A Dissertation

entitled

Wake-Fin Tailoring for Projectile Steering

by

Chuanbo Yang

Submitted to the Graduate Faculty as partial fulfillment of the requirements

for the Doctor of Philosophy Degree in Engineering

Dr. T. Terry Ng, Committee Chair

Dr. Ray Hixon, Committee Member

Dr. Sorin Cioc, Committee Member

Dr. Chunhua Sheng, Committee Member

Dr. G. Glenn Lipscomb, Committee Member

Dr. Patricia R. Komuniecki, Dean
College of Graduate Studies

The University of Toledo
May 2011

An Abstract of

Wake-Fin Tailoring for Projectile Steering

by

Chuanbo Yang

Submitted to the Graduate Faculty as partial fulfillment of the requirements
for the Doctor of Philosophy Degree in Engineering

The University of Toledo
May 2011

The overall goal of this dissertation is to investigate an active flow control concept, called wake-fin tailoring (WaFT), for improving the steering performance and attitude control of projectiles. The concept is based on the use of mechanical flow control actuators located at a position well upstream of the projectile's tail. With an asymmetric deployment of the actuators, the system induces an asymmetric wake-flow that interacts with the tail fins to generate aerodynamic control forces and moments. The system can be used to provide in-flight adjustment capability, reduce dispersion and increase endgame maneuver footprint of the projectiles.

The investigation results in the following:

1. Proof-of-concept experiments and computational simulations were conducted to investigate the feasibility of the proposed method. Low-speed wind tunnel experiments were performed on a representative surrogate tank munitions (STM) model. Effects of actuator parameters such as shape, locations (axis and azimuth), and actuator size were examined. Based on the results, the best control configuration was identified.

2. Steady CFD modelings of the projectile were carried out at subsonic and supersonic speeds to investigate the flow control mechanism and determine the control performance at operational flight speeds.

3. Unsteady CFD simulations were performed to evaluate the performance of

WaFT during dynamic events including spinning motion and dynamic deployment of actuators.

Results from wind tunnel experiments and CFD simulations demonstrate effective generations of control forces and moments by the WaFT system. The overall control authority is derived from two effects. First, a deployed actuator modifies the local surface pressure resulting in a local force. Second, the wake of the actuator interacts with the tail-fins downstream to change the pressure distributions on the fins. As a result, the control authority is enhanced compared to either effect alone. Additionally, a wide control bandwidth and a small drag penalty are expected due to the small size of the actuator.

Dedicated to my wife, Yi Guo, my children, Lillian and Ethan, my parents and my parents-in-law. Thanks for all your love and support.

Acknowledgments

I express my deepest thanks and gratitude to my advisor, Dr. T.Terry Ng, for his guidance,constant encouragement and patience which made this work possible. I am very grateful for his enlightening discussions and suggestions as well as the intellectual support he has provided.

I would like to thank Dr. Ray Hixon for the engaging teaching regarding CFD in the classes of CFD I and II. You peaked my interest in CFD and inspired me to learn as much as possible about the subject.

I would also like to thank the members of my dissertation committee, Dr. Sorin Cioc, Dr. Chunhua Sheng, and Dr. G.Glenn Lipscomb for their valuable time and generous help.

I want to acknowledge my special thanks to Mr. John Jaegly and Mr. Randall Reihing for their excellent and devoted work at the Engineering Machining Lab.

Table of Contents

List of Tables

List of Figures

List of Abbreviations

AFC	Active flow control
AOA	Angle of attack
BL	Baseline
BWF	Baseline without fin
CG	Center of gravity
Ma	Mach number
Re	Reynolds number
St	Strouhal number
STM	Surrogate Tank Munition
WaFT	Wake-Fin Tailoring

List of Symbols

C_D ..... coefficient of drag
C_n ..... coefficient of yawing moment
C_l ..... coefficient of rolling moment
C_m ..... coefficient of pitching moment
C_N ..... coefficient of normal force
C_Y ..... coefficient of side force
C_P ..... coefficient of pressure

α_{SV} ..... onset angle of attack of symmetric vorticies (deg)
α_{AV} ..... onset angle of attack of asymmetric vorticies (deg)
α_{UV} ..... onset angle of attack of unsteady vorticies (deg)
θ ..... azimuthal location (deg)
Δt ..... time step ($second$)
Δt^* ..... non-dimensional time step
ρ ..... density of air (kg/m^3)
μ ..... dynamic viscosity of air (kg/ms)
k ..... turbulent kinetic energy (kg/ms^3)
ω ..... specific dissipation (kg/m^3s^2)
H_d ..... helicity density (m/s^2)

D ..... maximum diameter of body of revolution
L ..... projectile body length
U ..... free-stream velocity (m/s)
V ..... velocity (m/s)
x ..... coordinates along downstream direction (m)
y ..... coordinates along cross-stream direction (m)
z ..... coordinates along spanwise direction (m)
y_p ..... distance of node p from wall
y^+ ..... non-dimensional distance from wall

Chapter 1

Introduction

The goal of flow control is to achieve some desired aerodynamic objectives as a function of time and space by the application of an appropriate actuator. The objectives may include drag reduction, separation control, aerodynamic control, enhanced mixing, noise suppression, change of a surface property; etc [1]. Among them, Aerodynamic control is a key issue for the present and next generations of projectiles to achieve enhanced flight performance and maneuverability. For an aerodynamic body, aerodynamic flow control can be attained by manipulating the flow field around it to promote or delay transition, prevent or provoke separation, and suppress or enhance turbulence. The application of flow control techniques for a specific projectile is usually based on the design objective and mission requirements.

Over the years, significant efforts have been conducted in developing innovative flow control techniques to improve the flight control of projectiles. A number of unconventional flow techniques based on the usage of novel miniature actuators have been developed in the wind tunnel laboratory in the University of Toledo. Some of the results are presented in the references [2-7]. Lopera and Ng [2, 3] assessed the effectiveness and attainable control authority using deployable miniature spoilers mounted at aft body boattail and aero control fins for the control of a U.S. Army Smart Cargo projectile at low angles of attack. The capability of a control concept of

reconfigurable porosity for providing control forces was also experimental investigated on the same model [4]. Their results show both control methods are effective in providing controlled pitching moments. Deployable strakes were applied on the aft body of a U.S. Air Force DEX model by Lopera and Ng [5, 6] for yaw control at high angles of attack. It was observed a strake placed on one side had the effect of lifting the vortex associated with it, resulting in a side force. Recently, Patil and Ng [7] numerically investigated active flow transpiration method for steering a small caliber projectile at supersonic speeds. The asymmetry induced in the flow due to the interaction between the flow exiting from transpiration channel and main stream flow was demonstrated to be effective in generating a control force.

1.1 Motivation

The present study focuses on the demonstration of the effectiveness of a low-cost flow control concept for active aerodynamic control of Army's next generation smart munitions. Currently, munitions depending on the conventional guidance and aerodynamic flow control technology are suffering from the limitations of traditional hinged control surfaces, and also are expensive and have no capability to dynamically re-target mobiles targets. This is because the response rate of the control surface is slow, and the control system lacks the ability in generating control force to turn the munitions at off-design conditions which are often encountered during endgame maneuvers or during prosecution of targets of opportunity. To improve the steering performance and attitude control of this kind of slender projectiles, a fast- response control system, named Miniature Control Actuator System (MCAS), was developed. The control employs miniature flow control actuators and advanced control strategies to provide in-flight course-correction capability for Army's next-generation smart munitions.

The MCAS control concept is to be extended to a surrogate tank munition (STM,

shown in Figure 2-1), which features a reduced-diameter tail-piece with six tail fins. The MCAS technology working with the WaFT control strategies aim to eliminated the need for traditional servo-based control surfaces for aerodynamics control and produce a low-weight, volume, cost, and fast response control system. Additionally, the proposed technology will provide an in-flight adjustment capability that will help reduce dispersion and increase endgame maneuver footprint of the projectile. Besides the goal of enhancing the munitions' performance at off-design conditions, the MCAS concept is particularly appealing because it reduces the system complexities associated with integrating flow control devices into the controlled model.

The particular geometry and operating envelope of the STM, however, present challenges to the MCAS concept. Since the operating angle of attack for the STM is relatively low (less than 10°), vortex controls as that used by Lopera and Ng [5, 6] are ineffective. For low angles-of-attack, the tail area would be the most effective control section. Incorporating a flow control system near the tail section is however very challenging due to the small cross-section of the tail-piece of the STM, and practically impossible because the tail fins need to be extremely thin and wrapped around the base for proper stowing before the gun-launch.

Due to the mission requirement and difficulty of hardware installation mentioned above, an innovative control concept named "Wake-Fin Tailoring" (WaFT) that provides directional control to the chosen STM would be investigated. The WaFT concept is based on the usage of flow control actuators located on the main body of the projectile upstream of the tail. Using an asymmetric deployment of the actuators on the symmetric STM main body, the system induces an asymmetric interaction between the wake of the actuators and the tail fins to generate aerodynamic control forces.

It is the intent of this program discussed herein to examine the feasibility of this novel active flow control concept. Both proof-of-concept experiments and computational simulations were performed. In addition, the flow control mechanism is studied

and the control effect is optimized.

1.2 Literature Review

Flow control includes any mechanism or process through which the fluid flow is caused to behave differently than it normally would if the flow was developing naturally along a control surface [8]. Flow control is designedly introduced to manipulate a flow field actively or passively to effect a desired change in free shear flows or wall bounded flows. As concluded by Gad-el-Hak [9], flow control can be used to achieve transition delay, separation prevention, drag reduction, lift augmentation, turbulence suppression, noise abatement, noise abatement, and heat and mass transfer enhancement.

A particular flow control strategy should be chosen based on the flow situation and the purpose of the control when there are a number of flow control strategies to control or mitigate flow. A unifying principles is to achieve a goal using a simple device that is inexpensive to build as well as to operate, and most important, has minimum side effects. Flow control goals are strongly interrelated, and one scheme for classifying control strategies considers energy consumption. Flow control flow control can be categorized into passive if no auxiliary power needed and active when energy is required in an open or closed control loop.

Over the years, a great number of Active Flow Control (AFC) techniques have been practically applied with great benefits in the aerospace community. Active approaches offer some performance advantages over passive flow control methods. Active control can be turned off when it is not needed, and it may be adaptable to changing flight conditions. Any active flow control system involves control actuators, either fluidic or mechanical, and sensors if feedback control included. The discipline of such flow control is to select the best receptive locations on the aerodynamic body where a micro-actuation can be performed at low energy cost and produce a macro-

effect on the whole body performance [10].

The Wake-Fin tailoring method is a kind of active flow control in that energy is needed to deploy the control actuator. It is aimed to manipulate the flow around the STM model using micro-actuators and upon deployment produce aerodynamic control forces for providing directional control to the chosen model. Herein, the previous and related work was reviewed and a summary of the work will be presented.

1.2.1 Aerodynamic Flow Control for Slender Projectiles

Fluid mechanics for active flow control is a multidisciplinary field, which involves flow physics, control theory, actuators and sensors technologies. Just like the beginning of the last century, some fundamental problems for flow control, such as separation control, drag reduction and noise suppression, continue to be the focus of attention today. However, the understandings of flow behavior, control approaches and the techniques of actuators and sensors have evolved significantly. As such, more and more practical applications of active flow control are being investigated.

There is an increasing amount of interest in using active flow control to improve the maneuverability and performance of aerodynamic bodies such as an aircraft and projectile. Among potential applications, controlling the trajectory of projectiles during flight using active flow control is a promising one. A general principle is unbalancing the pressures exerted on the projectile body surface through changing the flow around it. This pressure imbalance may be produced by surface deployment or by the use of one or more pyrotechnical mechanisms judiciously distributed along the projectile.

As mentioned above, any active flow control necessarily includes actuators. As such, regardless of flow physics, aerodynamic control of slender projectiles using active approaches can be classified based on the type of actuators. Cattafesta and Sheplak [11] proposed a useful classification where the actuators were organized based on function. The most common type is fluidic with primary function of fluidic injection

or suction. The representative actuators within this classification are synthetic jet and pulsed jet. Fluidic actuators have been applied to enhance projectile aerodynamic performance. Farnsworth and Amitay [12] tested the effectiveness of arrays of synthetic jet actuators on an unmanned aerial Vehicle at low angles of attack. Their wind tunnel results show that synthetic jets have the capacity of altering the local streamlines and displace the boundary layer on the suction surface of the UAV's wing. A small quasi-steady interaction region is produced, and the changes induced on aerodynamic forces can be proportionally controlled. Sahu [13] numerically studied a spinning projectile with flow control using a synthetic microjet, which takes advantage of jet-interaction with the free stream flow to generate aerodynamic control force.

Additional to fluidic and moving-surface actuators, a new technology using non-thermal surface plasma has gained popularity in recent years. Plasma actuators consists of using the electric wind produced by the discharge within the boundary layer to modify the near-wall flow, or to actively interact with the surrounding natural large-scale flow structures [14]. The plasma actuator technology has been shown to be successful in a large number of low-speed aerodynamic flow control applications including separation control, lift enhancement, drag deduction and flight control without moving surfaces. Gnemmi [15, 16] investigated the feasibility for steering a supersonic projectile by using activating plasma discharges at the tip of the projectile. He shows the perturbation caused by the plasma discharges is strong enough to distort the shock wave and thus produced a lateral force and a pitching moment that favorably combine to steer the projectile. To reduce the drag and provide directional control of a slender projectile, Corke and Tillotson [17] applied Single Dielectric Barrier Discharge (SDBD) plasma actuators on the blunt aft portion of the projectile. At a range of free-stream Mach numbers from 0.3 to 0.5, experimental results indicated an optimum location upstream of the flow separation location and a linear dependence of flow turning angle with plasma actuator voltage. By vectoring the flow angle and

wake, significant drag reduction and side force generation were attained. Despite the large volume of work, flow control application using plasma or fluidic actuators near atmosphere pressure still suffer from insufficient control authority, especially in high speed air vehicles.

Another class of actuator involves moving body inside or on the domain boundary, which are used to induce local fluid motion. Examples can be piezoelectric flaps, rotating or morphing surface, and deployable miniature spoilers. Micro-mechanical actuators, type of moving surface actuators, have been widely investigated in the last decade. At high angles of attack, a number of approaches for side force and yawing moment control are developed by utilizing the separation and induced asymmetric vortex shedding occurred near the nose [18, 19], which was first observed by Allen and Perkins [20, 21] in 1951, Rao [22] is one of the first researches to suppressing side forces by mounting a pair of helical trips on pointed fore bodies. The first numerical simulation in predicting the vortex asymmetry occurred on slender bodies of revolution at high angles of attack was carried out by Degani and Schiff [23, 24]. A vast amount of experimentally and numerically research was conducted to investigate parametric effects factors including the shape of the nose and the flight speeds. Many flow control approaches were also proposed and investigated where the forebody vortices were manipulated to produce controlled yawing moments. A micro-mechanical actuator, named strake, was proven by Ng [25], Stahl [26], Ng and Malcom [27], Modi [28], Chen [29], and Lopera [5] to be one of the most promising methods in achieving this form of control.

As oppose to at high angles of attack, three-dimensional separation occurs symmetrically at low angles of attack for a long pointed slender body [30]. The ideal position to apply active control for pitching control of slender bodies is normally the aft body. A typical conventional application is elevators at the rear of the stabilizer, which can be found at the rear of the fuselage of most aircraft. Recently, great research effort has been conducted to develop novel micro-mechanical actuators with

fast time response for aerodynamic force control of slender projectiles. Massey et al, [31 and 32] proposed a method to control the flight of a supersonic projectile based on shock-boundary-layer interactions. They placed a pin next to a tail fin to produce a local lift force, which then was used to produce expected rolling moments.

Two control concepts used micro-actuators were developed by Gjiko and Yiannis[33]. The first consists of a micro-flap in the form of a delta wing that can be deployed and activated at a location on the ogive nose of the projectile or at the beginning of its cylindrical aft body. The second is based on micro-balloons, which can be inflated and change the local pressure distribution on the projectile. Their results shows lift force can be generated, which can potentially be used to provide control force for possible maneuvering of the projectiles. Liang and Fu [34] applied a drag reduction method to provide passive control of shock/boundary-layer interaction on the boattail to improve the performance of a secant-ogive-cylinder-boattail projectile. A porous surface and a cavity or submerged plenum were used, and the configuration produced a 7% reduction in total drag.

Ng and Patel [35-38] conducted a series of investigations on active micro-mechanical actuator flow control applying to a family of slender bodies including: missiles, munitions and projectiles at low angles of attack where the baseline control is primarily provided by tail-fins. Main objectives of their work are to enhance the range and end-game maneuvering of the weapons by integrating miniature-spoilers on the boattail and fins to provide pitching and yawing controls. Their results demonstrate significant control-force generation and effective force modulation by varying spoiler-configurations at low angles of attack.

1.2.2 Fluid Mechanism for Active Flow Control

The flow involving in active aerodynamic control of slender bodies is mostly a kind of wall bounded flows. Regardless of actuator operation, the basic flow phenomena and flow physics involving in the flow control system are flow separation, flow-actuator

interaction, and flow- fins interaction if fins are included.

1.2.2.1 Flow Separation

Under certain conditions, wall-bounded flows separate. A boundary layer is a thin region near the surface of a wall where viscous effects are important. Following the comprehensive review of separation flow by Simpson [39], separation is defined as the process by which an attached boundary layer flow undergoes a departure or breakaway from a wall surface. To describe the characteristic of flow separation, Sears [40] first introduced the concept of limiting streamlines, identified as the streamline which is parallel to the wall. A line, near which adjacent limiting streamline will tend to leave the surface, can be defined as the line of separation [41]. Furthermore, Maskell [42] observed a surface of separation along which the joined separation streamlines from opposite sides would merge and leave the surface as single streamlines.

Once the flow separates, it interacts with the free-stream flow in an almost inviscid manner resulting in an inherently unsteady flow. The interaction is nonlinear and dominated by vortex dynamics. Improved understanding of flow separation can be gained by studying the dynamics of vorticity. Lighthill[43,44] studied flow separation by means of vortex dynamics. Focusing on the surface vortex lines and associated skin-friction lines, which cross each other at 90° on the surface, Lighthill found solid walls can be treated as the "source" of vorticity. Vorticity is then convected along the wall and diffused across the boundary layer. Essentially, vorticity is contained within the boundary layer since the diffusion process is very weak. Once the flow separates, vorticity is released in the flow. As such, the shape and size of the separated region is controlled by the direction of the vorticity vector along the line of separation [45].

A steady, two-dimensional boundary-layer separation was first explained by Prandtl in 1904. For steady, two-dimensional flows, a vanishing shear stress and flow reversal are traditional indications of flow separation. However, during 1950s, different characteristics between two-dimensional unsteady flows, three-dimensional steady and

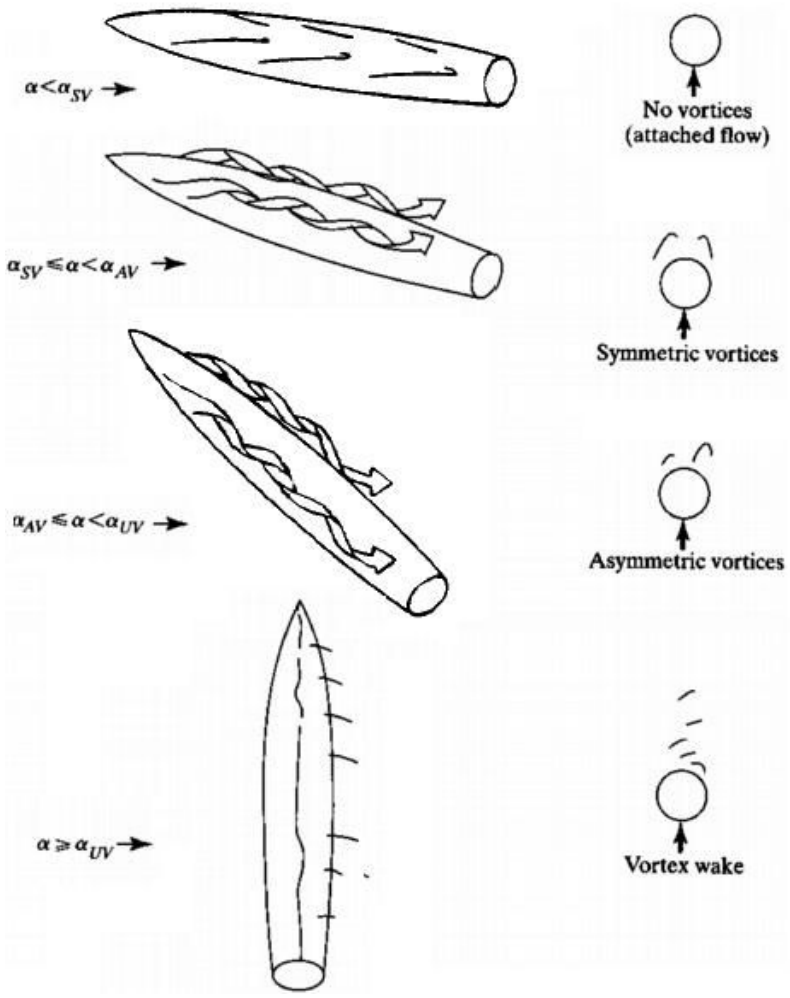

Figure 1-1: Effect of angle of attack on leeside flow field.Reproduced from Ref.49.

unsteady flows and steady two-dimensional flows were discovered by Rott, Sears and Moore [8]. They found the point (line) of vanishing wall shear did not necessarily coincide with separation, which greatly complicates the flow separation problems. In the past few decades, theoretical and numerical analysis of three-dimensional separation is considerably less developed. That is because there is no universal law of the wall for three-dimensional turbulent boundary layer, and the separation processes will be non-unique. A large cross-flow velocity component can occur, which induces large anisotropy in the flow [46].

In general, the overall development of flow separation region is affected by three distinct directions in space including the directions of oncoming free-stream, local direction of the line of separation and the direction of the vorticity vector at separation [45]. Associated with the flow separation physics and vortex dynamics, the aerodynamic performance of slender body of revolution can be divided into four principal flow patterns through the angle-of-attack range from 0° to 90° [47]. Shown in Figure 1-1, the first flow pattern is vortex-free flow or attached flow since the flow is dominated by axial flow component, which happens at low angles of attack. The cross-flow will cause a thickening of the boundary layer on the leeside. If the nose is sufficiently blunt, the axial flow may separate on the nose tip and then reattach, creating a closed type flow separation. This closed-type flow separation may subsequently delay the development of flow separation on the aft body [48]. The cross-flow separates and produces a symmetric vortex pair at intermediate angles of attack. The characteristic of the third principal flow pattern is asymmetrical flow separation at higher angles of attack. In this flow regime, a side force and yawing moments will be generated at zero sideslip. The final cross-flow pattern at very high angles of attack is almost identical with the impulsively started flow over a circular cylinder. At the leeside, axial component is greatly vanished, and the flow separation becomes unsteady starting on the aft body and advancing toward the nose with increasing angles of attack. The low angle of attack flow control on slender body is for the absolute angle of attack range from 0 degree to the angle where symmetric vortices occur on the leeside of the slender body [49].

Control of flow separation, historically referred to as boundary-layer control or BLC, is desired to prevent, modify and provoke flow separation achieved mostly by either passive or active techniques. Typically, configurations to study separation control include flow over backward-facing steps and ramps, on sharp-leading wedges, on bluff bodies, on various airfoils, delta wings, circular cylinders, behind two-dimensional fences and slender aerodynamic bodies.

1.2.2.2 Flow - Actuator/ Fin Interaction

Flow-actuator interaction is the interaction of an actuator that is immersed in a fluid. Inherently, flow control using actuators takes advantage of flow-actuator interactions. If the interaction is significant enough, a particular goal can be achieved. The scope of the literature review herein focus on flow physics for the interaction between solid body actuators and supersonic flow.

As pointed out by Hemsch[50] and Hsia[51], the basic fluid dynamic interactions of a solid body, or a jet, in a supersonic cross-flow are essentially the same: providing blockage to the flow. Typical two-dimensional flow field and pressure distribution are shown in figure 1-2, as presented by Spaid and Cassel [52]. Upstream of an actuator, either fluidic or mechanical, a thickening of the boundary layer is caused by the actuator. In addition, complex shock patterns are induced near the interacting region. Upstream of this region there is a rise in pressure associated with the separation shock caused by boundary layer flow separation. Downstream there is a low-pressure region corresponding to a recirculation flow zone.

Compared with flow control at subsonic speeds, shock-boundary-layer interactions are mostly involved within control system at supersonic speeds, which make the problem more complex. The interaction of a shock wave with a boundary layer was apparently first observed by Ferri [53] in 1939. The interactions represent the imposition of the strongest adverse pressure gradients on viscous layer which are susceptible to disruption by such gradients. It was also found the interactions depend on the free-stream Mach number, the characteristics of the incoming boundary layer, and the shock generator geometry [54].

If the flow is regarded as fundamentally three-dimensional, however, sweepback becomes a key element in shock/boundary-layer interactions. Typical studies of swept shock shock/boundary-layer interaction are on incoming supersonic flow interacting with fin or fins. Comprehensive reviews were given by Settles [54] and Knight [55], among others. It was pointed out by Settles [54] that 3D interactions were much more

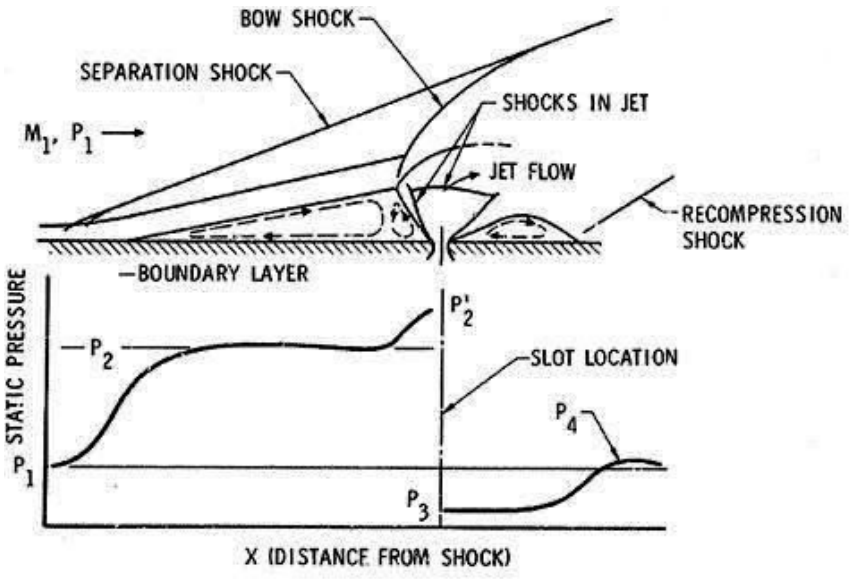

Figure 1-2: Flow field and pressure distribution of a supersonic jet in a supersonic cross flow.Adopted from Ref.52.

complex than 2D interactions because of the combined effects of compressibility and turbulence coupling between the normal and cross-flow components. Most swept interactions show evidence of boundary-layer separation other than those at low Mach number with weak shocks. Knight [55] reviewed 3D double fins configuration and interaction (also known as the crossing shock-wave/turbulent boundary-layer interaction). Most works on the subject analyze the pressure distribution and structure of the limiting streamlines on the plate surface (surface flow pattern) in the interaction region.

Several kinds of actuators were investigated recently to provide directional control for supersonic projectiles. Siliton[11] validated that placement of pins next to the fins does indeed produce local lift. The results show that the lift capability of the adaptive flow control technique can be used to create roll torque using two diametrically opposed pins. Gnemmi[21] used plasma discharge to produce a perturbation that can distort the shock wave attached to the conical projectile tip if the perturba-

tion is strong enough. An asymmetric flow field around the projectile was produced accompanying by a lateral force and a pitching moment that favorably combine to steer the projectile. Flow control using flow transpiration to generate aerodynamic control forces for steering a small caliber projectile at low angle of attack is numerical investigated by Patil and Ng [22]. The results show that the interaction of the naturally-powered flow, exiting from the transpiration channels, with the main stream flow leads to a complex three-dimensional shock wave structure on the projectile base coherent vortex structures downstream of the primary interaction shock. The asymmetry induced a considerable force which can be used for steering a small caliber projectile.

1.2.3 CFD Integration with Flow Control

Computational Fluid Dynamics (CFD) has been applied in aerospace for over 30 years. It can be used to reduce design cost and provide a more detailed understanding of the complex aerodynamics than the understanding achieved through experiments. Table 1.1 shows a comparison of Computational Fluid Dynamics (CFD) with Experimental Fluid Dynamics (EFD) [56]. With recent advances made in high-performance computing and CFD technologies (topics listed in Table 1.1), CFD, working as a kind of theoretical approaches, has been applied to many aerodynamic flow control studies, and is transforming itself from an experimental art to a predictive science [8].

The genesis of CFD has evolved in solving the time-dependent Navier-Stokes equation, a system of five nonlinear partial differential equations for three-dimensional single-phase fluid motions. With appropriate initial and boundary conditions, CFD is capable of solving laminar flow problems in principle. Turbulent flow simulations however remain a challenge to CFD. This is because the physics of turbulence is complex and always is a genuine three-dimensional, multiple-scale, nonlinear phenomenon. One approach providing approximate solutions to Navier-Stokes equations is Reynolds-Averaged Navier-Stokes (RANS), in which an instantaneous quality is

Table 1.1: Experimental Fluid Dynamic and Computational Fluid Dynamics.

EFD	**CFD**
Wind tunnels	Computers
Measurement techniques	Numerical algorithms
Manufacturing techniques	Programming techniques (Parallel language, etc)
Model manufacturing	CAD interface, grid generation
Data acquisition	Post-processing
Data handing	Visualization software
Reynolds number effect	Discretization error, turbulence model, etc

decomposed into its time-averaged and fluctuating quantities. The Navier-Stokes equations are satisfied with the solution of the ensemble average with turbulence closure models [57]. The ensemble averaging process is equivalent to the time averaging for statistically stationary flow. This process also eliminates several key characteristics of turbulence, such as the frequency, phase, and wavelength of the fluctuating motion. The most direct approach to simulate turbulence is the direct numerical simulation (DNS), in which all the spatial scales of turbulence, from the smallest dissipative scales up to the integral scale, is resolved without any turbulence model. An intermediate method to turbulent flow is the large eddy simulation (LES). The basic premise is that only the large eddies containing information about the geometry and dynamics of the flow have to be resolved, and the relative small-scale eddies have the universal structures according to Kolmogorov [58]. A filter function is built to eliminate the small-scale fluctuations and only the smoothed large-scale structures are retained.

Inherently, RANS is limited by the averaging procedure that defines it. Unlike LES, which models turbulence only at the smallest scales above some cut-off wave

numbers, RANS is designed to model turbulence across the entire wave number energy spectrum. It is in effect trying to model the effects of all turbulent eddies, even the largest ones, in an average sense [59]. One concern is that RANS may not be strictly valid for unsteady flow. Current RANS closures do however have the ability to identify the presence of large scale unsteadiness when run in an unsteady mode (URANS) [60], if the time scale of any gross unsteady motion is much greater than the physical time step employed, which in turn is much greater than the time scales associated with turbulence. A common test case to demonstrate its effectiveness is the flow around bluff bodies, where large eddies formed in the wake.

DNS requires that the entire range of spatial and temporal scales of the turbulence must be resolved. According to the Kolmogorov micro-scales, the ratio between the largest and smallest eddy of fluid motion is proportional to the value of $Re_y^{\frac{3}{4}}$. Therefore, for the three-dimensional problems of interest in most applications, the grid would involve order $Re_y^{\frac{9}{4}}$ grid points. As such, DNS is currently only practical at low Reynolds numbers and on some simple configurations. As pointed out by Shang [57], the DNS is used sparingly only for the laminar-turbulent transition, vorticity and energy production to acquire insight on the detailed spatial relations in kinematics and dynamics of turbulent eddies.

Comprehensive reviews on the current capability of LES were given by Piomelli [58], Rumsey et al [59], and Georgiadis et al [61]. In LES, because the remaining larger scale turbulent fluctuations are directly simulated the computational requirements on LES are still very high. Furthermore, resolution requirements near solid surfaces for LES are essentially the same as those for DNS. Baker [62] suggested that around 50 million points will be needed for RANS computations over a complete aircraft, while computing the turbulent boundary layer by large eddy simulation can be expected to increase this number to mesh sizes of around 510^9 points if the subgrid scale turbulence and viscous sublayer turbulence are modeled. Additionally, turbulent eddy simulation of the extremely small physical scales of the viscous sublayer dynamics will

likely increase the mesh size requirement to around 510^{11} mesh points, mesh sizes that appear well beyond the capability of computer hardware for the foreseeable future.

Application-oriented CFD for flow control is useful for determining locations for high receptivity to actuation and sensor placement, for testing actuator concepts, for optimizing flow control system design, and for obtaining scaling information needed for full-scale applications [63]. One more benefit of numerical simulations is that sensor and actuation schemes need not be physical realizable. However, active flow control also represents a challenge to CFD, because separation and unsteady flows are often involved. Resolving a wide range of scales of turbulence, resolving details of the actuator that extend below the nominal aerodynamic surface as necessary in some cases, and resolving the temporal and spatial scales of the actuation all increase the demands on CFD.

Comprehensive reviews of CFD for investigating the relevant physical mechanisms associated with active flow control method were given by Collis [1], Gross [64] and Rumsey [59]. Successes and challenges for flow control simulations were summarized. DNS is very powerful tool and can be used successfully for flow control simulation. Currently, use of true DNS is limited to very low Reynolds numbers, but some researches claim that "under-resolved" DNS at higher Reynolds number can also be useful for predicting certain qualities that do not appear depend on resolving the small scales in the flow. LES is being used by many researchers for flow control type problems. Like DNS, LES is impractical for high Re flows if the viscous sublayer needs to be resolved. Promising approaches to replace RANS are hybrid LES/RANS methods, such as detached eddy simulation (DES). These kinds of approaches would typical use RANS or a wall function near the wall, and LES to capture some desired unsteady structures away from the wall. Essentially, the RANS serves as an inflow boundary conditions to the LES region.

It is difficult to characterize the use of RANS for flow control application, because there has been such a wide range of application to date. Certainly, it appears that

turbulence modeling comes under question quite often for its applicability for these flows. It showed the inaccuracy in turbulence modeling is the main reason why CFD predictions can be severely degraded. For examples, Reynolds-averaged Navier-stokes may be employed for investigating steady flow control, but for unsteady flow control the flow structures that are relevant for the effectiveness of the actuation have to be resolved [64]. One more example is RANS models often fail to provide accurate results for high angles of attack flows since the large turbulence scales for separated flows are very dependent on the geometry. RANS models, however, can provide accurate results for attacked boundary layer flows, thin shear layers, and steady coherent vortical flow field, but at the cost of interesting empiricism due to the closure problem [65].

Although turbulence modeling is certainly a possible cause for poor RANS results, it may not always be the primary reason. It is usually difficult to simulate precisely the same conditions as experiment. In particular, for flow control problems the boundary conditions at flow control interfaces are often not defined in sufficient detail to make assignment of CFD boundary conditions entirely clear. Furthermore, conducting experiments in unsteady flow control can be much more difficult that in steady problems and measurement uncertainties can be larger. Considering the robustness and efficiency, for at least the near future, it is expected that that flow codes which solve the RANS equations will be the principal CFD methods used in aerodynamic design [66, 67, and 68].

Based on solving RANS equations, a great number of CFD simulations of flow control techniques for slender projectile aerodynamics control have been done in recent years. Mostly, CFD simulation is used to predict the forces and moments, flight characteristics coupling with degree-of-freedom trajectory simulations, and provide a more detailed understanding of the underlying complex flow physics once the simulation can be verified and validated [69, 70, and 71]. In CFD, verification and validation are the primary means to assess accuracy and reliability in computational simulations [72]. In verification activities, the accuracy of a computational solution is primarily

measured against experimental data with quantified errors and uncertainties estimated for both.

1.3 Objectives

In the present effort, an innovative active flow control concept for projectile steering is proposed and studied. Compared with other reviewed flow control methods, the proposed method is not only utilizing flow-actuator interaction to modify local flow near the actuator, but also wake-fins interaction to change the pressure loads on the fins. The wake-fin tailoring method is investigated using static wind tunnel and CFD studies, CFD modeling of spinning projectile with control, and CFD simulations of the dynamic deployment of actuators.

Specific objectives of this research are:

- ◇ To develop a novel active flow control method for aerodynamic control of projectiles and munitions at low angles of attack.
- ◇ To evaluate the effectiveness of the proposed flow control method in generating aerodynamic forces for projectile steering at both subsonic and supersonic speeds.
- ◇ To access the control performance for a spinning projectile.
- ◇ To investigate the process of dynamic deployment of control actuators.
- ◇ To perform the analysis of intrinsic flow physics and control mechanism associated with the proposed flow control method.

Chapter 2

Background

Recently, an innovative, low-cost, Miniature Control Actuator System (MCAS) is proposed for active aerodynamic control of Army's next generation smart munitions. The objective of MCAS is to provide in-flight course-correction capability for line-of-sight (LOS) and beyond line of sight (BLOS) munitions. Utilizing miniature flow control actuators and advanced control strategies, the benefit of MCAS over conventional hinged surfaces control system include low- weight, volume, and cost, and faster response rate, which translate into improved range, accuracy, and lethality of the munitions. Continuous in-flight adjustments will help reduce dispersion and increasing endgame maneuverability.

To develop the MCAS technology the surrogate tank munitions (STM) model shown in Figure 2.1, whose attributes are made to resemble those of the Army's 120mm Line-of-Sight Multi-Purpose (LOS-MP) munition, was built and tested for proof-of-concept investigations. The LOS-MP program started in 2004. To be more useful in urban battlefields, the Army's main battle tank need to be armed with advanced multipurpose rounds that can be adapted for use against different types of targets. A multipurpose munition would offer tankers flexibility to target not only armored vehicles, but foot enemy soldiers or light trunks, even if they are shielded by a rock wall or within a fortified concrete shelter.

The chosen STM model is a kind of fin-stabilized projectiles. These projectiles obtain stability through the use of fins located at the aft end of the projectile. Additional stability is obtained by imparting some spin (approximately 18 rev/s) to the projectile by canting the leading edge of the fins. In contrast to conventional spin-stabilized projectiles, which derive their in-flight stability from the gyroscopic forces resulting from the high rate of spin, the finned projectiles are stabilized during flight by aerodynamic forces acting on the projectile. Although projectile spin does not contribute to the stabilization of finned projectiles, a low rate of roll around the longitudinal axis is desired to minimize the adverse effects of mass and configurationally asymmetries which may result from material imperfections and from manufacturing tolerances.

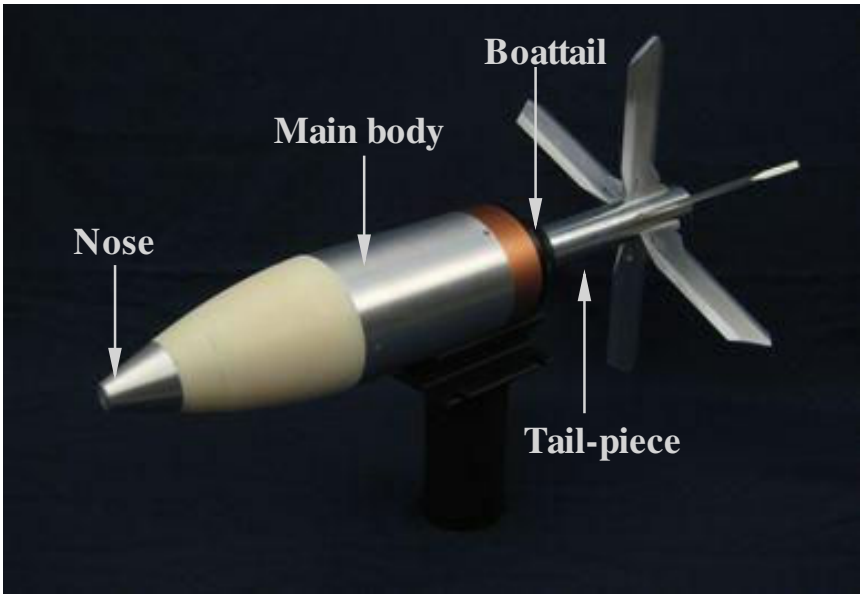

Figure 2-1: A picture of the chosen STM model.

Shown in Figure 2-1 and 2-2, the studied model is assembled to be symmetric to its longitudinal axis. The model features a small blunt nose and a reduced-diameter tail-piece with six tail fins, which make the configuration aerodynamically highly stable and hard to maneuver. The total length and maximum diameter of this slender

projectile are 621.75 mm and 114 mm respectively, which yield a fitness ratio of 5.45.

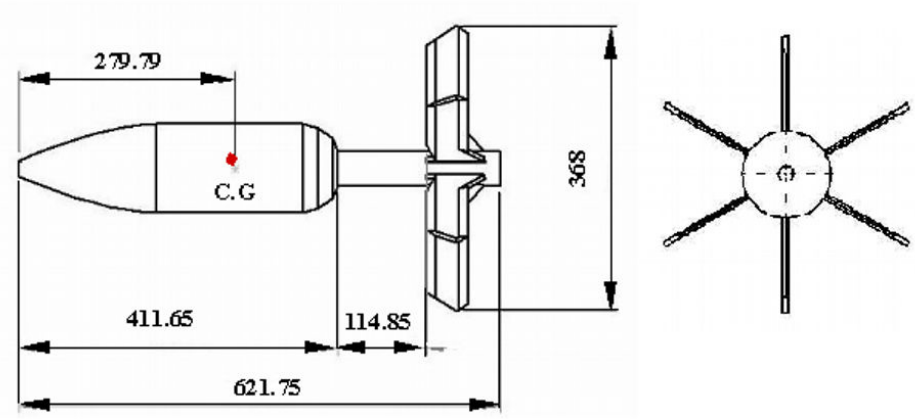

Figure 2-2: A schematic for STM model (all dimensions in millimeters).

2.1 Wake-Fin Tailoring Method

A Wake-Fin Tailoring (WaFT) flow control method is proposed to augment the MCAS technique. Inherently, WaFT is a kind of active flow control method. In the control-off state, actuators are placed inside the munition body surface and flushed with the outer surface. Once control is on, the actuators can be applied to generate asymmetrical aerodynamic forces, which result in control moment generation. In the real situation, the actuators can be turn on autonomously via a feedback controller. One particularly appealing characteristic of this concept is it reduces system complexities and the problems associated with integrating flow control devices near the tail fins. In a typical application at low angle of attack condition, the aft body near the tail is viewed as the most effective section in a projectile's body for applying flow control. For some projectiles including the STM, incorporating a flow control system near the tail fin section is not feasible since the tail fins are extremely thin and need to be wrapped around the base for proper stowing before the gun launch. The

WaFT method can offer a practical and potentially highly-effective means to apply flow control to the Army's STM, and subsequently on the Army's Los-MP muniton, for generating forces for steering.

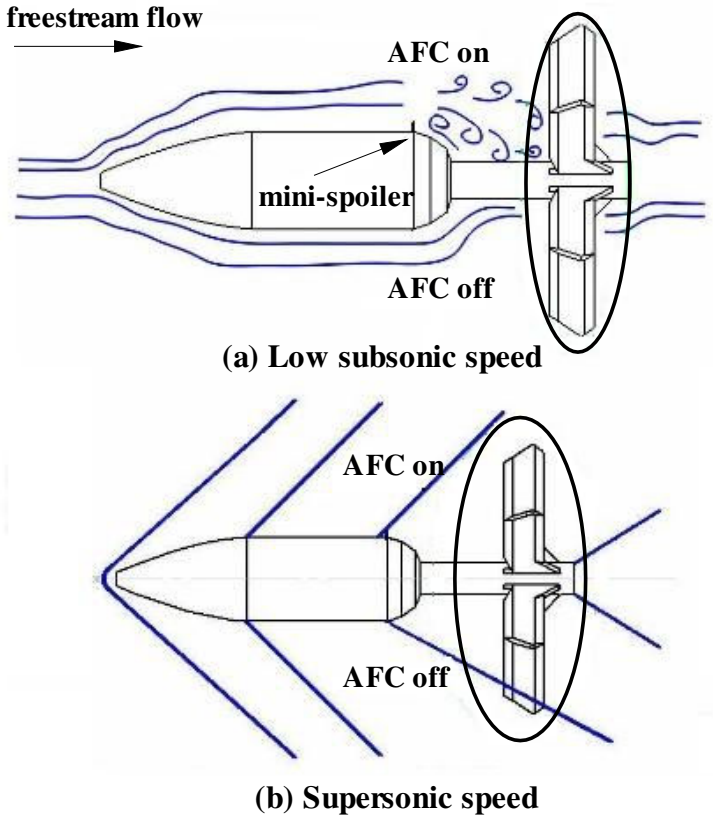

Figure 2-3: Illustration of the Wake-Fin Tailoring method using boattail-mounted flow control actuators.

The WaFT control approach is illustrated in Figure 2-3. In this approach, one or more flow control actuators are strategically mounted and stowed at the upstream of a projectile's tail. The flow around the downstream-located fins can be altered once the actuators are deployed. By using an asymmetric deployment of the actuators, the system induces control forces and moments through tow mechanisms. First, a deployed actuator modifies the local surface pressure resulting in a local force. Second, the wake of the actuator interacts with the tail-fins downstream to change the pressure

distributions on the fins. The flow fields associated with this control mechanism are however complex and involves fluid interactions of an actuator or actuators with the cross-flow, flow separation, shock/turbulent boundary-layer interaction, and actuator-induced wake/shock-fins interactions (3D shock impingement).

The WaFT method may be viewed as a kind of active flow control strategy since external energy (electrical or mechanical) is required to deploy and re-stow the actuator. The concept is also a steady control method since, once the actuator is deployed, no time-varying effects, such as the addition of mass, momentum, energy, or vorticity, or shape modulation, including periodic or quasi-periodic approaches, is involved at a timescale commensurate with the relevant dynamics of the flow.

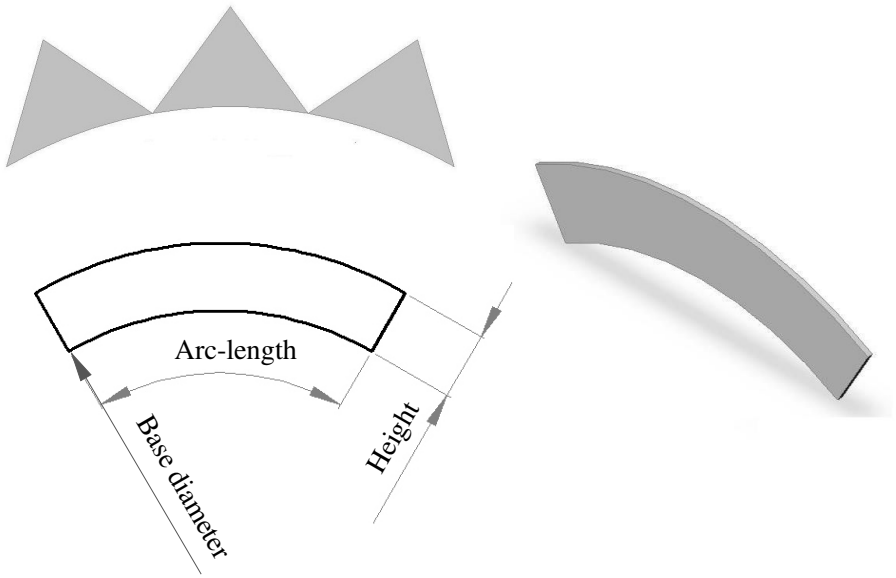

Figure 2-4: Illustration of micro-mechanical actuators.

2.2 Flow Control Actuators

Several different types of flow control actuators were experimentally and numerically examined in previous studies on different projectile configurations. Control actuators investigated include micro-mechanical actuators in the forms of spoiler and vortex generator, active vents, and single dielectric barrier discharge plasma actuators. The results indicated all control actuators except the plasma actuator were effective in providing control moments. It was also observed that mechanical spoiler was the most effective actuator device in general. As such, only mini-spoiler is employed in the present study to validate the Wake-Fin Tailoring methods.

Based on previous studies on spoilers, thickness is not a significant factor as long as it is small relative to the other spoiler dimensions. As shown in Figure 2-4, the length (arc-length) and height of a spoiler are the parameters of interest. In addition, a discontinuity spoiler was also tested since it has the potential for easier stowing and deployment relative to a continuous one.

Spoiler nomenclatures to be used in presenting the results are listed below:

SP: Spoiler

DSP: Discontinuity Spoiler

DSP-TRI: Discontinuity Spoiler and include identical isosceles triangle pieces

DSP-TRI (N): N is piece number

DSP-REC (N): REC represents the pieces are rectangle

AA-BB-SP-CC-DD-EE-FF-GG

AA: Baseline without fins (BWF) or baseline (BL)

BB: Number of spoiler used, default is one

CC: Spoiler height (mm)

DD: Spoiler attached model surface diameter (mm)

EE: Arc length (degree)

FF: Azimuth location (degree, spoiler middle position)

GG: Distance from boattail (mm), positive is to nose direction

Chapter 3

Experimental and Numerical Approaches

3.1 Test Facility

Wind tunnel experiments were performed at The University of Toledo closed-loop, single return subsonic wind tunnel with a 0.9 m x 0.9 m (3 ft. x 3 ft.) test section. Two tempered glass sidewalls and a large Plexiglas window on the ceiling provided convenient access for flow visualizations from different angles. An array of about 4400 circular flow straightening elements of 1 foot length is positioned at the entrance of the contraction nozzle. The nozzle is 10 feet long and provides a 12:1 contraction ratio to the test section. Downstream of the test section, a rectangular diffuser with 3 degrees of horizontal and vertical expansion angles returns the flow to a circular section. A 5 foot diameter, fourteen-blade, variable-pitch fan coupled to a 150-hp electric motor is used to drive the flow. An essentially uniform flow, with a turbulence level of 0.2% outside of the wall boundary layers and speed up to 200 mph (89m/s), can be produced in the test section.

The tunnel is equipped with a C-strut model support and an automated turntable driven by an electric motor that allows for remote model positioning. A five-component

internal strain-gage force balance capable of measuring rolling, pitching, and yawing moments, and normal and side forces was designed and constructed. Moment and force measurements were taken using a National Instruments SCXI unit integrated with a 4 Hz low-pass filter for time-averaged measurements and a 10 kHz filter for unsteady measurements. A LabView program was customized to monitor the test section conditions, control the angles of attack, and measure the force balance outputs. A 0.5 W portable laser was used for laser sheet visualizations. The smoke supplied to the test section was produced by a Rosco Delta 3000 remote-controlled fog machine.

3.2 Experimental Conditions

Subsonic wind tunnel experiments were conducted at a Reynolds number of 1.75×10^5 based on a character length of 0.114 m and a freestream velocity of 22 m/s. As dictated by the operational flight envelop of Army's LOS-MP munitions, data were taken for angles of attack ranging from -10 to 10 degree at 1-degree increments. The sample rate and the number of samples are 100 Hz and 2000 Samples respectively.

A parametric study of the spoiler was performed, with actuator height, length, and axial and azimuth locations being the parameters of interest. The objective is to achieve the desired performance with the minimum spoiler size and most convenient installation.

3.3 Computational Considerations

The objective of the numerical study is to validate the WaFT concept and determine its supersonic performance. In addition, the flow phenomenon and control mechanism associated with the control will be explored in detail.

All the numerical simulations are conducted using a well-tested and widely used

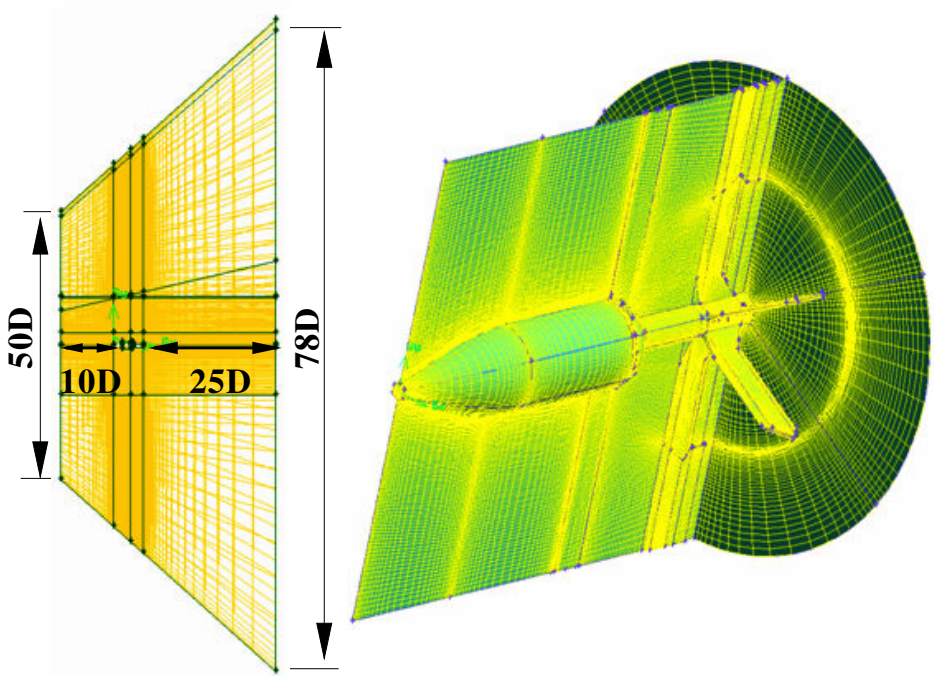

Figure 3-1: Typical computational domain and mesh for supersonic simulations.

computational fluid dynamics code, FLUENT. In the solver, second-order upwind scheme and coupled algorithm are used for spatial discretization and pressure-velocity coupling respectively. To accelerate flow convergence, Full Multigrid (FMG) is performed to initialize the numerical solutions.

The computational domain used for supersonic simulation is shown in Figures 3-1 and 3-2. The domain is a frustum of cone with a 50D diameter domain inlet and 45 degree increment of domain from inlet to outlet, where D is the maximum diameter of the projectile. The distance between inlet and model is 50D for subsonic and 10D for supersonic, and the distance between the outlet and projectile base is 100D for subsonic and 25D for supersonic.

Multi-block structured and unstructured meshes with conformal mesh at interfaces are generated in Gambit for different simulation cases. For supersonic simulations, hexahedral mixed cells were produced by using map or cooper mesh schemes. Tetra-

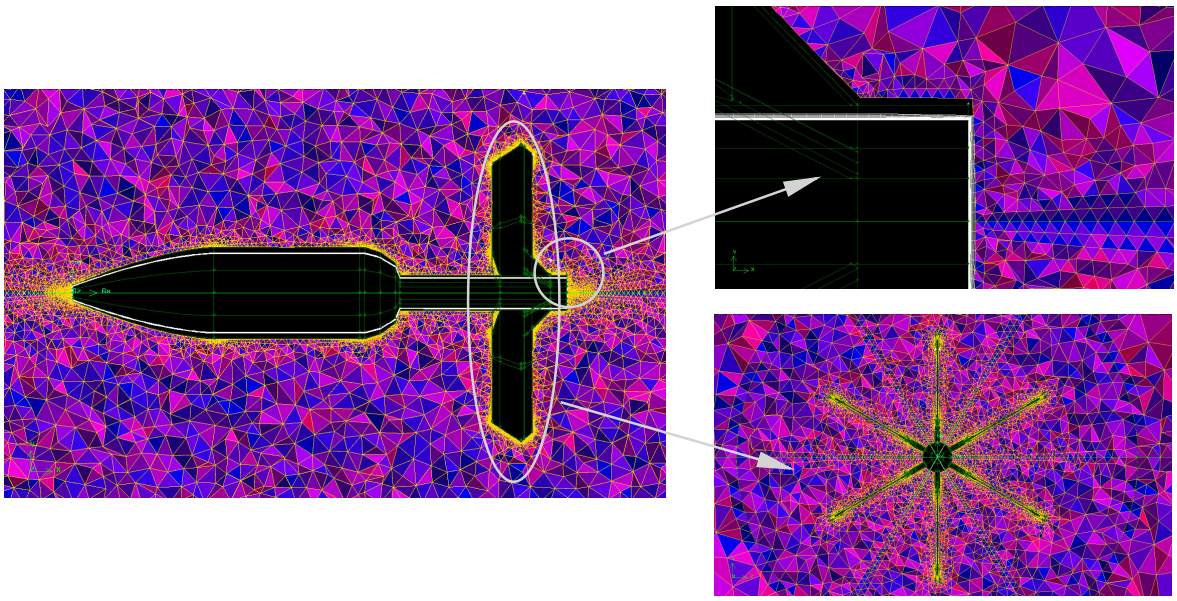

Figure 3-2: Tetrahedral mesh for finned baseline subsonic simulation.

hedral cells were generated for subsonic baseline simulations by applying Tgrid mesh scheme since the same boundary mesh is applied to the whole model at one time. The meshes are fine enough to allow the use of the near-wall treatment for K-omega turbulent model with enabled transitional flows option in Fluent.

In order to resolve the gradients near the projectile, the first cell height was calculated by using the following equation to capture the sublayer flow condition:

$$y_p = \frac{y^+ \nu}{U_\infty \sqrt{\frac{0.037}{Re_L^{0.2}}}} \tag{3.1}$$

Where y_p is first cell height, y^+ values for wall-adjacent cells is set to be less than 1, and Re_L is the Reynolds number based on the projectile maximum length of 622 mm. As a result, the first cell heights for subsonic and supersonic simulations are 0.01 and 0.0004 mm respectively. The mesh cell growth factor is 1.05 near the model and less than 1.15 at the far field areas.

Since the boundaries are sufficiently far from the projectile, Pressure-Far-Field

boundary condition, corresponding with ideal gas fluid material, was applied to inlet and far field boundaries. The outlet is set to be pressure outlet and the model surface treated as non-slip wall with zero heat flux. The supersonic simulations were conducted at Mach number 3, identical with the projectile flight speed. The freestream flow has a temperature of 300k with the turbulent level of less than 1%.

The simulations were determined to have converged based on four criteria. First, the residuals of all convection terms should be less than 1E-3. Second, the first three digits of the monitored moments (pitching or rolling) should not change for at least 50 iterations. Third, the first three digitals of the monitored velocity of a point, selected near the model, should not change for at least 50 iterations. Last, the net mass flow rate of the total domain should be almost zero.

3.4 Turbulence Modeling

At present, numerical techniques to solve the Navier-Stokes governing equations mainly include Reynolds-Average-Navier-Stokes (RANS) simulation, large eddy simulation (LES) and Direct Numerical Simulation (DNS). As mentioned in the literature review, due to the limitation of computational resources and time consideration, LES and DNS are applied mostly to simply geometries, and currently not practical at high Reynolds numbers and on full configurations. Particularly for complex flow problems at high Reynolds numbers, it appears that eddy-resolving methods are still decades away [66]. The numerical method used to investigate the performance of WaFT flow control method is based on a three dimensional finite-volume scheme to solve the Reynolds-averaged Navier-Stokes equations.

Undoubtedly, a good understanding of the physics of turbulent flow played a key role in motivating the design of new control schemes for wall-bounded turbulence. One of the most important improvements needed for all RANS models is to repair their tendency to under-predict turbulent eddy viscosity in near-wall separated shear

layers. This under-prediction results in delayed reattachment/recovery. Among the turbulence models employed for flow control application, the widely used SA and SST models are very robust and offer reasonable prediction in many cases.

Gnemmi and Rey [14] proposed a plasma actuation system for the control of supersonic projectile. Their fluid solver is based on the RANS equations and provides solutions for the transient, compressible, and turbulent ideal gas flow. The shear-stress transport (SST) two-equation model of turbulence is used to provide a link between the turbulent transport of momentum and energy, and the mean flow variables and fluid properties. It was found the computation using a fine grid and the SST turbulence model predicts the boundary-layer separation, the jet expansion, and the recompression shock with an accuracy that is of the same order of magnitude as that encountered in the experiments. Many researchers have used RANS to compute applications with surface blowing/suction for separation control. Vadillo and Agarwal [73] used active flow control for transonic flow applications on airfoils with shocks, using SST. Rehman and Kontis [74] used SST to investigate the effect of a synthetic jet on both a stationary and a pitching airfoil.

The eddy-viscosity turbulence model employed in the present study is Shear-Stress Transport (SST) $k-\omega$ two-equation model, which was developed by Menter in 1994 [75]. The shear-stress transport (SST) $k-\omega$ turbulence model is a type of hybrid model. The use of a $k-\omega$ formulation in the inner parts of the boundary layer makes the model directly usable all the way down to the wall through the viscous sub-layer. Hence, the SST $k-\omega$ model can be used as a Low-Re turbulence model without any extra damping functions. The SST formulation also switches to $k-\epsilon$ behavior in the free-stream flow region far from the wall and thereby avoids the common $k-\omega$ problem that the model is too sensitive to the inlet free-stream turbulence properties.

The SST $k-\omega$ two-equation model in FLUENT is the model from 2003[76], which has several relatively minor variations from the original SST version. Written

in conservation form, the two-equation SST $k-\omega$ model is given by the following:

$$\frac{\partial(\rho k)}{\partial t}+\frac{\partial(\rho U_j k)}{\partial x_j}=P-\beta^*\rho k\omega+\frac{\partial}{\partial x_j}[(\mu+\sigma_k\mu_t)\frac{\partial k}{\partial x_j}] \tag{3.2}$$

$$\frac{\partial(\rho\omega)}{\partial t}+\frac{\partial(\rho U_j\omega)}{\partial x_j}=\frac{\gamma}{\nu_t}P-\beta_2\rho\omega^2+\frac{\partial}{\partial x_j}[(\mu+\sigma_{\omega,1}\mu_t)\frac{\partial\omega}{\partial x_j}]+2(1-F_1)\rho\sigma_{\omega,2}\frac{1}{\omega}\frac{\partial k}{\partial x_j}\frac{\partial\omega}{\partial x_j} \tag{3.3}$$

Where,

$$P=\tau_{i,j}\frac{\partial u_j}{\partial x_j} \tag{3.4}$$

$$\tau_{i,j}=\mu_t(2S_{i,j}-\frac{2}{3}\frac{\partial u_k}{\partial x_k}\delta_{i,j})-\frac{2}{3}\rho k\delta_{i,j} \tag{3.5}$$

$$S_{i,j}=\frac{1}{2}(\frac{\partial U_i}{\partial x_j}+\frac{\partial U_j}{\partial x_i}) \tag{3.6}$$

The turbulent eddy viscosity is computed using the strain invariant in its definition:

$$\mu_t=\frac{\rho a_1 k}{max(a_1\omega,SF_2)} \tag{3.7}$$

$$S=\sqrt{2S_{i,j}Si,j} \tag{3.8}$$

To transform the standard $k-\omega$ model into equations based on k and ω, a cross-diffusion term is induced. The term is defined as

$$2(1-F_1)\rho\sigma_{\omega,2}\frac{1}{\omega}\frac{\partial k}{\partial x_i}\frac{\partial\omega}{\partial x_j} \tag{3.9}$$

Any of the constants is blend of an inner (1) and outer (2) constant, representing the original Wilcox $k-\omega$ model and standard $k-\omega$ model respectively. The relation between them is then:

$$\phi=F_1\phi_1+(1-F_1)\phi_2 \tag{3.10}$$

Additional functions are given by:

$$F_1 = tanh(arg_1^4) \tag{3.11}$$

$$arg_1 = min\left[max(\frac{\sqrt{k}}{\beta^*\omega d}, \frac{500\nu}{d^2\omega}), \frac{4\rho\sigma_{\omega,2}k}{CD_{k\omega}d^2}\right] \tag{3.12}$$

$$CD_{k\omega} = max(2\rho\sigma_{\omega,2}\frac{1}{\omega}\frac{\partial k}{\partial x_j}\frac{\partial \omega}{\partial x_j}, 10^{-10}) \tag{3.13}$$

$$F_2 = tanh(arg_2^2) \tag{3.14}$$

$$arg_2 = max(\frac{2\sqrt{k}}{\beta^*\omega d}, \frac{500\nu}{d^2\omega}) \tag{3.15}$$

Where ρ is the density, μ is the molecular dynamic viscosity. d is the distance from the field point to the nearest wall.

It is generally recommended to use a production limiter. In reference 72, the term P in the k-equation is replaced by:

$$P = min(P, 10\beta^\star\omega k) \tag{3.16}$$

The boundary conditions recommended by Menter [77] are:

$$\frac{U_\infty}{L} < \omega_{farfield} < 10\frac{U_\infty}{L} \tag{3.17}$$

$$\frac{10^{-5}U_\infty^2}{Re_L} < k_{farfield} < \frac{10^{-1}U_\infty^2}{Re_L} \tag{3.18}$$

$$\omega_{wall} = 10\frac{6\nu}{\beta_1(\Delta d_1)^2} \tag{3.19}$$

$$k_{wall} = 0 \tag{3.20}$$

Where L is the approximate length of the computational domain, and the combination of the two farfield values should yield a freestream turbulent viscosity from 10^{-5} to 10^{-2} times freestream laminar viscosity. As a result, the farfield turbulence

conditions are somewhat open to interpretation.

The constants are:

$$\gamma_1 = \frac{5}{9}, \gamma_2 = 0.44, k = 0.41, \sigma_{k,1} = 0.85, \sigma_{k,2} = 1.0$$

$$\sigma_{\omega,1} = 0.5, \sigma_{\omega,2} = 0.856, \beta^\star = 0.09, \beta_1 = 0.075$$

Chapter 4

Subsonic Study

4.1 Experimental Results

Wind tunnel experiments were conducted on the STM model at subsonic speed. Configuration and parametric studies were performed to determine the effects of actuator position and size on the control performance. One of the main objectives is to seek the optimal control with the minimum actuator size and a configuration that is convenient for installation. The most effective configuration and corresponding actuator were used for the numerical supersonic investigation presented in later chapter.

Spoiler control was applied to two projectile configurations in this study. First is the baseline without fins (BWF) configuration. Second is the model with fins (BL). The wind experiments were static in nature. Static actuator surfaces were attached onto the model surface at the desired location to represent the status when the control has been fully deployed. Miniature-spoilers are utilized as the flow control actuator for all the experimental and numerical investigations. Aerodynamic forces and moments are assumed to be functions of height, length, longitudinal and azimuth location of the spoiler.

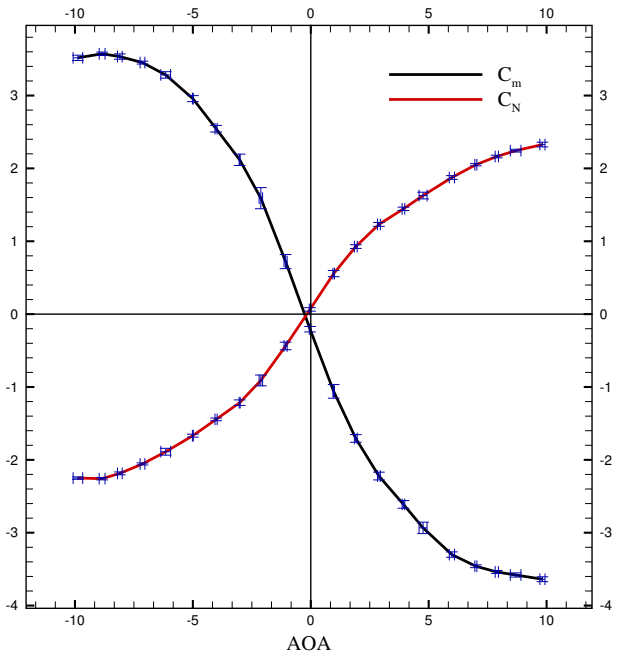

Figure 4-1: Pitching moment and normal force coefficient for baseline corresponding to 95% conficence level.

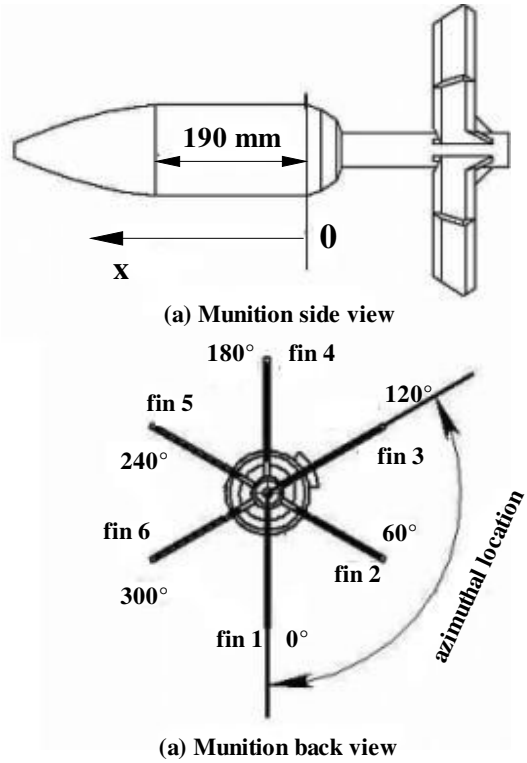

Figure 4-2: Side and back views of the STM model.

4.1.1 Baseline without fins results

To establish the uncertainty of the wind tunnel results, experiments on the baseline model at selected experimental conditions were repeated 5 times. Figure 4-1 shows examples of the 95% confidence intervals of the pitching moment and normal force results. Other results are expected to have confidence intervals similar in magnitude.

The coordinate system to be used in the result discussions is shown in Figure 4-2. Figures 4-4 to 4-14 show the subsonic experimental results for the no-fin baseline flow control, which are presented primarily in the form of coefficients of aerodynamic forces versus angles of attack, with the angles of attack ranging from $-10°$ to $10°$ at $1°$ increment.

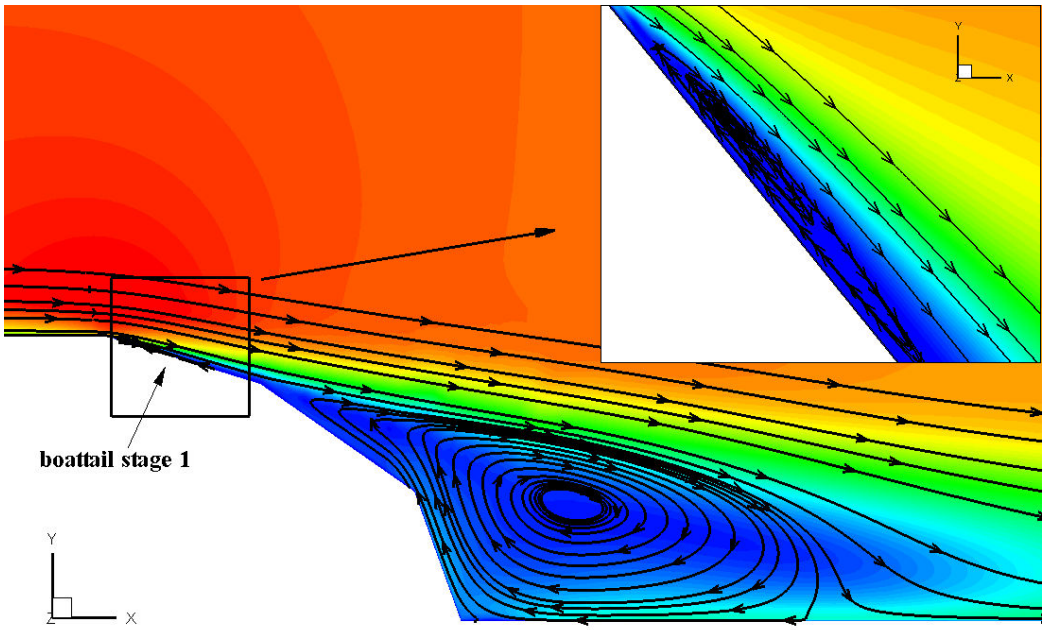

Figure 4-3: Contour of velocity magnitude and flow streamtraces near the boattail.

Figures 4-4 to 4-7 show results of a particular spoiler on top (180°) of the model and at various distances from the boattail. The starting position of the boattail of the main projectile body is used as the reference point for moment and is designated as the zero for the axial position. The distance shown in the legends indicates axial location of the spoiler upstream (positive) or downstream (negative) of the projectile boattail. The most effective control is obtained for distance ranges from 0 to 20 mm, and 60 to 185 mm. Within 20 mm upstream of the boattail, significant negative normal forces are generated at all tested angles of attack. Nose-down incremental pitching moments are produced especially at the tested angles of attack from $-10°$ to 4°, which is a result of the induced normal force being concentrated around the spoiler. With the same spoiler placed at a distance range from 60 mm to 185 mm, however, positive normal forces and nose-up pitching moments are observed. Thus, forces generated by the spoiler at these two distance ranges are opposite in direction. Experimental and numerical flow visualizations reveal that the flow past the boattail is separated at the first stage of the boattail, as shown in Figure 4-3. For the distance within 20 mm upstream of the boattail, flow separation is provoked and the flow remains separated past the boattail onto the fin tube. When the spoiler is placed upstream from the boattail, the separated flow from the spoiler will reattach to the model upstream of the boattail. Compared with upstream of boattail, spoilers located at downstream of the boattail produce less control effect as shown in Figures 4-6 and 4-7. This is because the spoiler is immersed in the wake of the boattail. Additionally, the diameter of fin tube is much smaller than that of main body. As such, spoiler placed on the fin tube has smaller arc length and the area of the unbalanced pressure caused by spoiler is much smaller than that on main body.

Figures 4-8 and 4-9 show results of spoilers placed just upstream of the boattail at azimuth locations from 180° to 90°. Except for the 150° case where control is ineffective at most angles of attack, all other cases show normal force and moment effects. The most effective configuration is with the spoiler on the top, which is

expected. Magnitudes of the normal force and pitching moment are mostly increased from the baseline for the 180° case, while the opposite is true for the 120° and 90° cases. The results presented in Figure 4-10 indicate no significant controls can be generated at any azimuth positions for a spoiler placed downstream of the boattail.

A preliminary study indicated that considerable yawing moments could be generated by placing the spoilers at certain azimuth locations. As shown in Figures 4-11 and 4-12, spoilers placed at 120° and 90° produce considerable yawing moments especially at angles of attack near −10° and 10°. The results also demonstrate that symmetric spoiler configuration should be applied if cross-coupling of moments is to be minimized.

Effects of height, with the spoiler placed at the most effective axial and azimuth locations, are compared in Figures 4-13 and 4-14. In the cases tested, negative normal force increments are produced for angles of attack from −10° and 10°. Except for the smallest spoiler, all others produce significant pitching moments at angles of attack from −10° and 4°. The largest control is produced by the spoiler with a height of 12.7 mm the highest one tested. It decreases the moment coefficient by 0.12 or 20.0% compared with the no control case, at the angle of attack of −10°. The control loses its effectiveness for angles of attack above 4°.

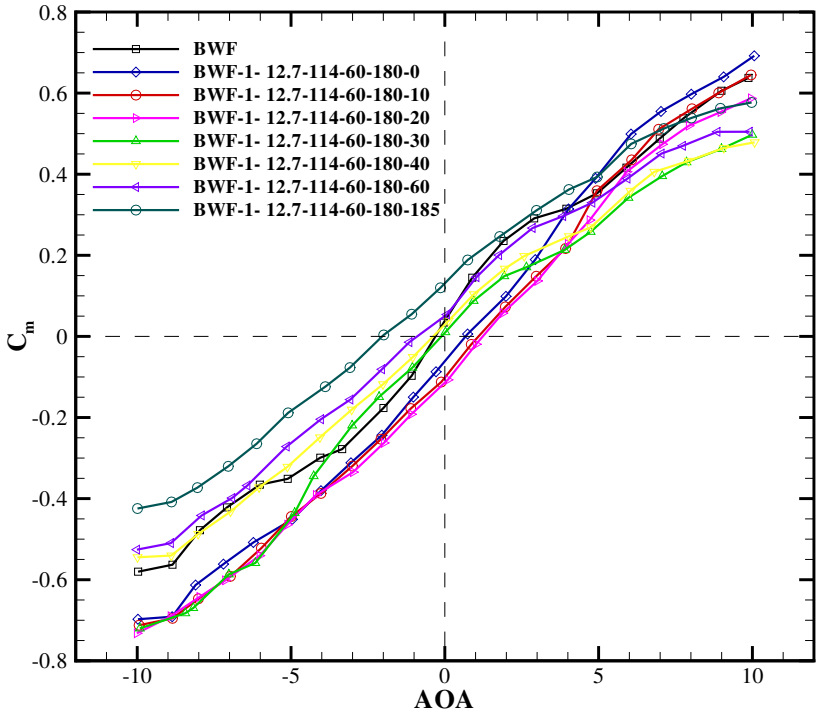

Figure 4-4: Effect of spoiler axial location at forebody on pitching moment coefficient as a function of angle of attack.

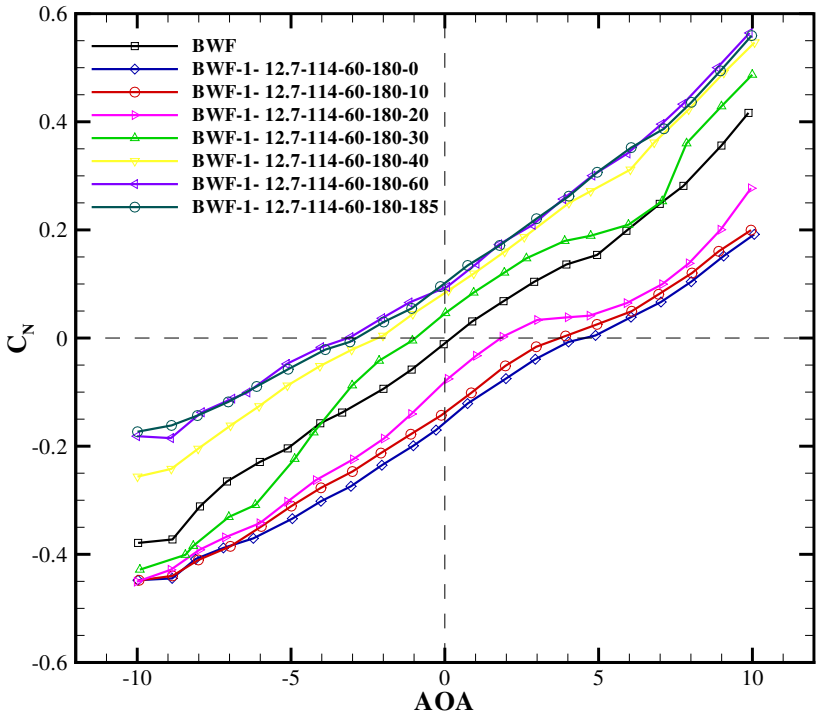

Figure 4-5: Effect of spoiler axial location at forebody on normal force coefficient as a function of angle of attack.

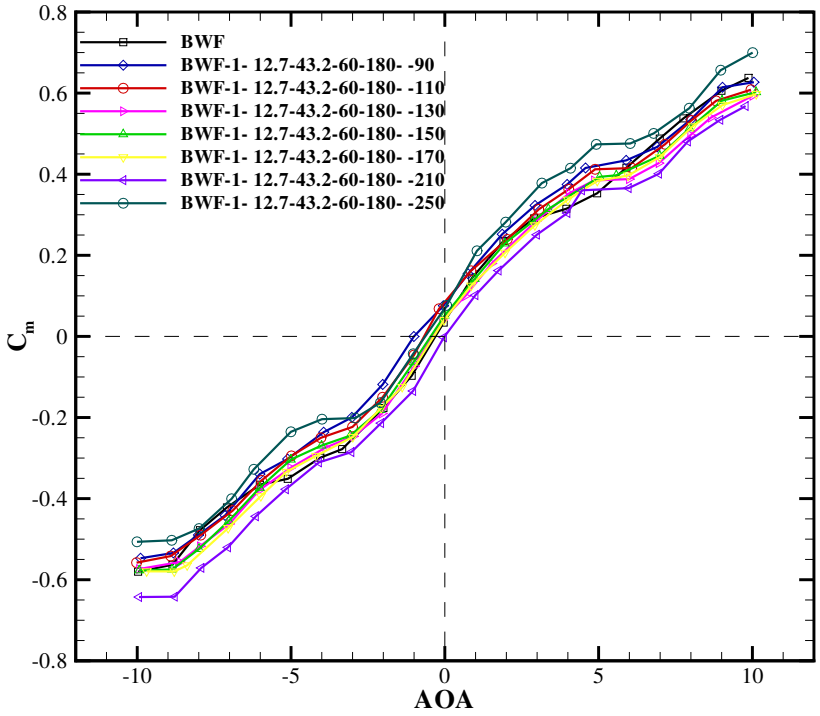

Figure 4-6: Effect of spoiler axial location at aftbody on pitching moment coefficient as a function of angle of attack.

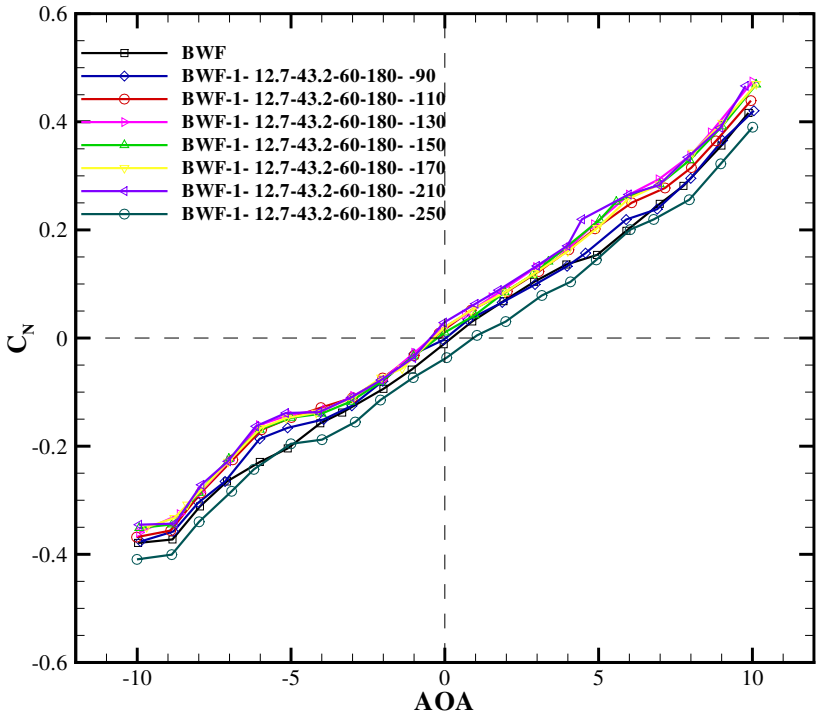

Figure 4-7: Effect of spoiler axial location at aftbody on normal force coefficient as a function of angle of attack.

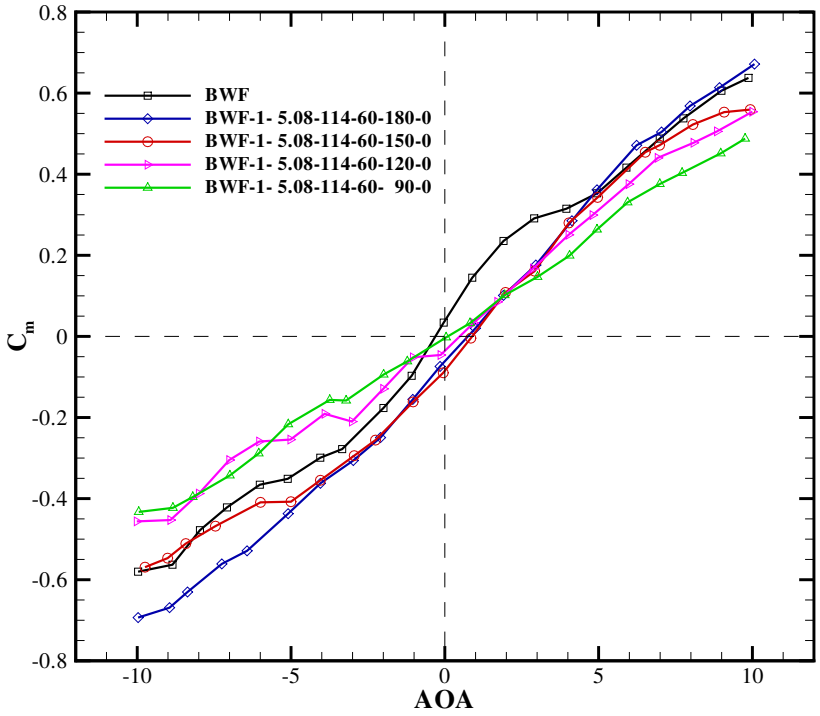

Figure 4-8: Effect of azimuthal location on pitching moment coefficient as a function of angle of attack using a spoiler mounted on boattail.

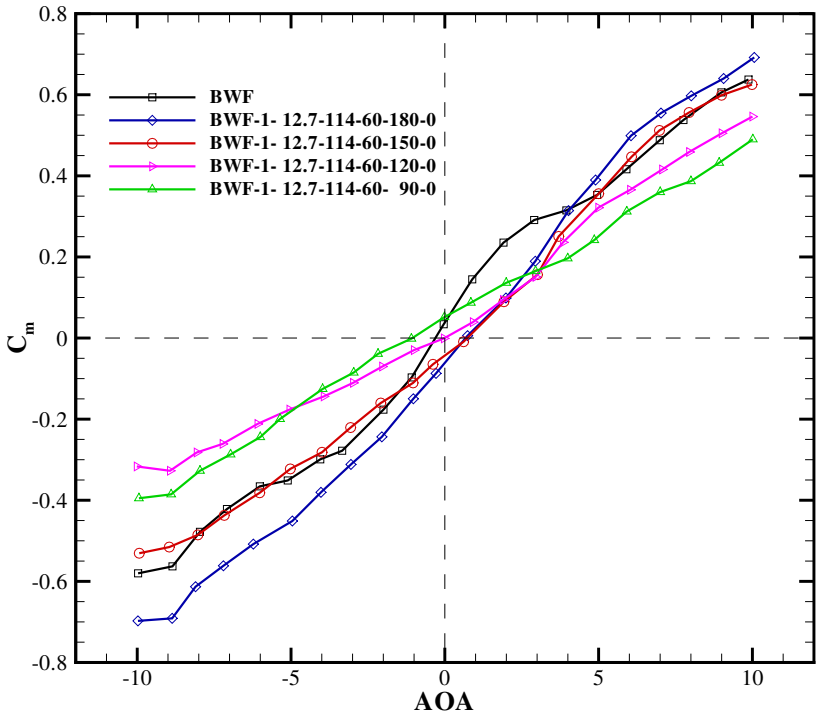

Figure 4-9: Effect of azimuthal location on pitching moment coefficient as a function of angle of attack using a spoiler mounted on boattail.

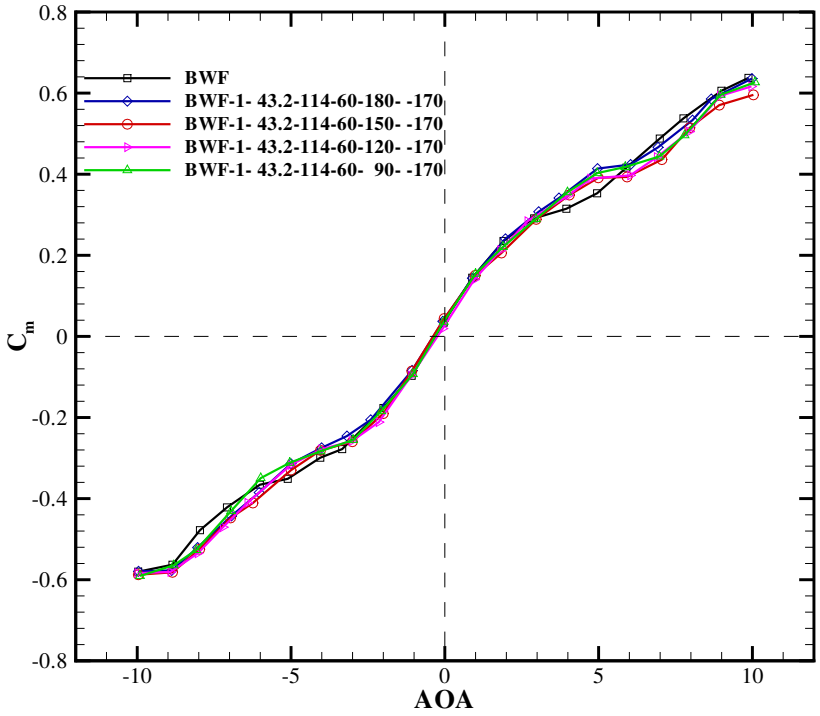

Figure 4-10: Effect of azimuthal location on pitching moment coefficient as a function of angle of attack using a spoiler mounted on tail piece.

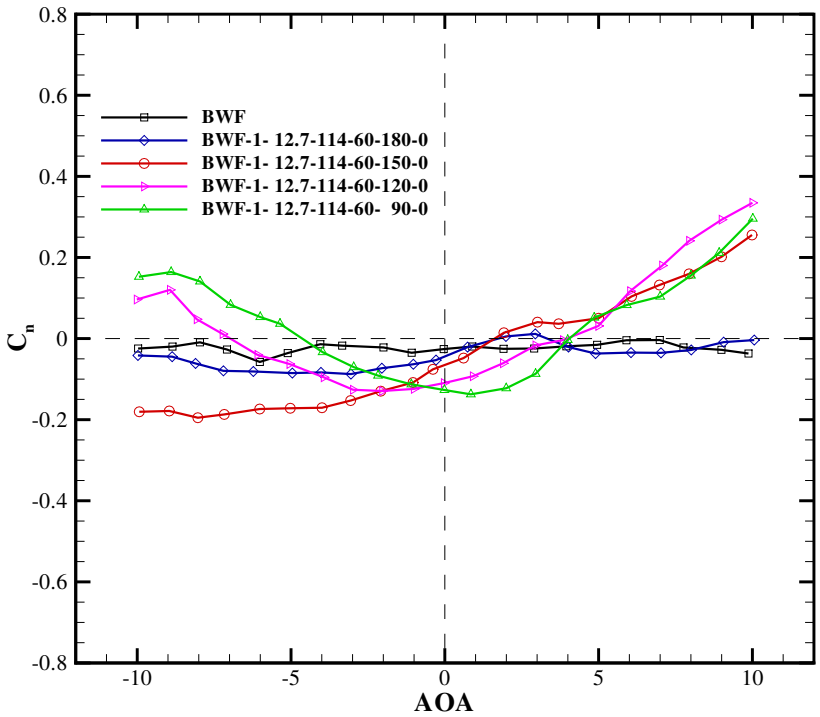

Figure 4-11: Side effect on yawing moment coefficient as a function of angle of attack caused by a spoiler mounted at varying azimuth locations.

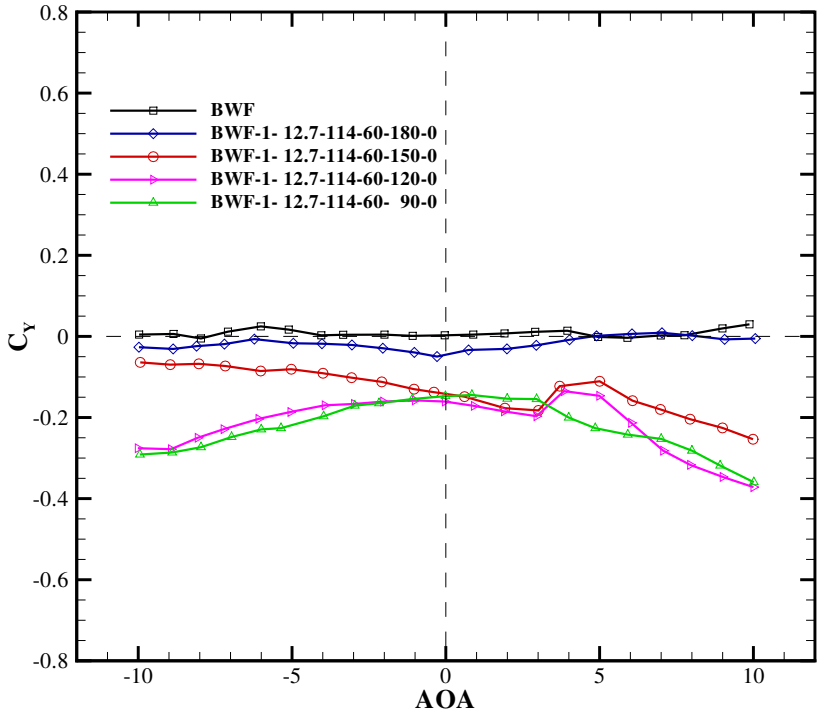

Figure 4-12: Side effect on side force coefficient as a function of angle of attack by a spoiler mounted at varying azimuth locations.

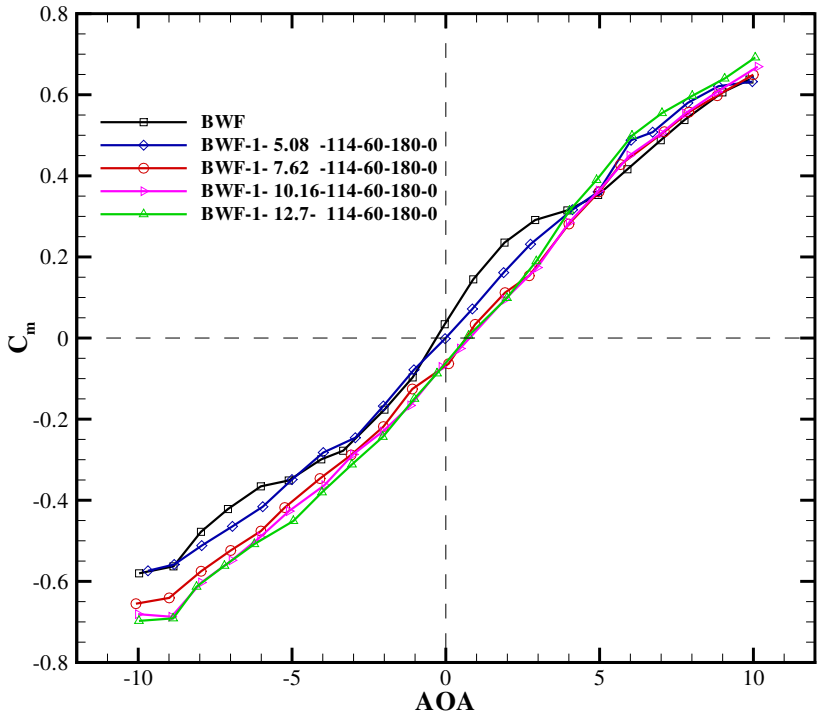

Figure 4-13: Effect of spoiler height on normal force coefficient as a function of angle of attack.

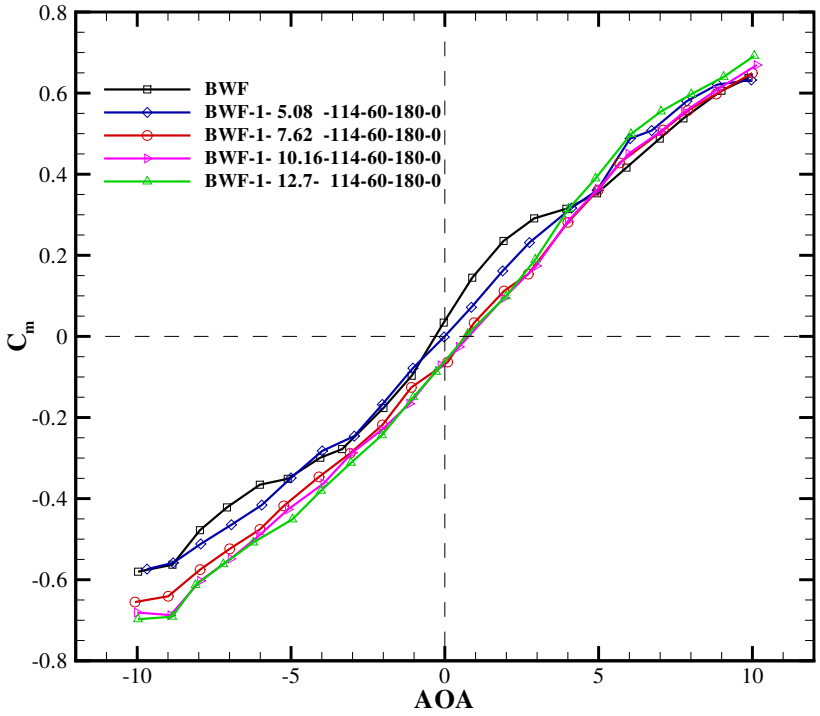

Figure 4-14: Effect of spoiler height on pitching moment coefficient as a function of angle of attack.

4.1.2 Baseline with Fins Results

Tail-fins are intended to provide nose-down pitching moments at positive angles of attack and vice versa to provide static stability in pitch, and similar effects in yaw. In contrast with the baseline without fins configuration, the baseline with fins case is pitch-stable. This is seen in the C_m vs. AOA relationship where the slope is negative.

To determine effective axial locations, a spoiler with 12.7-mm height and 60 arc-length was placed on the top of boattail. As shown in Figures 4-15 and 4-16, the area within 30 mm upstream of the boattail remains the ideal position for flow control, in that significant nose-down pitching moments are produced especially at the angles of attack from $-10°$ to $-2°$. For example, the pitching moment is reduced by 0.74 or 21.44% at the angle of attack of $-10°$, and at the angle of attack of $-2°$ the pitching moment is reduced by 0.28 or 17.1%. Within this range, no significant positional effect

is observed. This suggested reasonable freedom in positioning the spoilers. There is no competent pitching moments generated outside this range of axial locations. This is different with what detected in the study of baseline without fins, in which two effective ranges of axial locations observed. One is from 0 mm to 20 mm, and another is from 60 mm to 185 mm, before the center of gravity. As can be seen in Figure 4-16, downstream of the boattail is still not an effective control location to place the spoilers.

The effect of azimuth positions on control performance is illustrated in Figures 4-17 and 4-18. Spoilers with 127 mm and 5.08 mm heights produce significant pitching moments at arc-length locations from 180° to 120°. Obviously, the most effective location for generating pitching moment is with the spoiler on top (180°). At 90° the magnitudes of pitching moments generated by both spoilers are reduced to near zero, as would be expected.

At axial position of 0 mm and azimuth angle of 180°, effects of spoilers with various heights and arc-length are compared in Figures 4-19, 4-20 and 4-22. In all cases, nose-down pitching moment increments are produced for all tested angles of attack. Figure 4-20 is an enlarged view to show control results at angles of attack from 0° to 10°. Figure 4-21 shows the effect of spoiler height on the normal force as a function of angle of attack. As specified in the legend, the spoilers used are identical with the ones in Figure 4-19. The moment and normal force show that $-2°$ is a critical angle of attack where the spoiler-induced normal force increment changes from positive to negative. Much higher pitching moments are produced at angles of attack from $-2°$ to $-10°$ compared with other tested angles.

Similar results were obtained by using a reduced length spoiler, shown in Figure 4-22. The arc length of the spoilers was reduced from 60° to 45°, and a similar control effect was achieved but with reduced magnitude of pitching moment increments. Figure 4-23 compares the control results of spoilers with different arc-lengths. With a fixed height of 10.16 mm, the arc-lengths of the spoilers were changed from 60° to

30°. The results show the generated nose-down pitching moments is linearly increased by increasing the arc lengths. Even with the smallest arc length, significant pitching moment was produced.

Figures 4-24 and 4-25 compare the effect of spoiler shape on the pitching moment. A continuous spoiler is split into several triangle or rectangle pieces as illustrated in Figure 2-4. As such, the projectile drag induced by spoilers may be reduced. The results reveal that the continuous spoiler is still the most effective, and the spoiler with rectangle-shape pieces has identical control effect as the continuous one. This suggests the control is sensitive to the total arc-length, but not with the individual shape. As such, rectangle-shape spoilers may be employed for ease in assembly and multi-purpose control.

In general and as expected, larger magnitudes of control moments are produced with higher and wider spoilers. Furthermore, the results show that even for the spoilers with the smallest height (5.08 mm) or arc-length (30°), considerable effects on the pitching moment were observed especially at negative angles of attack. This suggests that the magnitude of generated control force can be modulated to a large degree by varying the spoiler size.

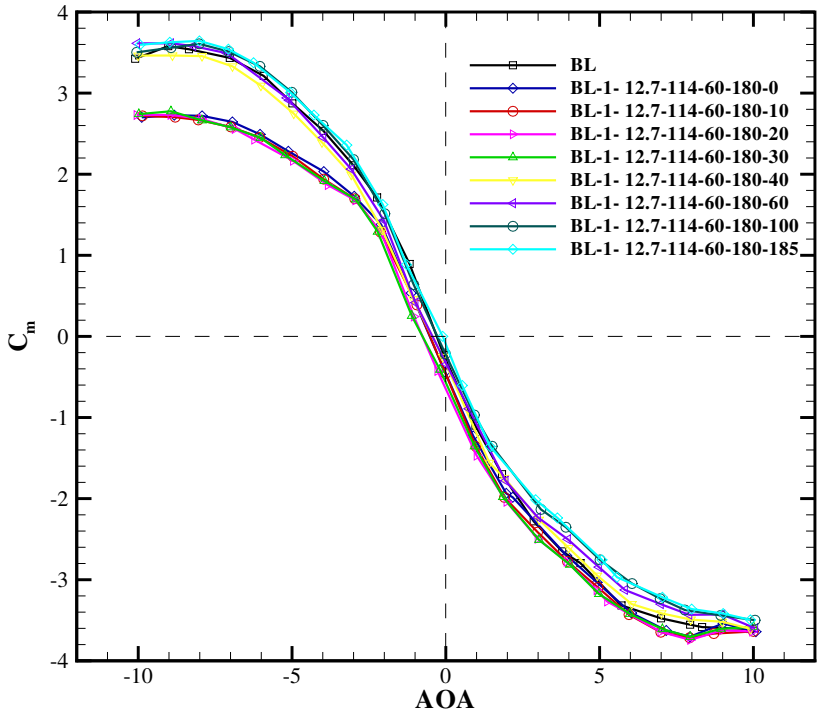

Figure 4-15: Effect of spoiler axial location at forebody on pitching moment coefficient as a function of angle of attack.

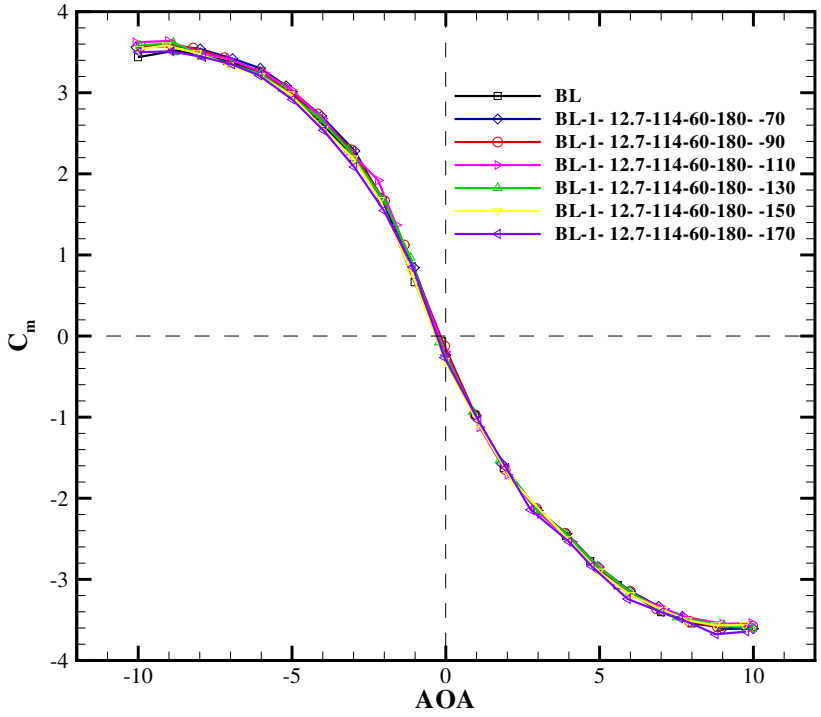

Figure 4-16: Effect of spoiler axial location at aftbody on pitching moment coefficient as a function of angle of attack.

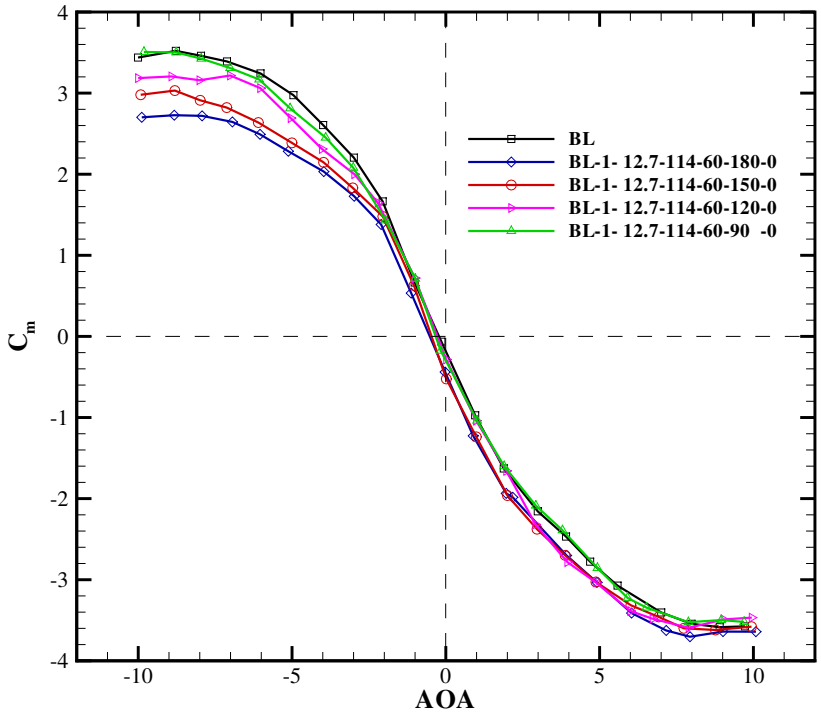

Figure 4-17: Effect of azimuthal location on pitching moment coefficient as a function of angle of attack using a spoiler mounted on boattail.

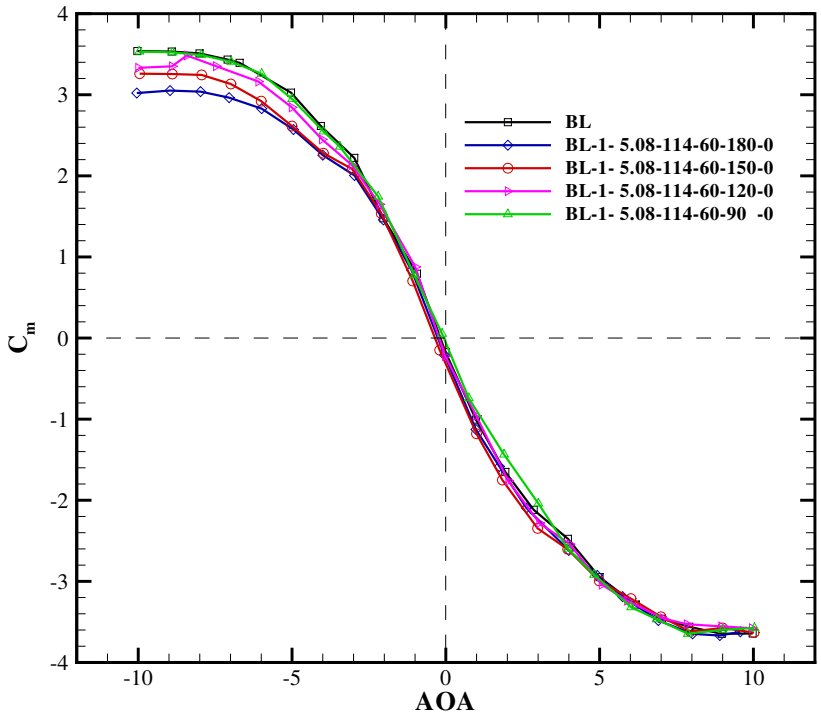

Figure 4-18: Effect of azimuthal location on pitching moment coefficient as a function of angle of attack using a spoiler mounted on boattail.

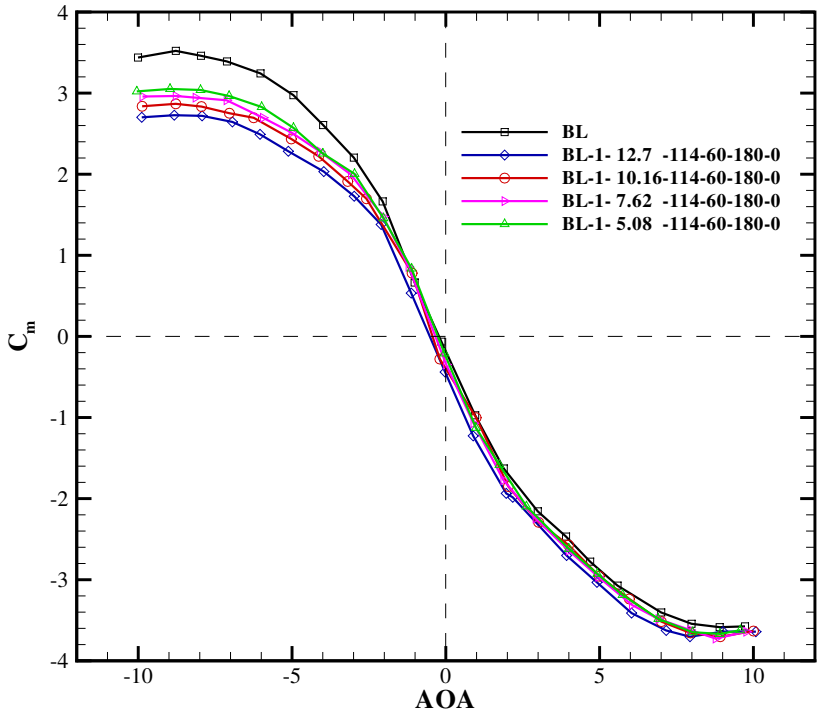

Figure 4-19: Effect of spoiler height on pitching moment coefficient as a function of angle of attack.

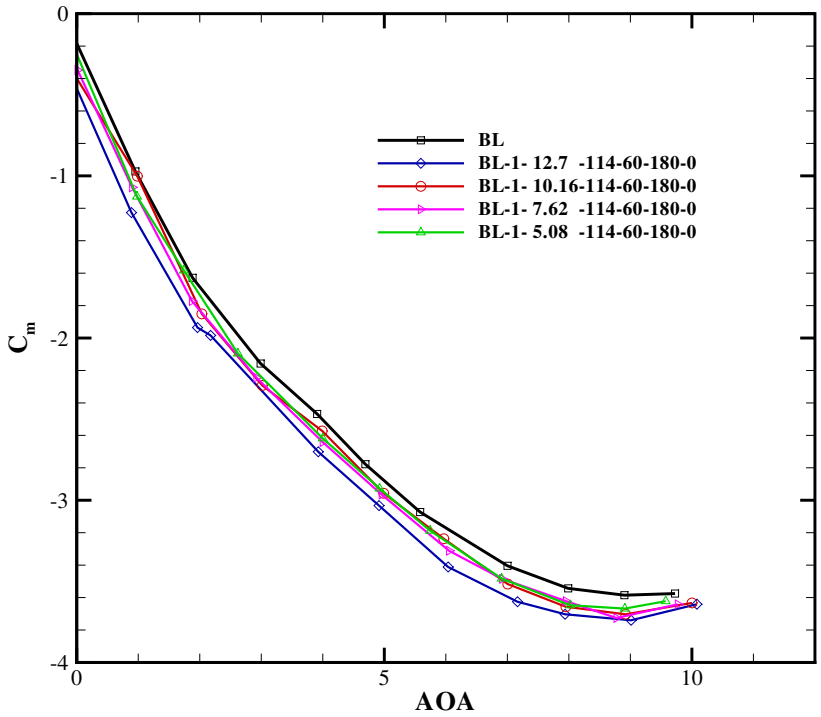

Figure 4-20: Enlarged view for results at positive angle of attack in Figure 4-18.

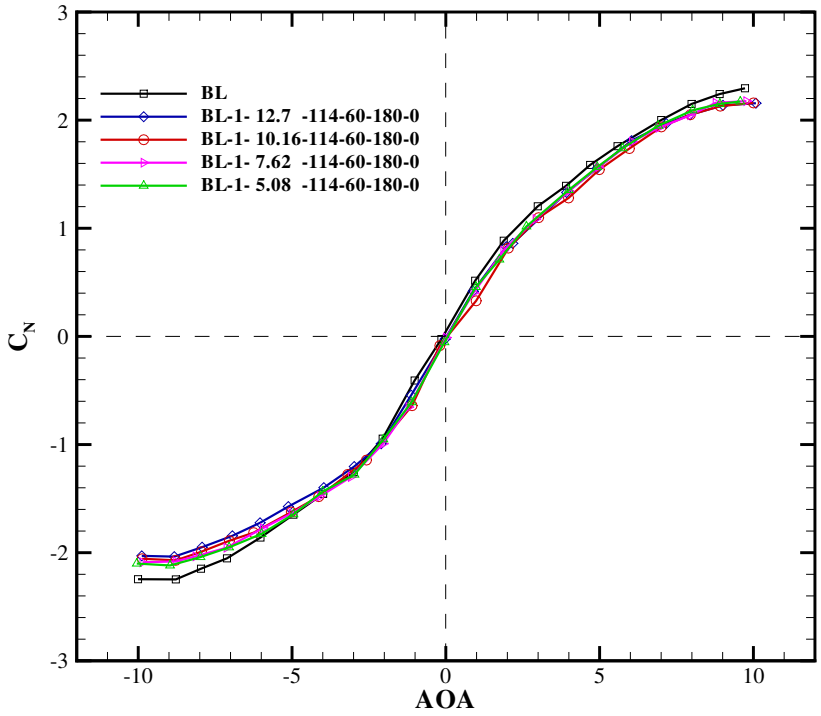

Figure 4-21: Effect of spoiler height on normal force coefficient as a function of angle of attack.

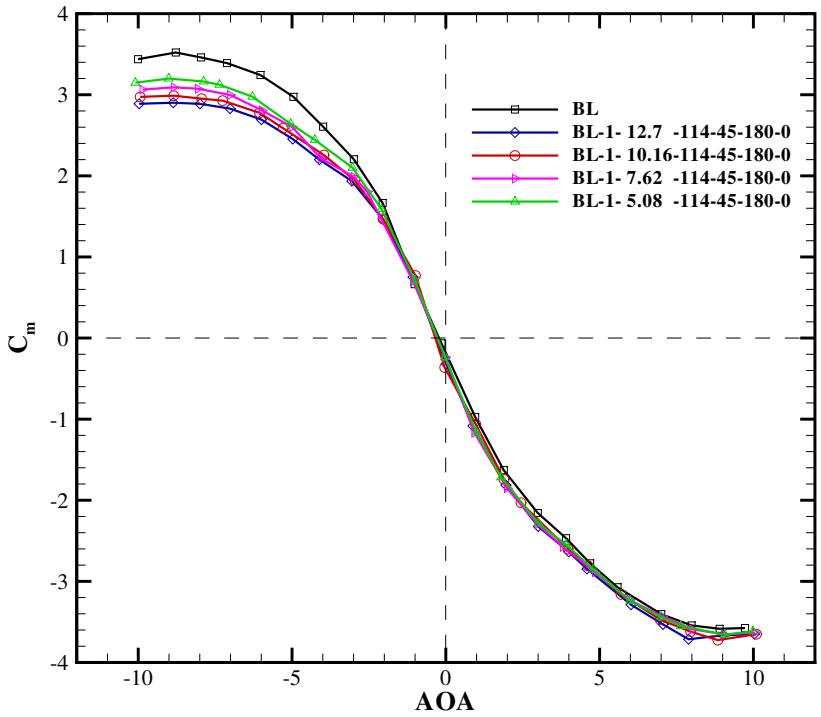

Figure 4-22: Effect of spoiler height on pitching moment coefficient as a function of angle of attack.

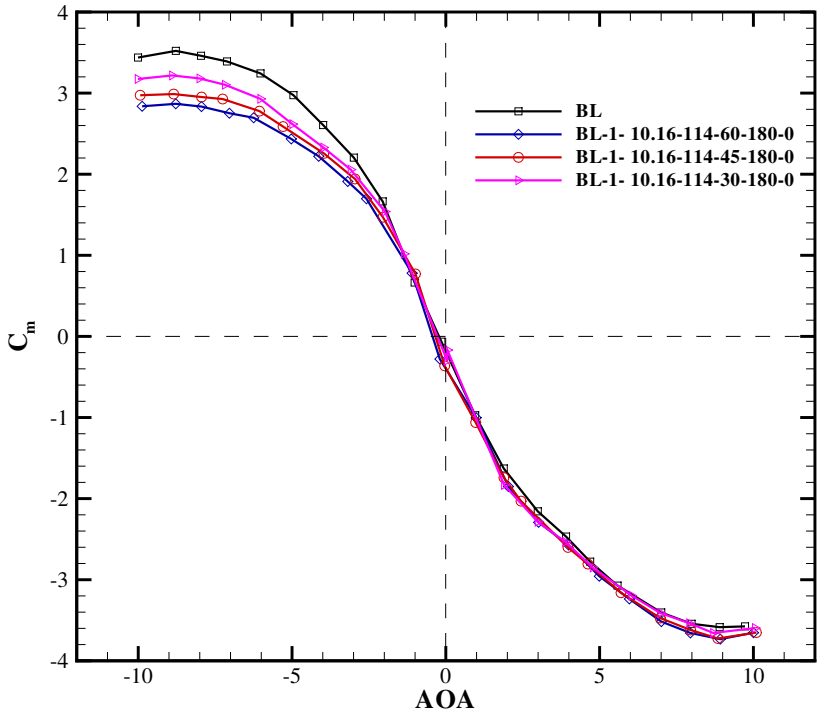

Figure 4-23: Effect of spoiler length on pitching moment coefficient as a function of angle of attack.

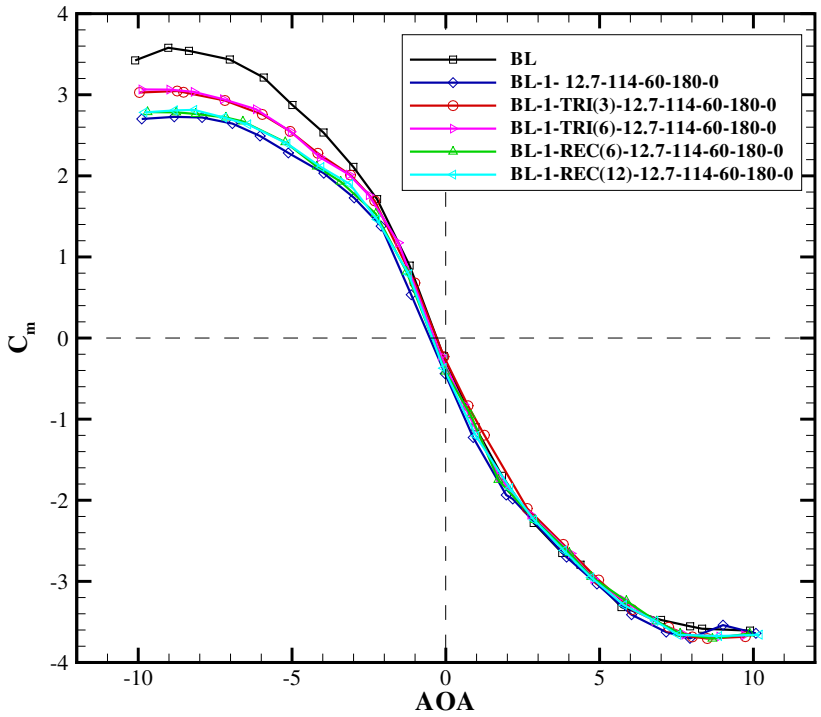

Figure 4-24: Effect of spoiler shape on pitching moment coefficient as a function of angle of attack.

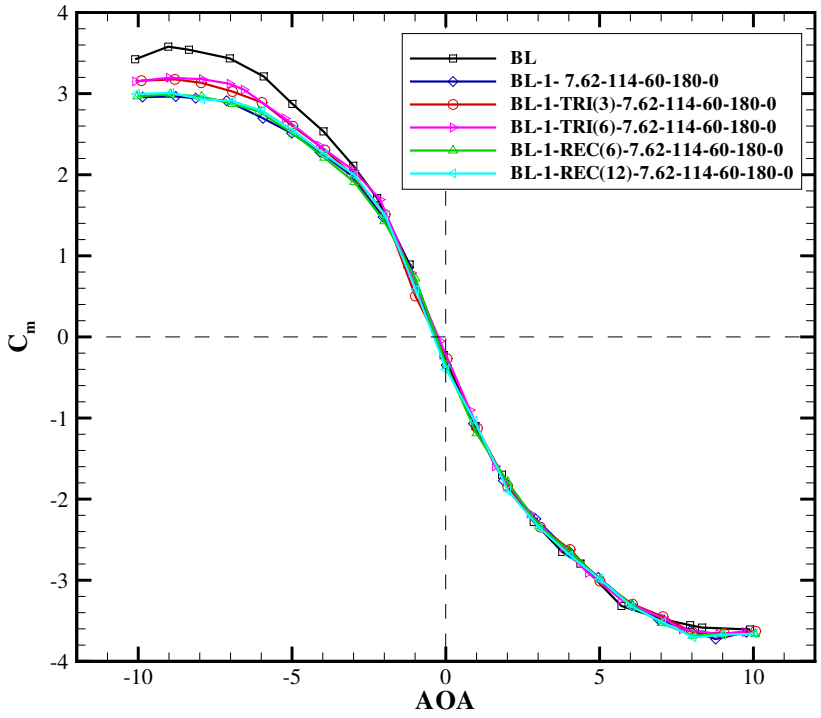

Figure 4-25: Effect of spoiler shape on pitching moment coefficient as a function of angle of attack.

4.2 Numerical Results

4.2.1 Grid Independence Study

Coordinates used in numerical result discussions are shown in Figure 4-26. Grid Independence studies were conducted to determine the ordered discretization error in the CFD simulations. For the baseline (finless) with control case, a mesh with 2,856,460 cells was first generated. Next, the grid points in circumferential direction were doubled, which resulted in a finer grid with 5,447,320 cells. The solutions of velocity profiles in the wake region and pressure distributions on the model surface along the axial direction were compared in Figures 4-27 and 4-28, and 4-29 for the two grids.

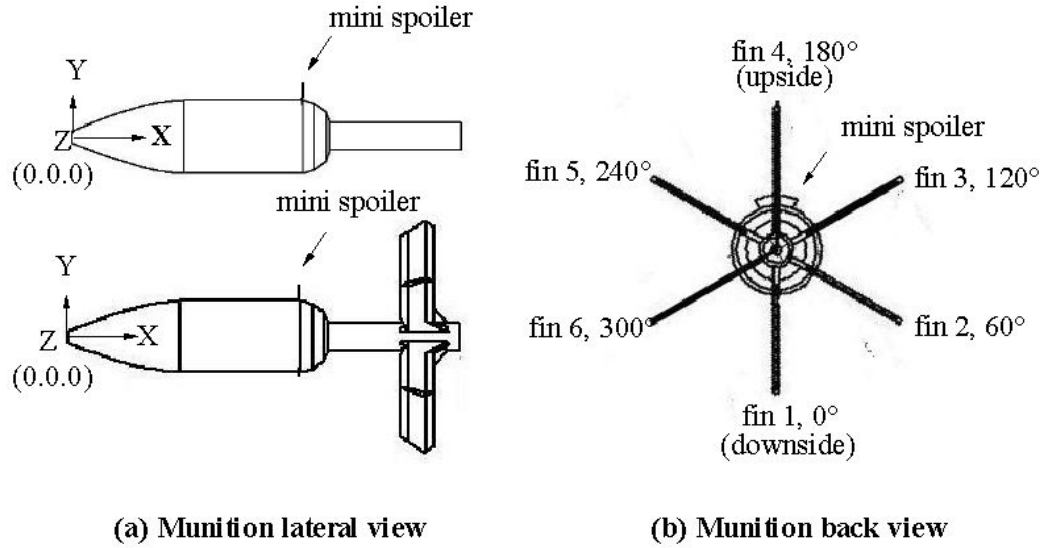

Figure 4-26: Coordinates used for computational simulations.

The most effective control configuration for the baseline (finless) model is used in this grid independence study. Specifically, a spoiler, 10.16 mm high and 60° long is placed on the top (180°) of the main body just before the boattail. The combined model and spoiler is longitudinally symmetric at the z plane (left and right sides, z

= 0). The wake flow is therefore expected to be symmetric at z plane as shown in Figure 4-27. Figures 4-27 and 4-28 show that the velocity profiles predicted using these two grids is almost identical except for small deviations in the core wake region (near z=0). Figure 4-29 compares the axial distributions of pressure on the surface of the projectile as predicted by using these two grids. The pressure distribution is important since it directly determines the aerodynamic control forces on the model. Figure 4-29 shows there is no significant difference between results using the two grids. The comparison results of velocity profiles and pressure distributions thus indicate the solution become independent for grid sizes larger than the coarser grid. As such, the coarser grid is used for all other studies.

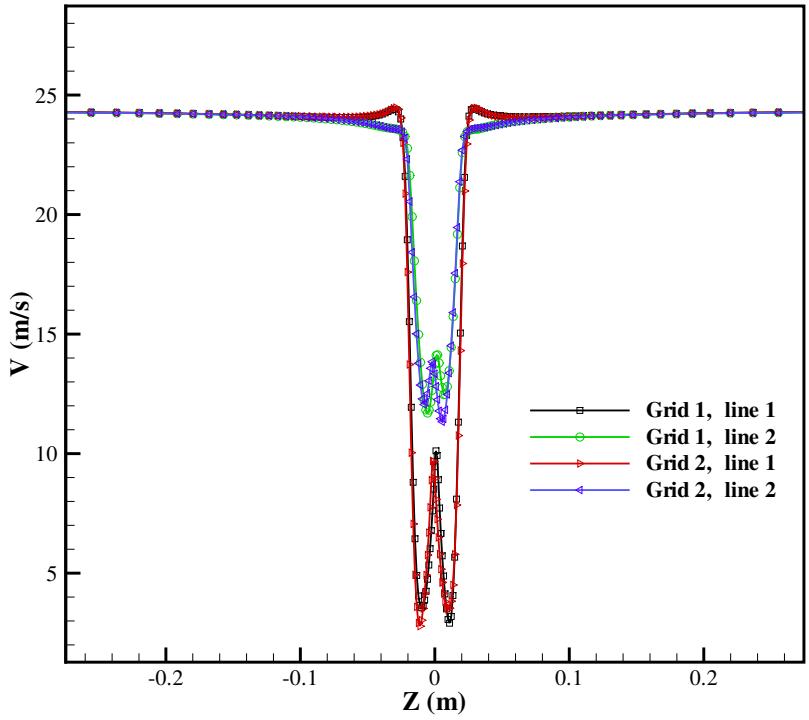

Figure 4-27: Comparisons of velocity profiles of cross lines on Y plane of symmetry predicted by coarse and fine meshes.

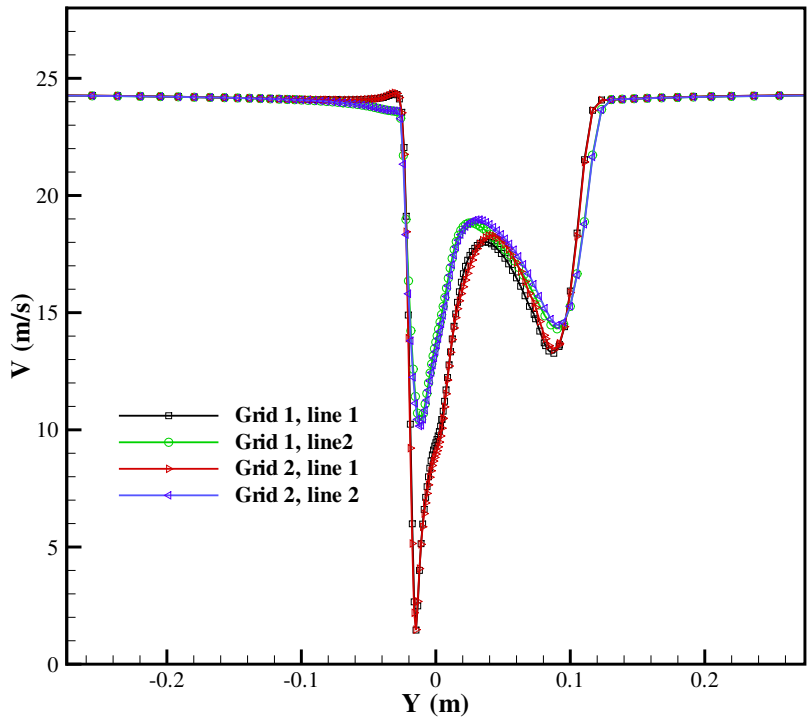

Figure 4-28: Comparisons of velocity profiles of cross lines on Z plane of symmetry predicted using coarse and fine meshes.

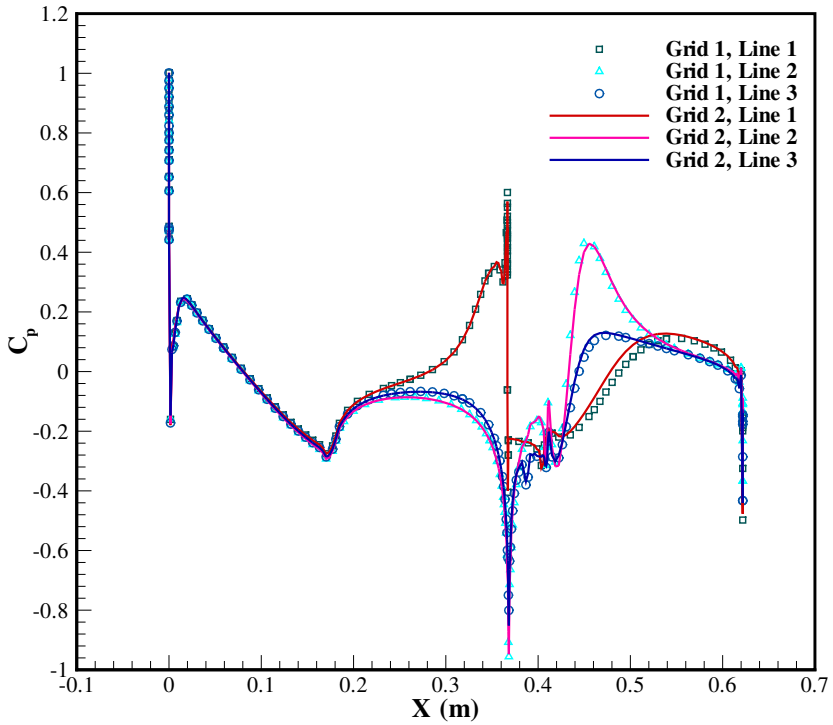

Figure 4-29: Comparisons of pressure distributions on model surface predicted using coarse and fine meshes.

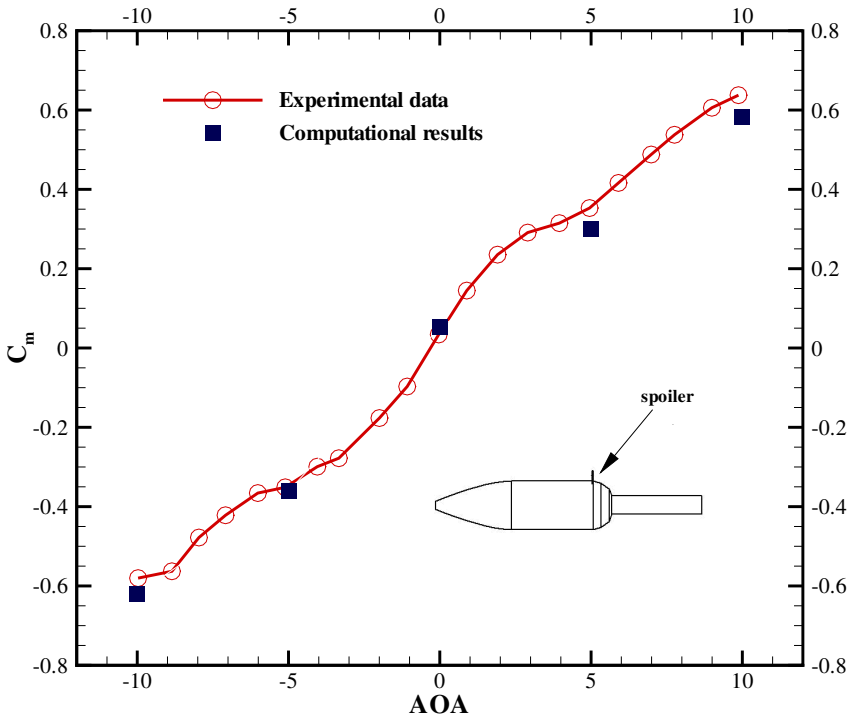

Figure 4-30: Experimental pitching moment coefficient versus computational results for finless baseline with control.

4.2.2 Simulation Validation

Simulation validation was conducted by comparing CFD results with experimental data, with quantified errors and uncertainty estimates obtained for both. Figure 4-30 shows a comparison of experimental results against numerical data for the same configuration used in the grid independence study. The moment predicted by CFD compare well with the experimental measurement with reasonable magnitudes of deviation. Based on experimental error analysis, the 95% confidence interval for the pitching moment coefficient is ± 0.02 for the finless baseline configuration. The CFD predicted pitching moments at 0° and -5° is within this error range. At other angles of attack, however, the deviations are out of the error range. The deviations are due to the inherit uncertainties of both the experimental and numerical methods, as well as geometry simplifications in numerical modeling. For example, the model is opened

at the end for the experiment but it is closed in the simulation in order to decrease the grid size.

Subsonic simulations were carried out to study the flow pattern associated with spoiler-induced pressure modification around the projectile, the function of the fins, and the effect of the angle of attack. The spoiler was placed at the most effective location as described before.

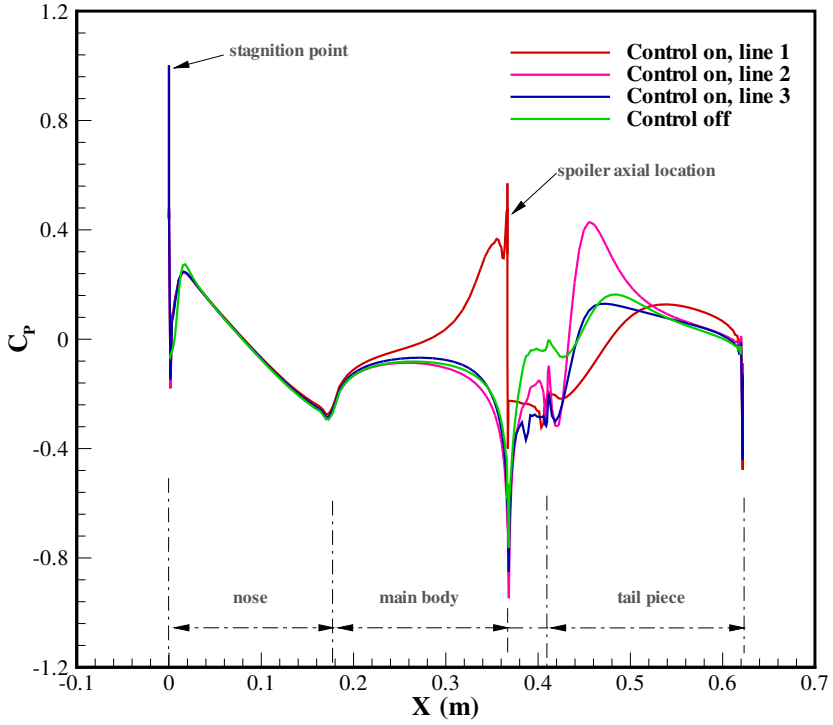

Figure 4-31: Pressure coefficient profiles along axial cross-lines for finless baseline configurations.

4.2.3 Baseline (Finless) Control

Figure 4-31 compares the pressure coefficient distributions of the finless model with and without control at 0° angle of attack. The green line represents the pressure loadings when the control is off. X axis shows the positions in the model axial direction, and y axis the local pressure coefficients calculated using the gauge pressure. The stagnation point shown in the figure is at the center point of the model at the

y-z plane at x/L=0, which is expected for both control on and off cases.

A sharp pressure rising was observed in the front of the nose from 0 mm to 20 mm. An analysis of the flow patterns in this region showed the flow separated and reattached almost immediately. Thus, a closed-type flow separation, induced by the blunt nose, was produced. This so-called nose-induced separation of the axial flow [18] creates reattaching flow on the aft body, thereby delaying the development of the open-type flow separation on the aft body with associated body vortices. Downstream of the initial nose separation, the boundary layer redevelops and the flow accelerates along the nose section that features a smoothly increased diameter. Correspondingly, the surface pressure decreases steadily over the same distance to the end of nose. The flow then decelerates around the connection of nose and main body and the pressure rises. The adverse pressure gradient is insufficient to separate the axial flow. After the steadily pressure rising, the pressure reaches a nearly constant level on much of the constant diameter section of the main body.

As can be seen in Figure 4-31, the pressure distribution at the aft portion of the body is far more complex than the one at the forebody. Shortly before reach the boattail the flow accelerates resulting in a sharp pressure drop. Over the boattail section the diameter decreases rapidly resulting in a sharp pressure rise. As a result, a strongly adverse pressure gradient is produced leading to flow separation. The flow eventually reattaches at the tail piece.

Simulation visualizations were conducted to study details of the flow patterns. Figure 4-32 compares the flow velocity contours near the model for control off and control on, while flow-spoiler interactions are illustrated in Figure 4-33 which shows the 2D velocity vectors, colored by velocity magnitudes, underlayed with a background of pressure coefficient contour. The boattail connected with the main body features three reducing-diameter stages, with each stage having a linear slope. Figure 4-32 shows he flow separates at the front portion of first stage, which affects the flow and pressure. The flow eventually reattaches at the fins tube resulting in a recirculating

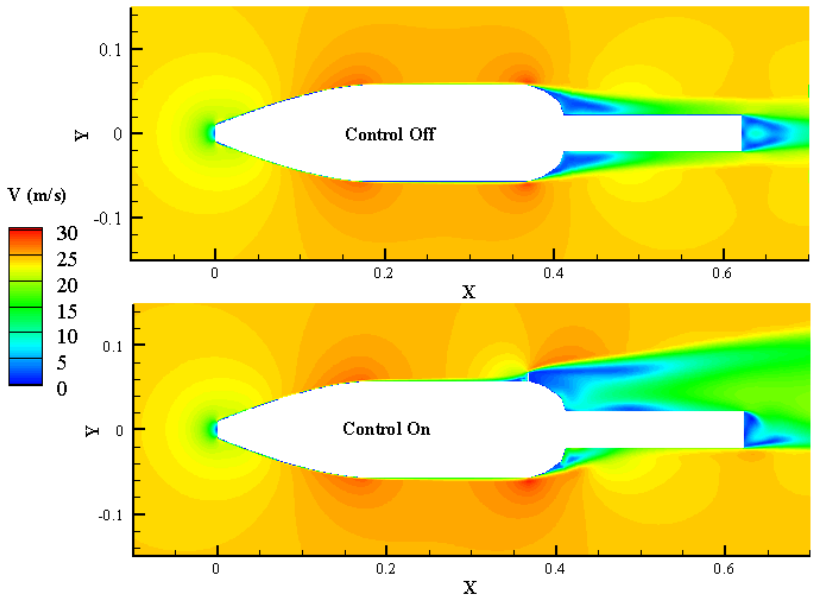

Figure 4-32: Contours of velocity magnitudes of the flow around the model without and with control.

flow zone at the corner between boattail and tail piece. The flow separation and recirculation happening in this region are complex and three dimensional.

Figures 4-32 and 4-33 show the flowfield is significantly changed when the spoiler is deployed. Flow velocities at the upper surface and downstream of the main body are obviously modified, which correspond to the pressure variations shown in Figure 4-31. The pressure on the upper surface of the main body is raised because of interactions. Interactions between the incoming flow and the spoiler not only increase the pressure near the spoiler, but also all the way to the front of main body. As a result, the pressure on a large portion of the upper surface is increased. Within comparison to the upper surface, the lower-surface pressure and side-surface pressure slightly decreases and increases respectively. The aft body pressure is also considerably changed due to flow-spoiler interactions.

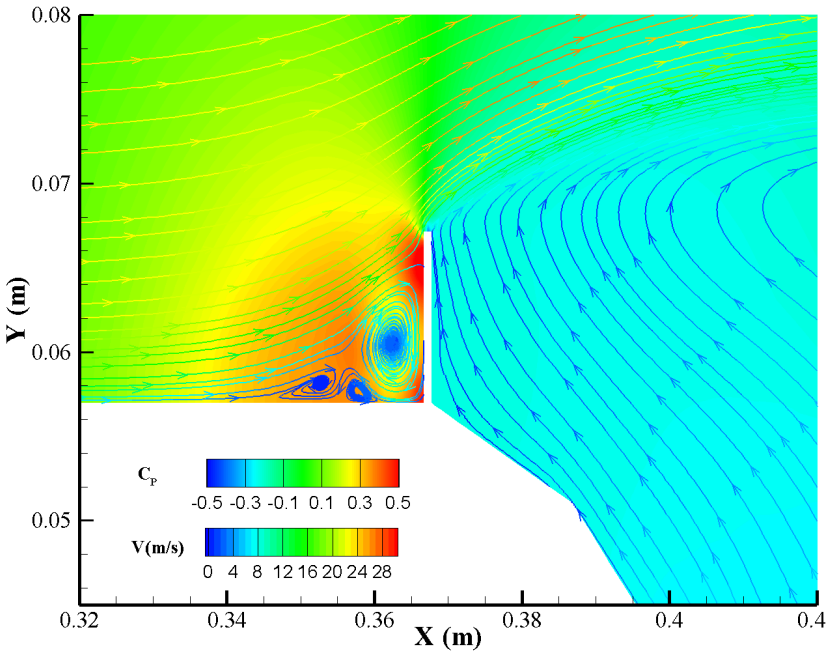

Figure 4-33: Contours of pressure coefficient and streamtraces colored by velocity magnitude upstream and downstream of the spoiler.

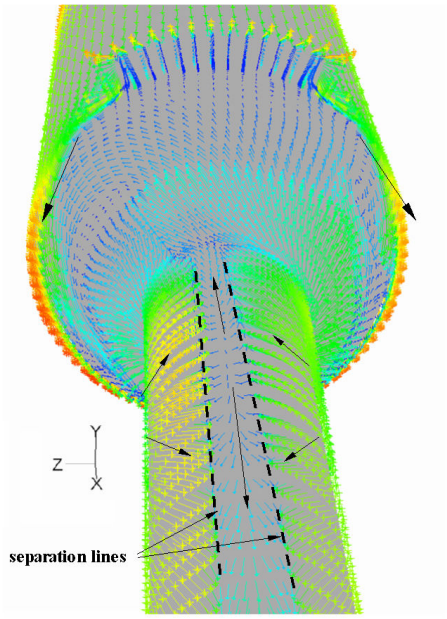

Figure 4-34: Velocity vector display colored by velocity magnitude at aft body on an ISO cell-wall surface.

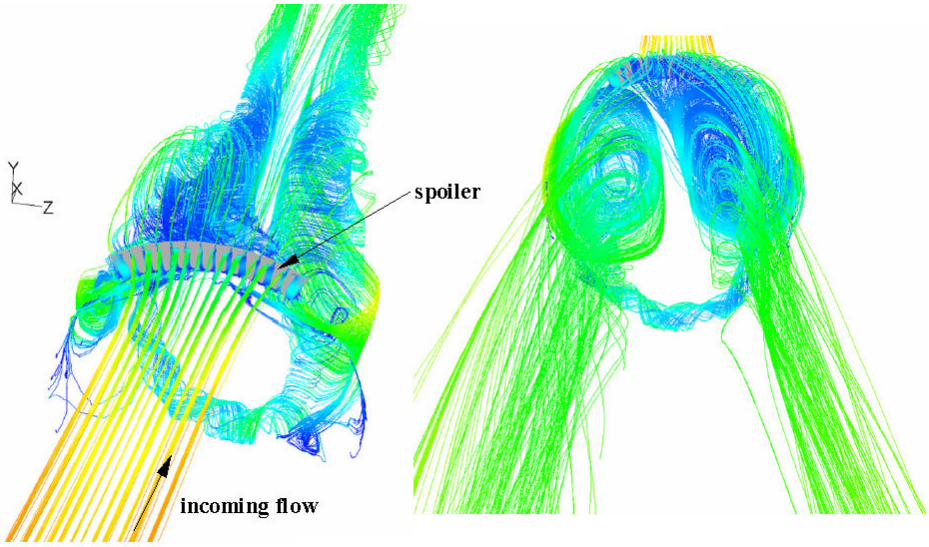

Figure 4-35: Pathlines for the flow directly impinging with the spoiler.

The pressure distribution on the boattail is quite complex. Generally, the control-on pressure is less than control-off. There is a positive pressure peak (line 2 in Figure 4-31) on the lower surface of tail piece. Due to flow-spoiler interaction, the flow is highly three dimensional with a considerable cross flow component. Consequently, the lower surface boundary layer on the tail piece after the separation zone is made thinner compared to the no-control case. This thinner boundary layer and the external flow, with a remarkable cross component, bring the lower surface pressure higher than upper. For the controlled baseline finless model, positive and negative normal forces are generated at forebody and aftbody respectively.

The flow pattern near the model surface is shown in Figure 4-34 where 3D velocity vectors are displayed on a cell surface. The isosurface is 0.1 mm away from the model surface, ensuring the surface to be located inside boundary layer. The axial-component dominated flow impinges on the spoiler, and is deflected to the sides and upward. The flow accelerates, around this spoiler-induced fluidic obstacle, and a cross-stream velocity component is induced. As shown in Figure 4-33, there is a separated zone immediately downstream of the spoiler. Figure 4-34 shows the separated flow interacts with the near-wall incoming flow, forming a three-dimensional recirculation

bubble that aligns approximately parallel to the boattail. It also can be observed that lower surface flow has a considerable cross flow component, and the resultant flow is upstream towards the boattail and tail-piece corner. Farther downstream, the resultant flow direction switches to downstream. At the tail-piece the cross flow separates. Two separation lines form as a result, and are presented black dished lines in Figure 4-34.

Pathlines for the flow directly impinging on the spoiler are shown in Figure 4-35. The incoming flow hits the spoiler and separates. Downstream of the spoiler, the separated flow forms a pair of vortices. The spiral vortices interact with the flow from other circumferential locations to form the aft body wake flow. Figure 4-36 shows this wake flow can be significantly influenced by the angles of attack.

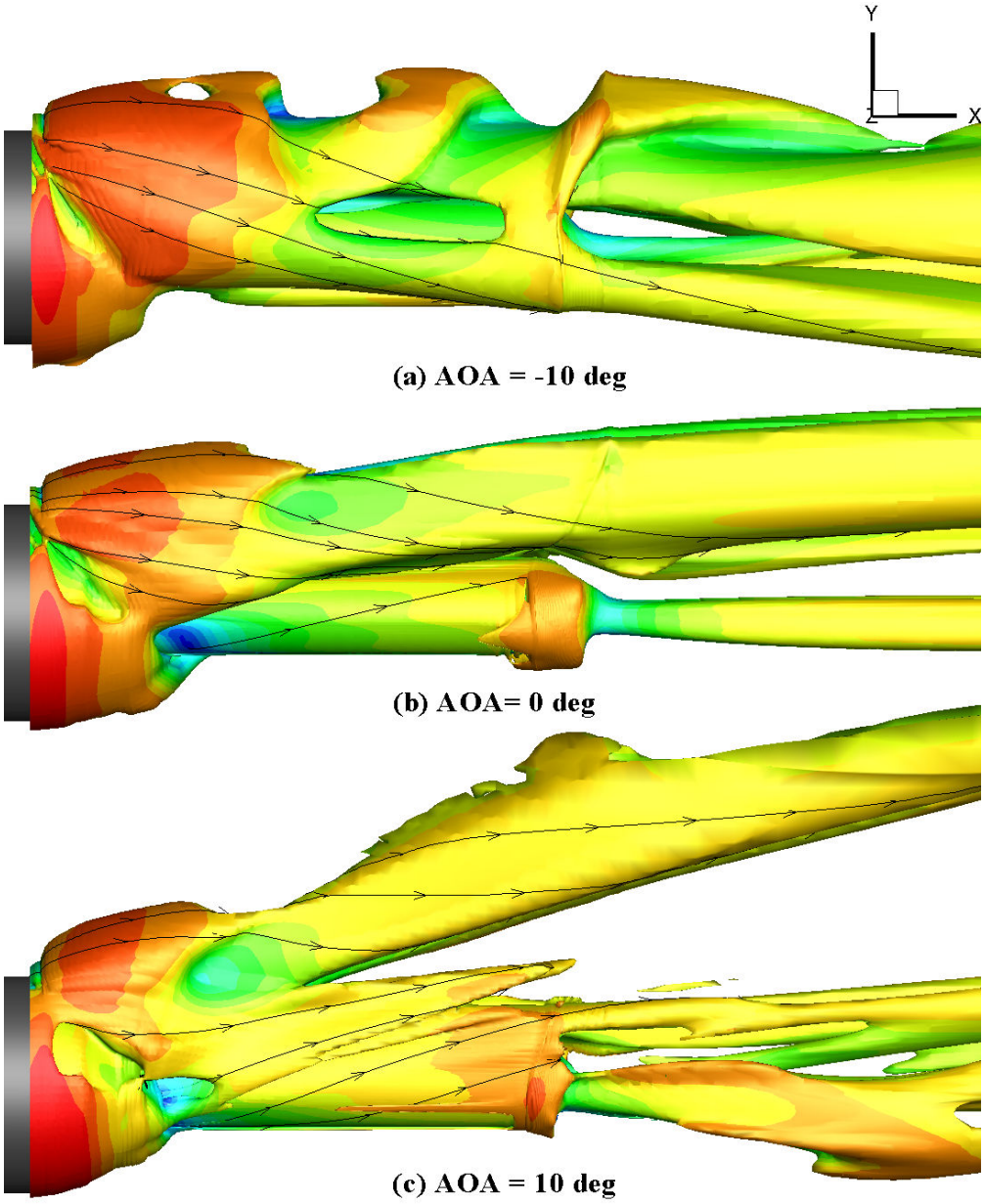

Figure 4-36: Visualizations of Votical flow downstream of spoiler at angles of attack using streamtraces and isosurfaces of Q-criterion (Q=1000) colored by velocity magnitude (side view).

4.2.4 Spinning Finless Baseline Simulation

As mentioned before, the finned STM projectile is stabilized during flight by static aerodynamic forces acting. Although projectile spin does not contribute to the stabilization of finned projectiles, a low rate of roll, about 18 revolutions per second around the longitudinal axis, is designed to minimize the adverse effects of mass and configurationally asymmetries that may result from material imperfections and manufacturing tolerances. Herein, spinning finless baseline simulations were conducted to study the spinning effect on the drag and rolling moment. The results can potentially be used in future projectile shell design, such as determining the spin reduction ratio due to friction, and serve as a building bloc for simulations of the model with fins.

In this dynamic simulation, a moving reference frame technique in FLUENT is employed. The principal reason for employing a moving reference frame is to render a problem which is unsteady in the stationary (inertial) frame steady with respect to the moving frame. For a steadily rotating frame (i.e., the rotational speed is constant), it is possible to transform the equations of fluid motion to the rotating frame such that steady-state solutions are possible. By solving these equations in a steady-state manner, the flow around the moving parts can be modeled.

To apply the multiple reference frame approach, the computational domain is broken up into two zones with a cylindrical interface. To minimize the computational error, the interface is 2 diameters away from the center line of the finless model. The freestream flow speed is at Mach number of 0.07, which is identical to the speed for planned experiments. The spinning speed in the simulation is varied from 2 rev/s to 227 rev/s.

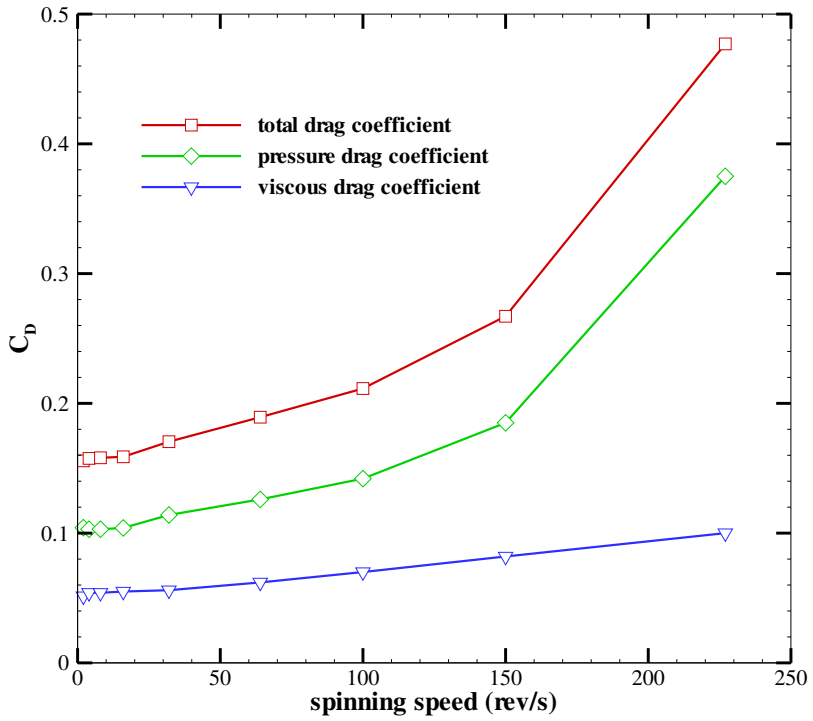

Figure 4-37: Drag coefficient versus spinning speed for finless baseline.

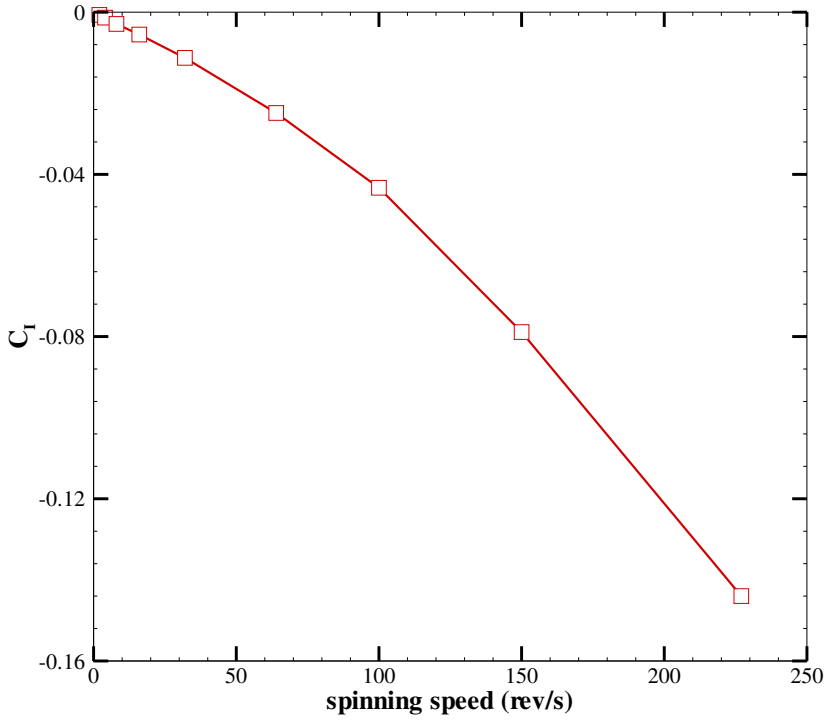

Figure 4-38: Rolling moment coefficient versus spinning speed for finless baseline.

Figure 4.36 shows the drag coefficients versus the spinning speeds. For spinning speeds from 2 to 16 rev/s, the drag coefficient remains essentially unchanged. Above 32 rev/s, the total drag coefficient increases with the spinning speed. The relationship is nonlinear, which is caused mostly by the nonlinearity of pressure drag. As shown in Figure 4-37, the viscous drag increases close to linearly with the spinning speeds, while pressure drag is not. This is because the circumferential-flow component increases with spinning speed, which changes the behavior of the flow separation and thus the pressure distribution at boattail. As a result, the pressure drag is significantly increased. In contrast to drag coefficient, the rolling moment coefficient increases linearly with the spinning speed as shown in Figure 4-38. This is expected as the rolling moment is only influenced by the viscous drag component in circumferential direction.

4.2.5 Control for the Configuration with Fins

Steady 3D RANS computational simulations were conducted to evaluate the control performance for the finned configuration at subsonic speeds. The Wake-Fin Tailoring method has been demonstrated to be effective for providing controlled-pitching moments for the chosen model in subsonic wind tunnel studies. Herein, numerical simulations, combined with experimental flow visualization, were performed to explore the associated flow physics and control mechanism. The configurations simulated are the finned baseline with and without controlled. A spoiler 12.7 mm in height and 60° in arc-length is placed on the top (180°) of boattail, as presented in Figure 4-39. The effect of angle of attack was not investigated in this part of study, and all the results to be presented were obtained at an angle of attack of 0°.

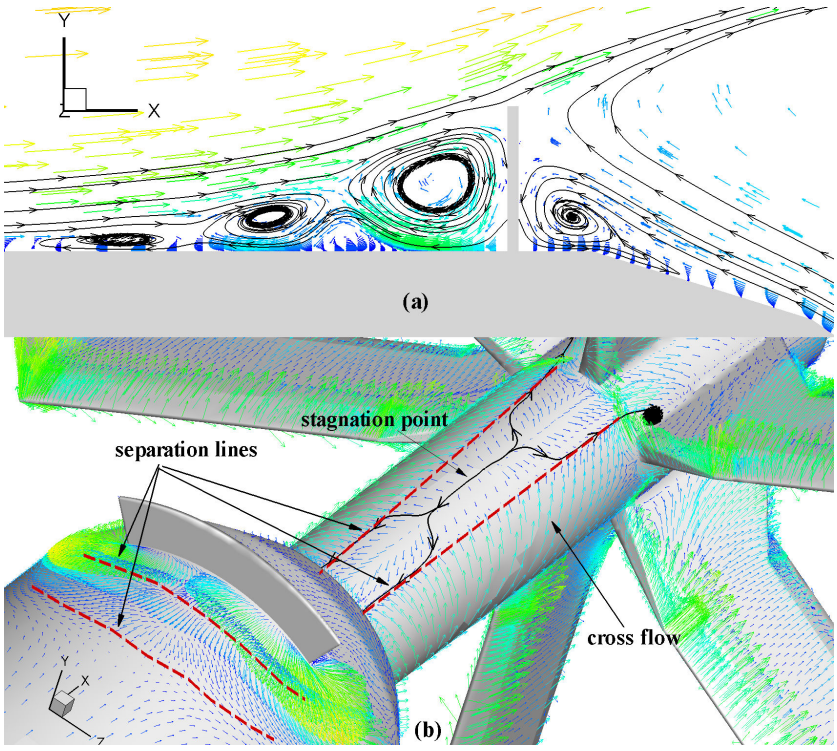

Figure 4-39: Velocity vector display colored by velocity magnitude together with flow streamtraces near the spoiler on z-cross section (a) and an ISO cell-wall surface (b).

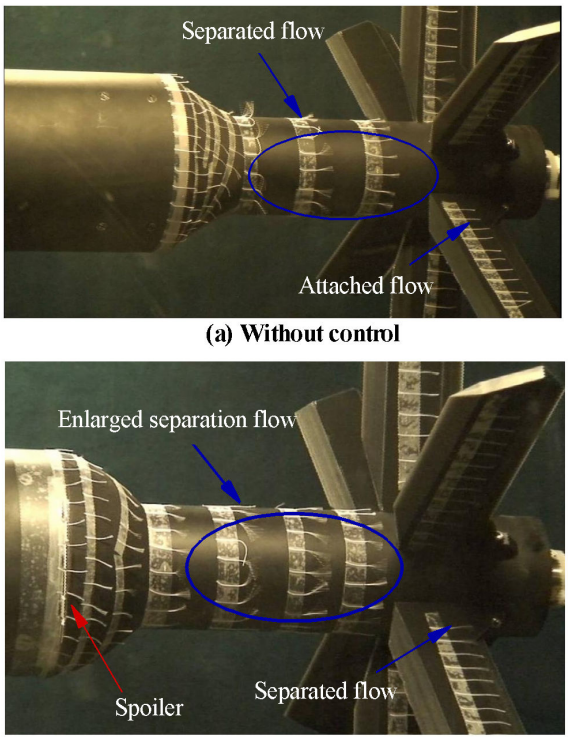

Figure 4-40: Results of Experimental flow visualization using tufts method.

The computational mythologies were described in detail in chapter 3. SST $k-\omega$ was again used to simulate the turbulent flow. Tetrahedral meshes were generated for all configurations. Mesh size of 3,721,345 and 3,909,286 cells were designated for baseline and controlled cases respectively.

Generally, the baseline flow shows a similar behavior at the fore body for both finless and finned configurations. Numerical flow visualization reveals a close-type flow separation induced just downstream of the nose tip for both cases. In addition, the incoming flow remains attached at the projectile shoulder as expected. Spoiler-induced flow separation occurs just upstream of the spoiler, as shown in Figure 4-39 where three streamwise separation vortexes can be see upstream of spoiler. The separation is stronger compared with the finless baseline simulation since the spoiler is higher. The result indicates that upstream flow will be affected by flow-spoiler interaction.

The wake-fin interaction makes the aft body flow far more complex than the finless baseline case. As shown in Figure 4-39, two separation lines and a stagnation point were identified on tail-piece. From the separation lines which are parallel to the wall, the near-wall flow tends to leave the model surface. Part of the near-wall flow between the separation lines flows backwards the spoiler, and rest of the near-wall flow goes towards the fins.

At the aftbody, the flow already separates from the boattail even for the no-control configuration. With control on, the separation zone is enlarged by the spoiler. These flow phenomena were observed in both numerical and experimental flow visualizations. Figure 4-40 shows the experimental results of flow visualization using tufts on the aft body. With control off, the flow is attached before the fins. With control on, however, flow separation is provoked at the tail-fins. The control effect was also predicted by the numerical simulations. As shown in the example in Figure 4-40, the attached flow near the root of fins becomes separated with the spoiler deployed. The behavior was also captured in Figure 4-41 which presents the velocity vectors colored

by velocity magnitude on a cell-wall surface 0.1 mm away from the model surface.

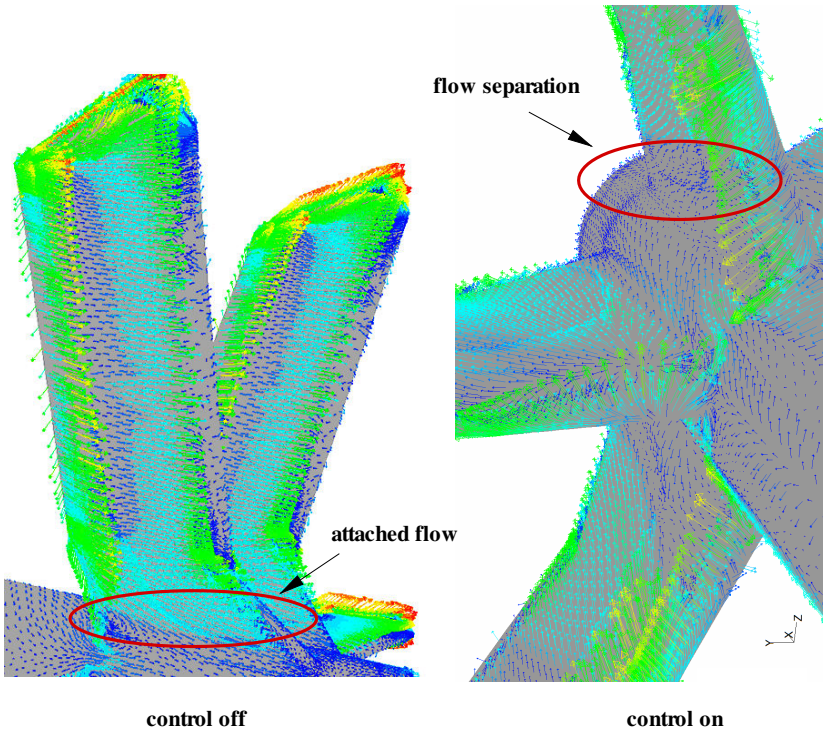

Figure 4-41: Velocity vector display colored by velocity magnitude near the tail-fins on an ISO cell-wall surface.

An interesting feature of the separated flow downstream of the spoiler is the cross-flow velocity component. This flow characteristic can be observed in both numerical and experimental visualizations. In the experimental results in Figure 4-40, the tufts along the side are pointing upward on the lower surface and downward on the upper, which is indicative of the presence of a vortical structure. Similar phenomenon can be seen in the computational results in Figure 4-39.

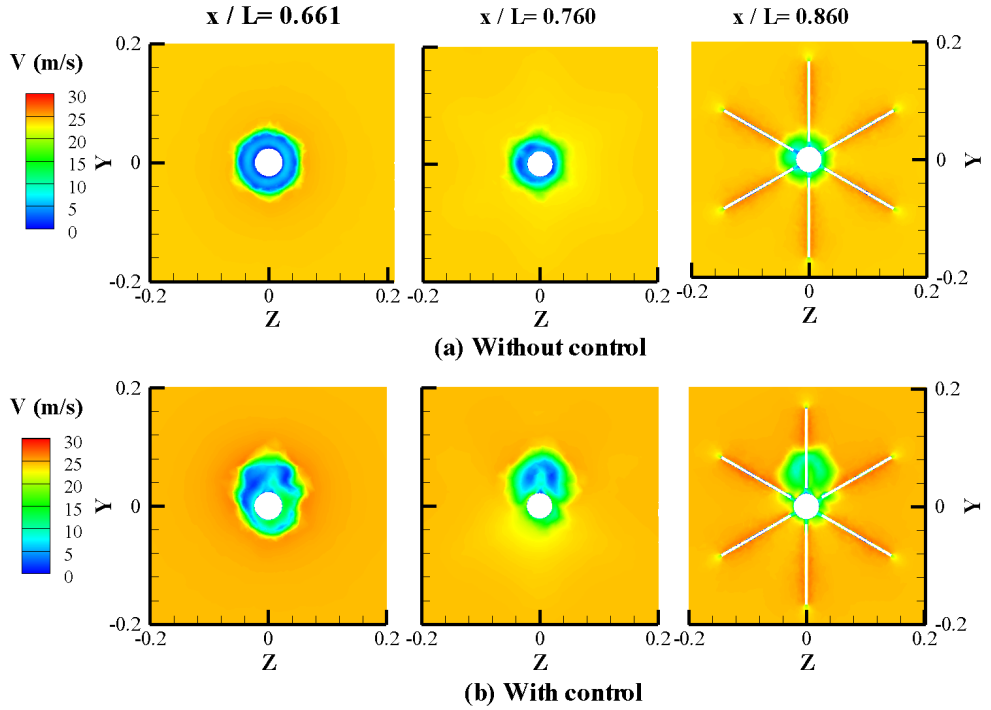

Figure 4-42: Contour of velocity magnitude in cross-stream sections for baseline with and without control.

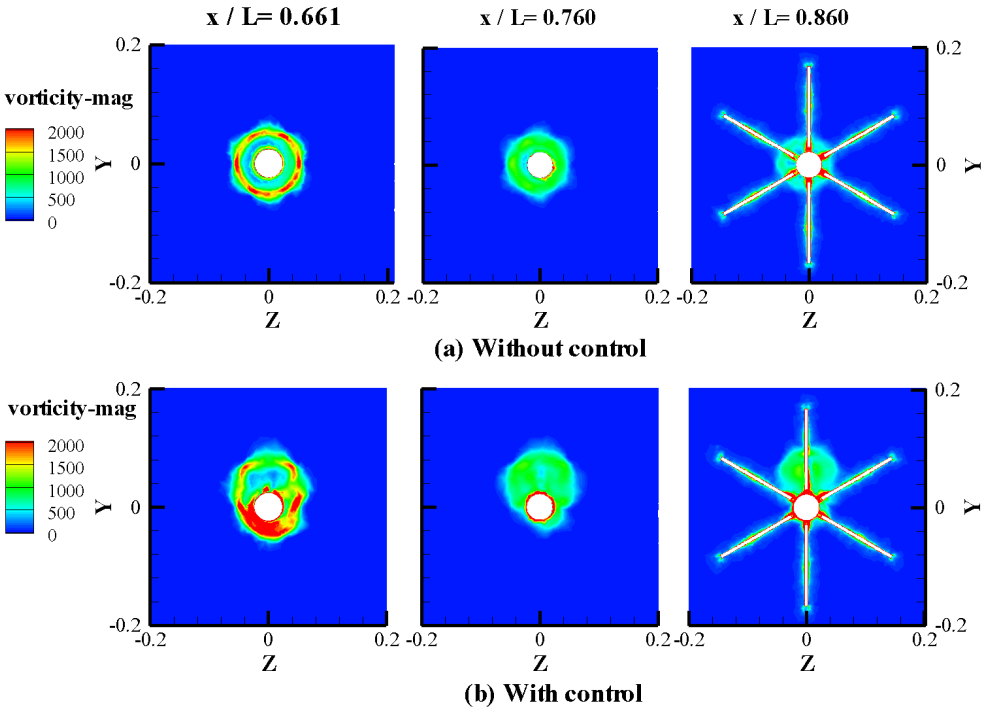

Figure 4-43: Contour of vorticity magnitude in cross-stream sections for baseline with and without control.

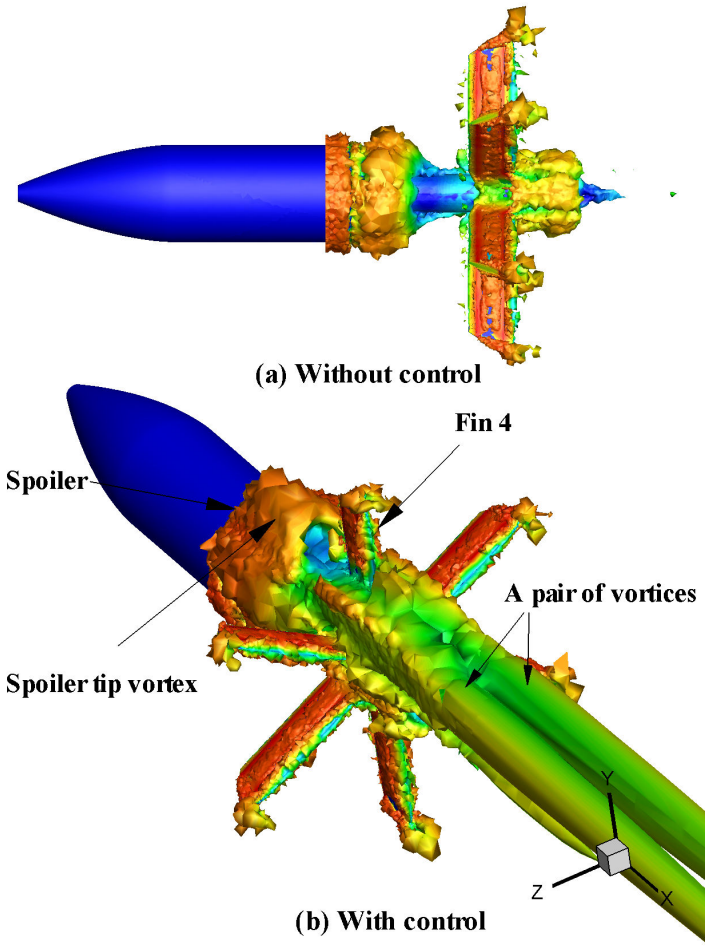

Figure 4-44: Display of vortex structures downstream of spoiler for baseline configurations using an isosurface of Q-criterion (Q=500) colored by velocity magnitude.

This near-wall flow characteristic can be explained by the feature of the wake flow at the upper surface. As discussed previously, a pair of vortices form due to flow-spoiler interaction. At angle of attack of 0°, these symmetric vortices reside above upper surface. The cross-flow velocity and vorticity magnitude-contours of the region from the spoiler to the fins are presented in Figures 4-42 and 4-43 respectively. Three cross-sections in axial direction, representing tip of the tail-piece, middle section of the tail-piece and middle section of the fins, were selected. The vortices change the pressure on the tail-piece. Additionally, the vortex flow extends to the fin area and changes the surface pressure of the fins,shown in Figure 4-44.

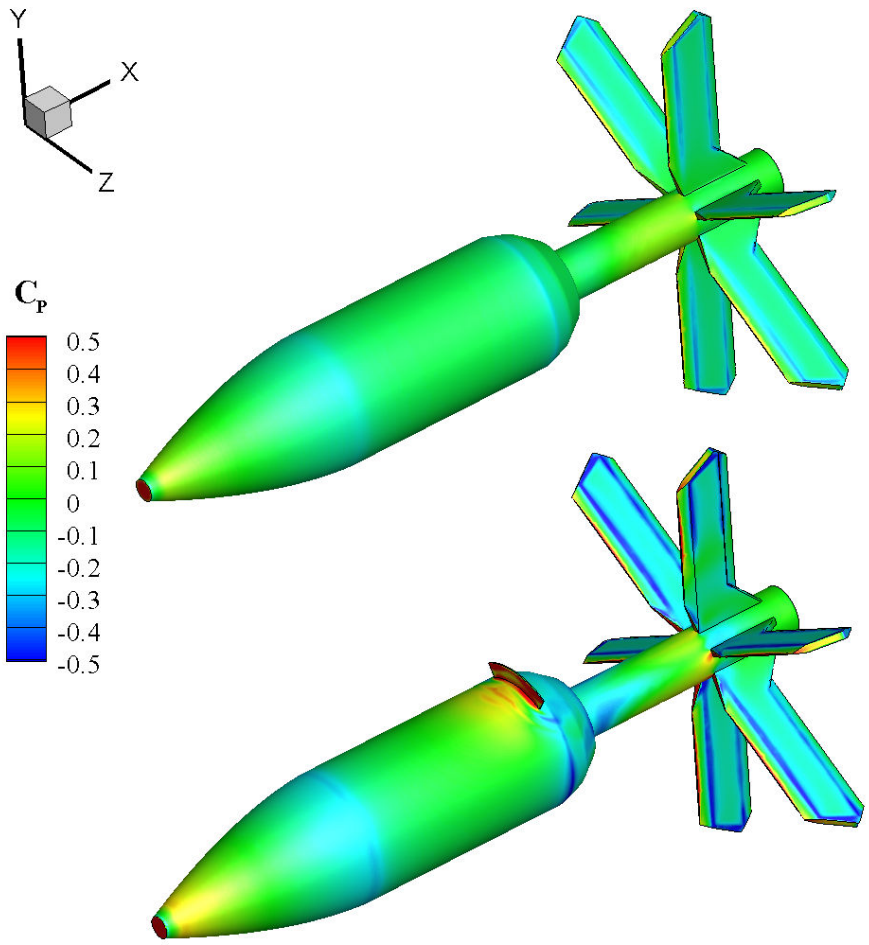

Figure 4-45: Pressure coefficient distribution on model surface for baseline with and without control.

A comparison of pressure distributions on the model with and without control is presented in Figure 4-45. The results show a small, relatively low pressure region immediately downstream from the tip, which corresponds to the nose-induced flow separation. A high pressure region follows indicating flow reattachment. Compared with the baseline, the spoiler induces a higher pressure region upstream and a lower pressure area downstream of the spoiler, which increases the overall pressure drag. Note that pressures on the fins are other parts of the model are also affected. Generally, with a spoiler on top a higher pressure region is produced at the lower surface

compared to the top. The pressure on tail-piece is more complex as a result of the presence of vortices downstream of the spoiler. The vortex wake interacts with fin 4 to produce a low pressure region on the fin.

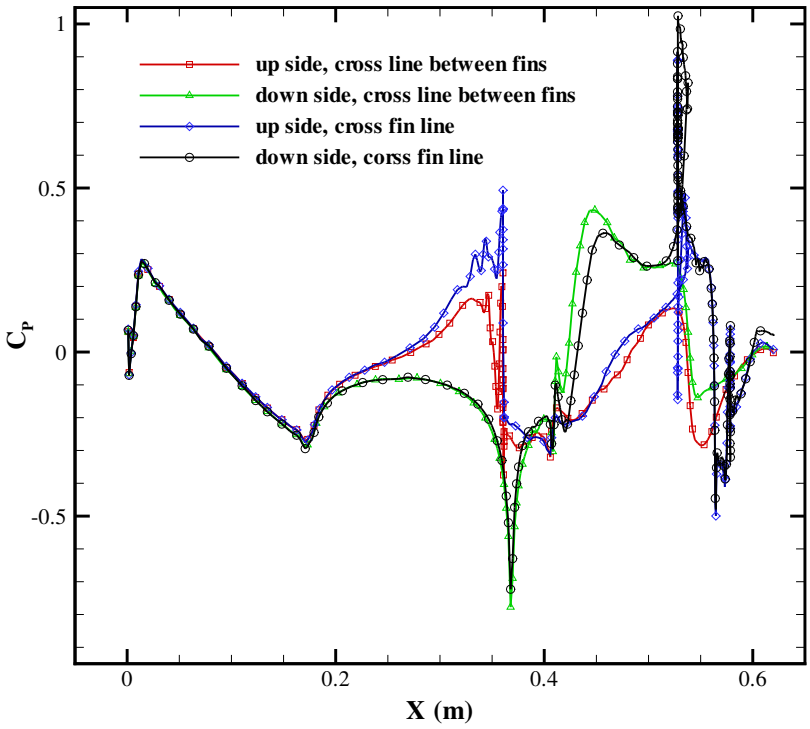

Figure 4-46: Pressure coefficient profiles along axial cross-lines of baseline with control.

Figure 4-46 compares the pressure profiles at different streamwise cross-sections along the model. The "cross fin line" is located on the vertical plane of symmetry aligned with two fins, while the "between fins" is between the vertical and adjacent fins. The results indicate the pressure distribution on nose is axially symmetric. On the main body, pressure at the upper surface is higher than the lower. The lower surface pressure show identical results along the two planes until the tip of tail-piece. On the lower surface of the tail-piece, a positive pressure with magnitude higher than upstream of spoiler can be observed. Based on the pressure distributions, a negative normal force will be generated on main body while a positive normal force will be produced on aft body. With control on, the total normal force of the simulated model

is -0.03. With a center of gravity located at (0.45, 0, 0), the predicted pitching moment is -0.37. Given the physical differences between the computational and experimental models, discussed before, the normal force and pitching moment predictions agree reasonably well with the experimental results which are -0.025 and -0.42 respectively.

4.2.6 Spinning Finned Model with Control

During flight, the STM projectile spins at a rate of 18 rev/s to minimize the adverse effect of mass and configurationally asymmetries. Herein, simulations of spinning model with fins and control were conducted. The results will benefit future 6-DOF simulations and optimization of the control.

The computational method used is 3D unsteady RANS, often denoted URANS. In URANS, the dependent variables in governing equations are not only a function of the space coordinates but also a function of time. To enhance the accuracy, a sliding mesh approach in FLUENT is employed to capture transient behaviors of the flow. The computational domain was split into two, one of which is stationary and the other rotating. A pair of interface zones with conformal grids is generated to transfer the solution information between the separated domains. Detailed computational mythologies were described in chapter 3. The SST $k-\omega$ solving transitional flows, compressibility effects and viscous heating was again used to simulate the turbulent flow. The discretization scheme of second-order upwind for the convective terms was used together with fully implicit second-order discretization in time; this gives second-order accuracy in both space and time. The time step size was calculated based on the experimental Strouhal number, which is about 0.2 corresponding to a Reynolds number of 1.75×10^5. Based on simulation performance the time step size was corrected and the final value is 0.0004s, which resulted in 500 time steps for every revolution.

The configuration with control is simulated at a clockwise (munition front view, Figure 4-26) spin rate of 5 rev/s. A spoiler 12.7 mm in height and 60° in arc-length

is placed on the top (180°) of boattail for pitch control. The effect of angle of attack was not investigated in this study, and the results presented herein were obtained at angle of attack of 0°.

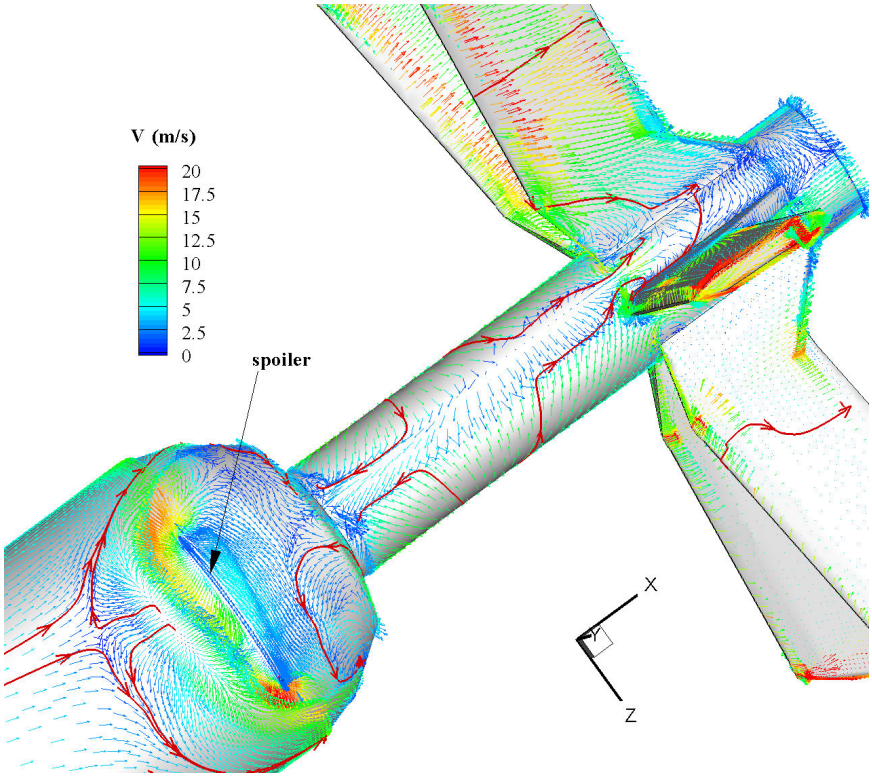

Figure 4-47: Velocity vector display upstream and downstream of the spoiler on an ISO cell-wall surface for the spinning projectile with control on.

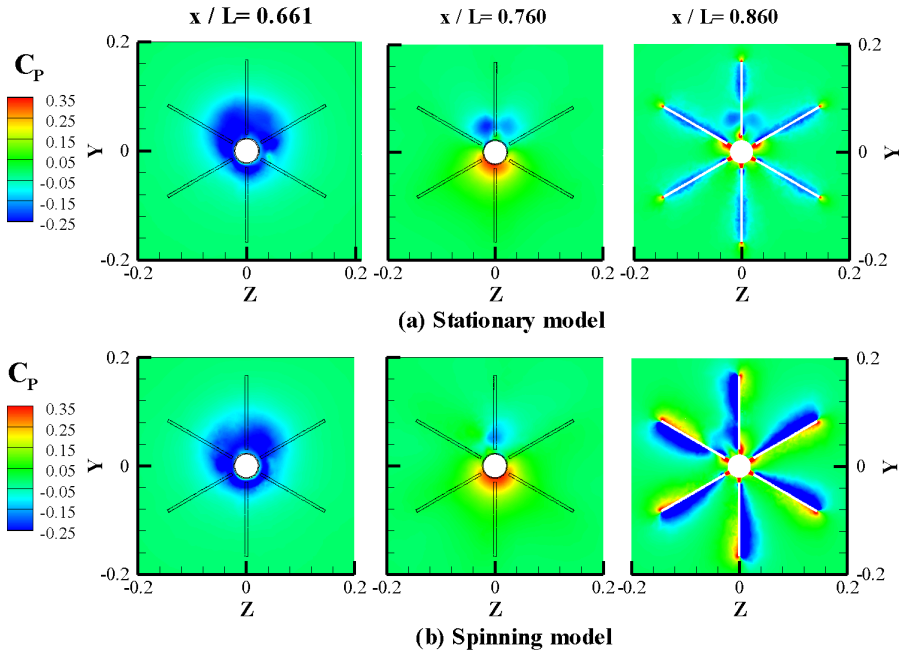

Figure 4-48: Contour of pressure coefficient in cross-stream sections for stationary and spinning projectiles with control.

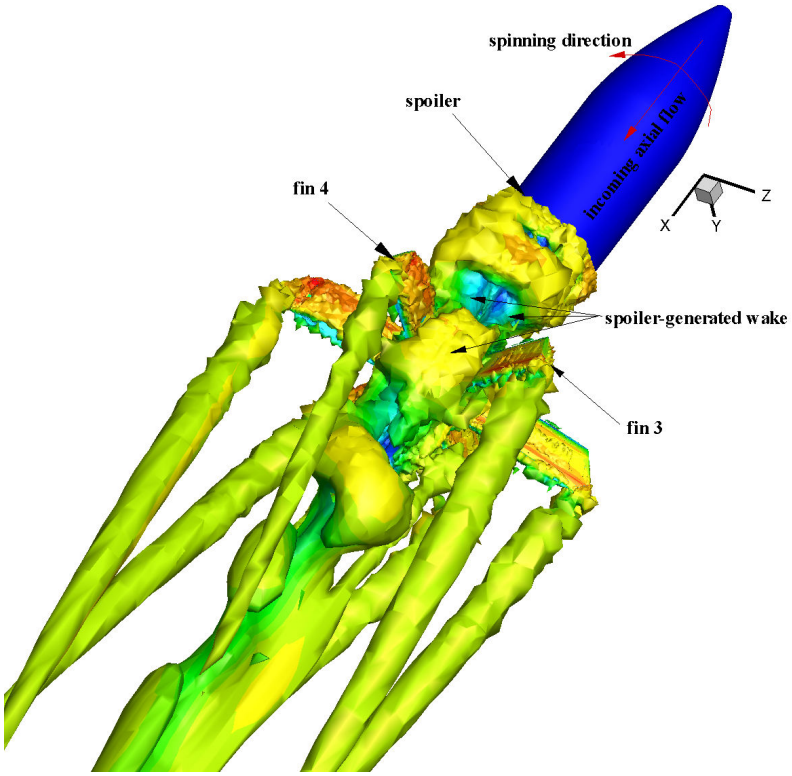

Figure 4-49: Visualization of vortical flow downstream of spoiler for spinning baseline using an isosurface of Q-criterion (Q=500) colored by velocity magnitude.

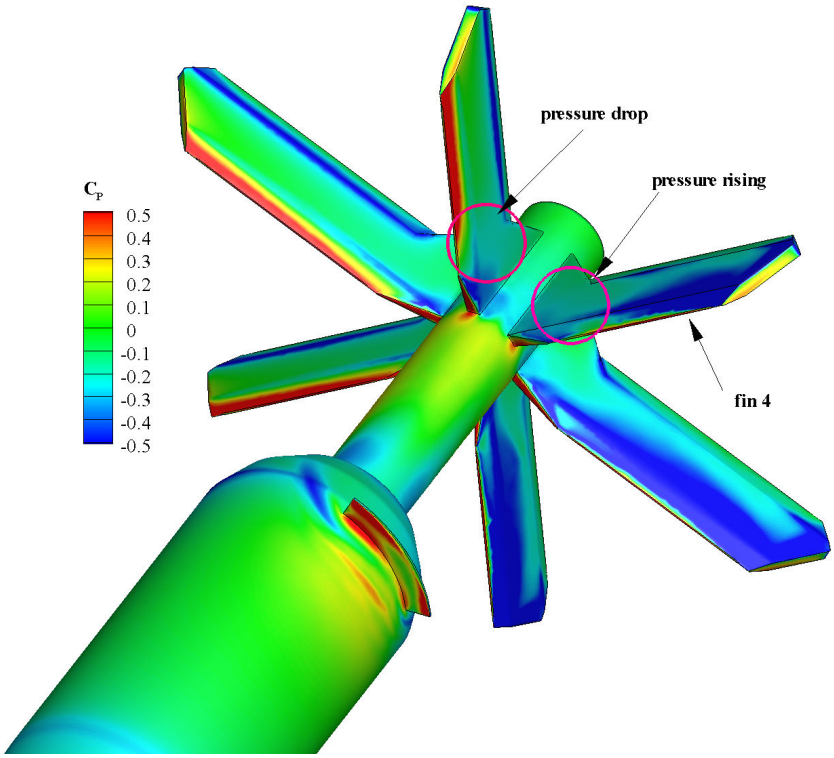

Figure 4-50: Contour of pressure coefficient on model surface for spinning projectile with control.

Figure 4-47 displays the velocity vectors colored by the velocity magnitude on a cell-wall surface. The surface is only 0.1 mm away from the model surface, which ensures the flow in the boundary layer is illustrated. The result presented is at the roll angle of 360°. Due to the spin, the incoming flow interacting with the spoiler has a cross-stream component. As such, the wake flow is not symmetry along the z plane. Additionally, the separation behavior on the tail-piece is changed with the separation lines shifted backwards the direction of spinning. The numerical flow visualization reveals that the flow is modified from the near-wall region. Cross-stream pressure coefficient contours of the region from the spoiler to the fins are presented in Figure 4-48. The results show that the spoiler-induced vortices become asymmetric, and the intensities of the vortices are also altered. With the spinning motion, the vortex wake is shifted to the space between fins 3 fin 4,shown in Figure 4-49. The vortices alter the pressures on the fins. As shown in Figure 4-50, pressure drops and rises near the

roots of fin 3 and fin 4.

Figures 4-51 and 4-52 show the time histories of pitching moment coefficient and drag force coefficient during spin. The X-axis is the spinning angle, calculated based on the spinning rate and time. Generally, the pitching moment generated by the spoiler is a sine function of rolling angle. Data analysis indicates that the force on spoiler itself has a great contribution to the total pitching moment. At 0° angle of attack, the forebody flow and associated pressure distribution are identical at varying rolling angles. During spinning, the total moment coefficient has two components. One is the pitching moment and the other the yawing moment, with their magnitudes varying as sine and cosine functions of the spinning angle. In addition, a high-frequency oscillation can be seen to impose on the pitching moment coefficient in Figure 4-51 and the drag coefficient in Figure 4-52. The oscillations are caused by the fluctuations of surface pressure induced by unsteadiness in the flow. These computed results clearly indicate the unsteady nature of the wake flow field. As discussed previously, an asymmetric vortex wake is produced due to spin and the vortices are unsteady. As a result, oscillatory drag and pitching moment are produced.

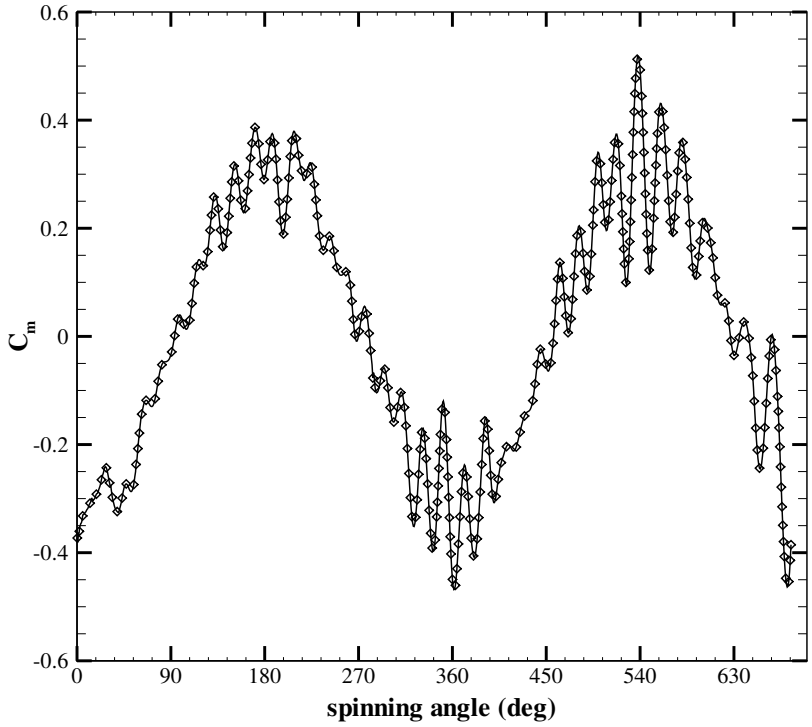

Figure 4-51: History profile of pitching moment coefficient of controlled baseline during spinning.

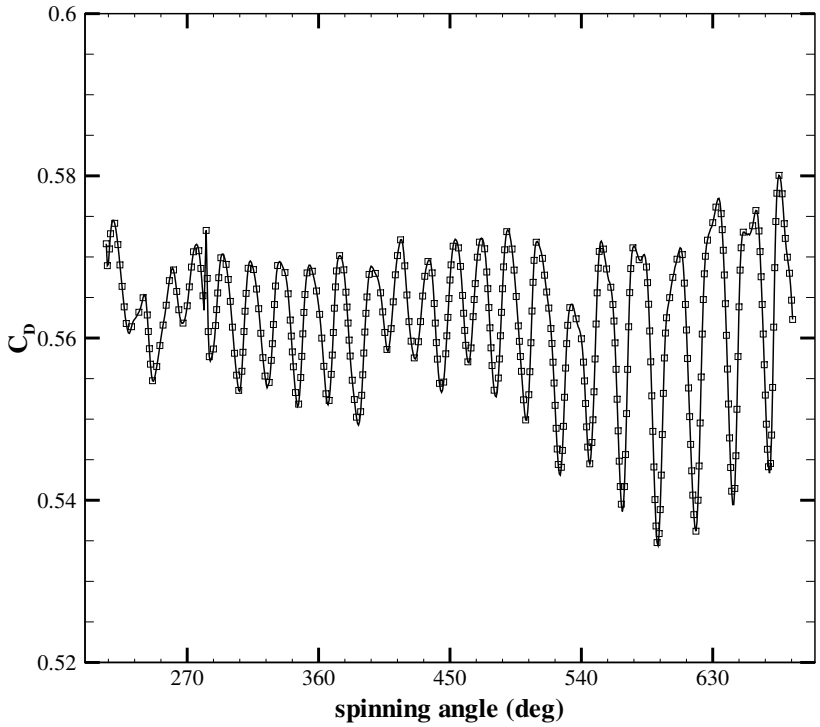

Figure 4-52: History profile of drag force coefficient of controlled baseline during spinning.

Chapter 5

Supersonic Investigation

5.1 Grid Independence Study

Coordinates used in the numerical result discussions are shown in Figure 4-26. Grid independence study was performed on the no-control configuration. Coarse and fine meshes were generated. The coarse mesh has 3,028,386 cells and the fine mesh has 5,969,040 cells. Figure 5-1 compares the Mach number profiles in the wake region, and Figure 5-2 compares the pressure distributions on the model. Lines 1 and 2 in Figure 5-1 are on the y = 0 axes on the cross-planes at x/L of 1.05 and 1.125 respectively.

Figure 5-1 shows Mach number profiles predicted using both grids are essential and as expected symmetric in the z-direction due to configuration symmetry. The profiles match each other well at mostly locations. Small deviations can be found in the portion of the wake coming from middle of the fins. These wakes is farther from the model surface compared with others, which indicates the grids may have caused discretization errors at farfield. The pressure coefficient distributions on the model based on the two grids are compared in Figure 5-2. The results show that the predicted pressures agree with each other very well both on the body and on the fins. This indicates the coarse mesh is sufficient for predicting near-wall flows and associated pressures. As such, all the results reported herein are obtained using grid

levels of 3 million cells for the baseline, and about 3.5 million cells for cases with control.

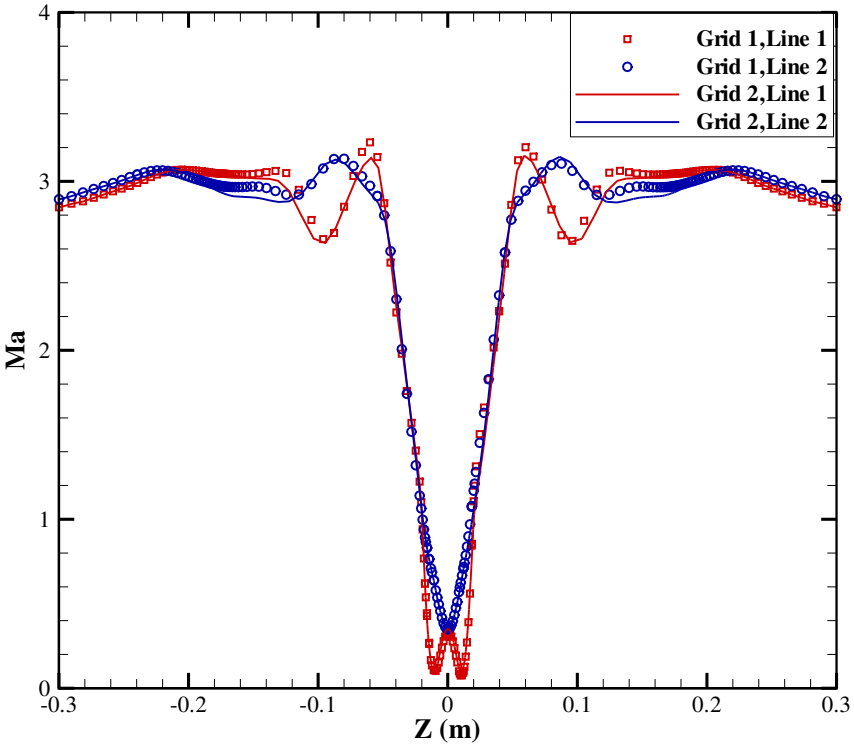

Figure 5-1: Comparisons of velocity profiles of cross lines on Y plane of symmetry predicted by coarse and fine meshes.

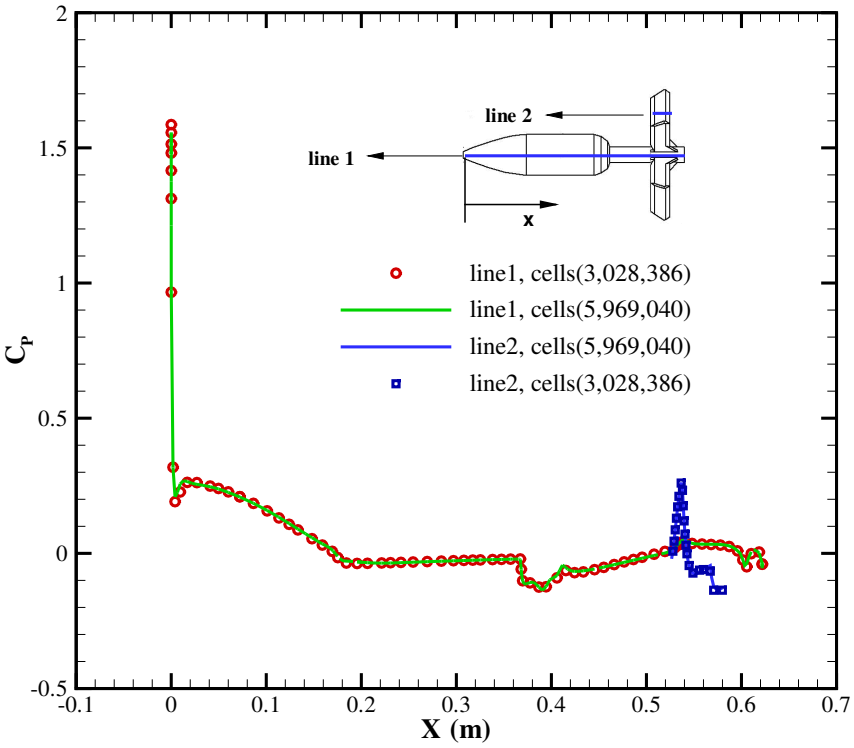

Figure 5-2: Comparisons of pressure distributions on model surface predicted by coarse and fine meshes.

5.2 Turbulence modeling

Detailed computational mythologies were described in chapter 3. As pointed out in the literature review, SST $k-\omega$ and Spalart-Allmaras turbulence models are the most popular models in aerodynamic simulations using RANS. In the present supersonic simulations, steady 3D RNAS simulations coupled with SST $k-\omega$ turbulence model were conducted to access the control effectiveness at supersonic speeds.

To verify the turbulence model, computational results using SST $k-\omega$ and SA turbulence models were compared. Figure 5-3 shows the pressure profiles along specific axial lines predicted using these two models. Small pressure deviations were observed just downstream of the projectile tip where the close-type separation occurred. Apart from this, the predicted pressures agree very well at the other locations. This compar-

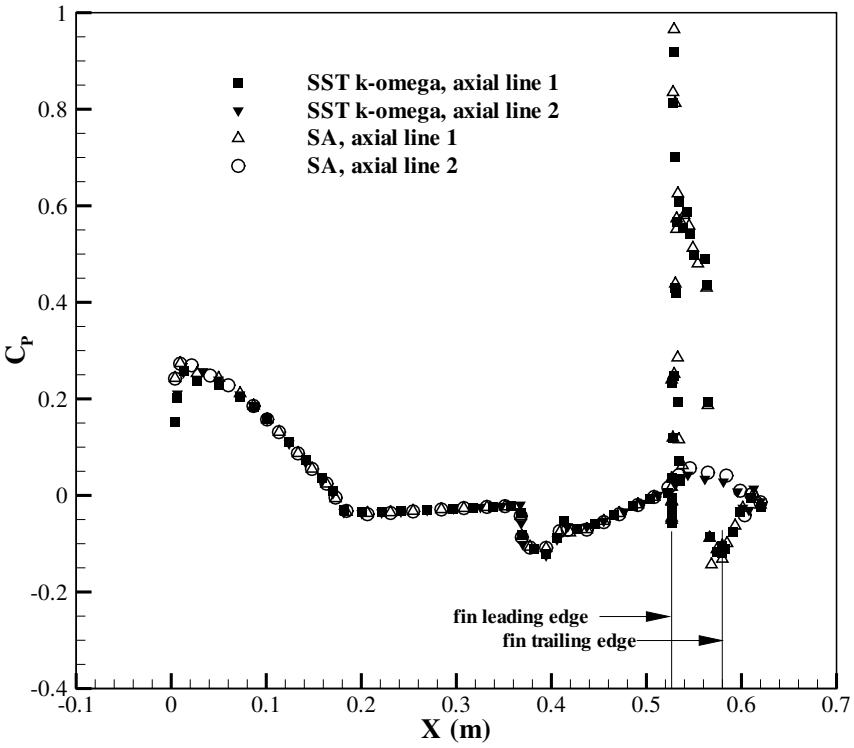

Figure 5-3: Comparisons of pressure distributions on model surface predicted using SST and SA turbulence model.

ison indicates that the simulations are independent of the specific turbulence model used.

5.3 Proof of Concept at Supersonic Speeds

The Wake-Fin Tailoring method has been shown in Chapter 4 to be effective in generating control forces for the STM model at subsonic speeds. In this chapter, simulations at a Mach number of 3 were conducted to validate the control effectiveness at supersonic speeds. This speed is the operational flight speed of the Army's 120mm Line-of-Sight Multi-Purpose (LOS-MP) munitions.

As before, a spoiler 10.16 mm in height and 60° in arc-length is placed on top of the main body (180°) just upstream the boattail. Figure 5-4 shows the Mach number contours near the model for control off and control on cases. For both cases, a bow

shock is generated just ahead of the tip of the blunt nose. The freestream flow is compressed and the speed of the flow is decreased to about Mach 2.5 near the nose. At the shoulder, there is a weak expansion fan and the speed of the flow is increased to about 3.0. For the model geometry, the main body and boattail form a convex corner with a large turn angle. As such, a strong expansion fan is produced and the flow is accelerated up to a Mach number of 3.5. Flow analyses around the fins reveal the generation of shocks and expansion fans, results of which will be discussed later.

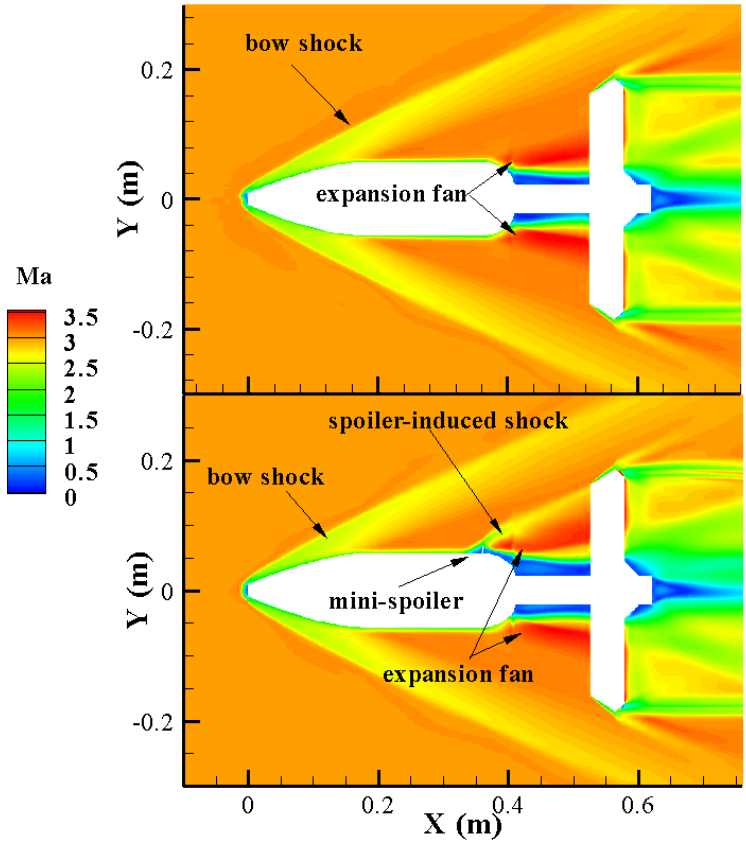

Figure 5-4: Contours of Mach number for baseline and controlled baseline.

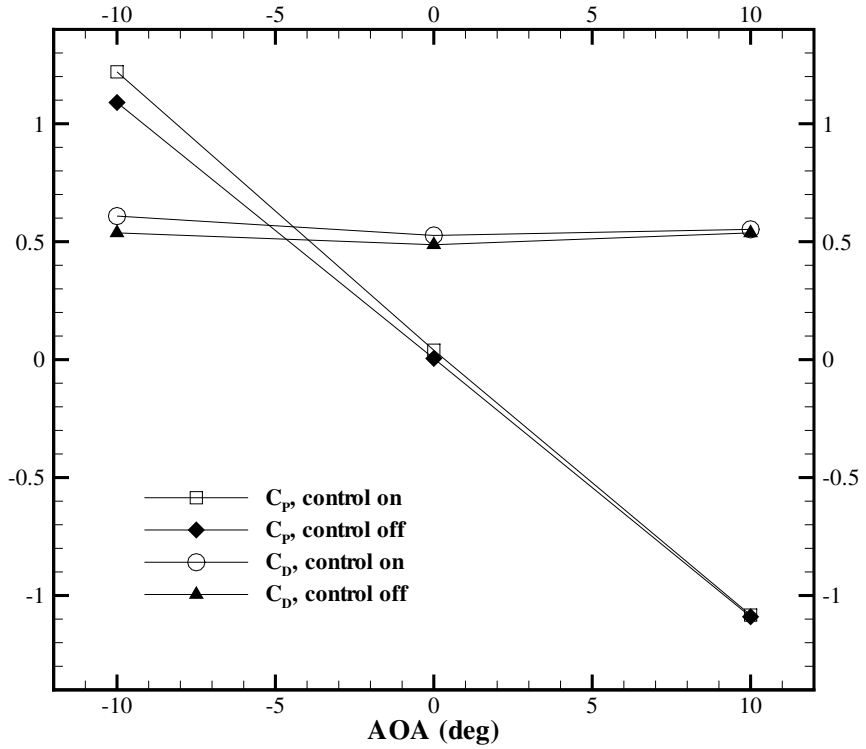

Figure 5-5: Comparisons of pitching moment and drag coefficient of baseline with and without control.

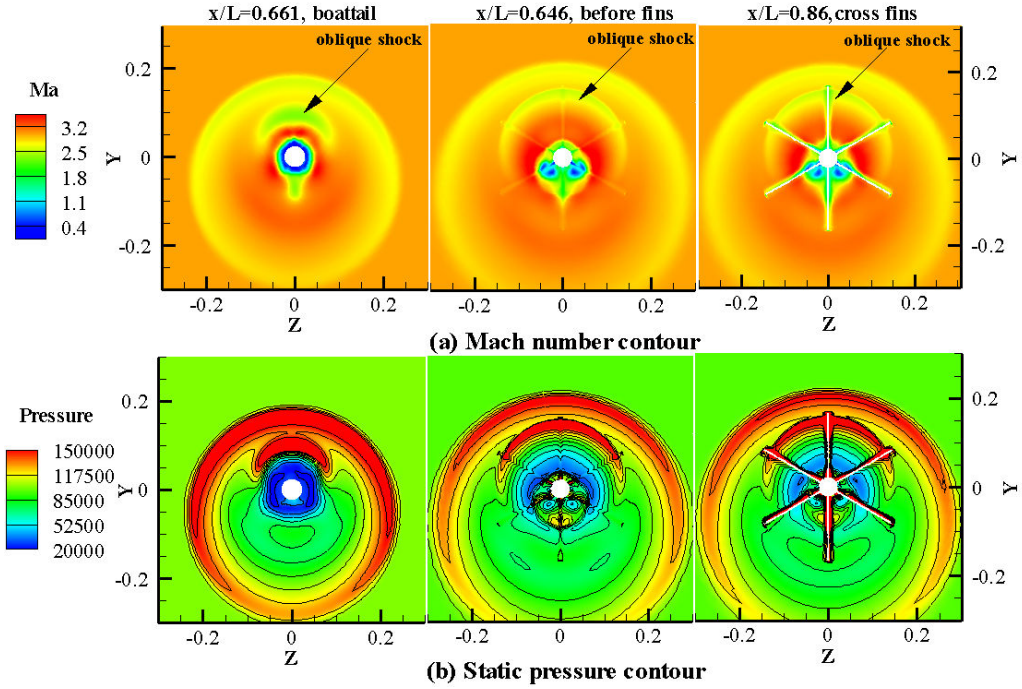

Figure 5-6: Contour of Mach number and pressure in cross-stream sections for controlled baseline.

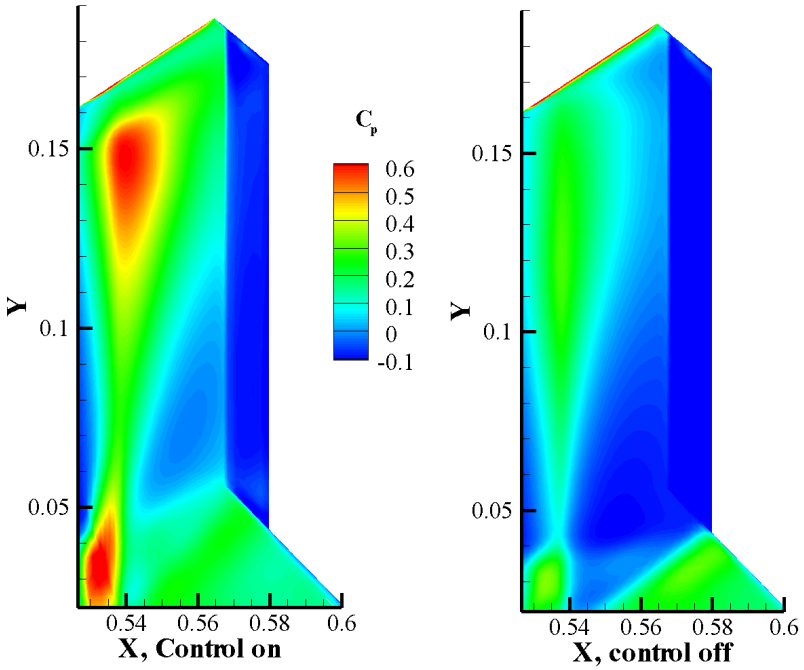

Figure 5-7: Contours of pressure coefficient on fin 4 (see Figure 4.25).

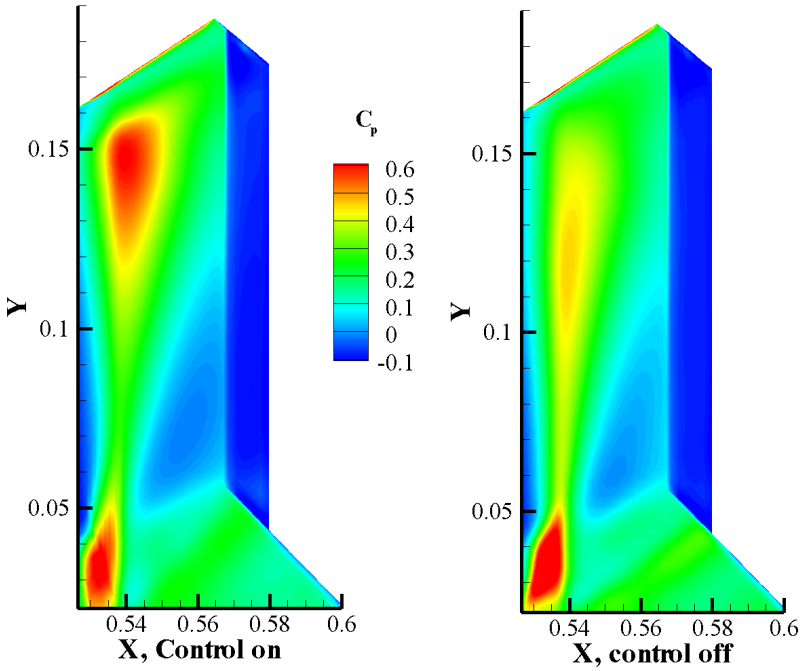

Figure 5-8: Contours of pressure coefficient on left side surface of fin 3 (see Figure 4.25).

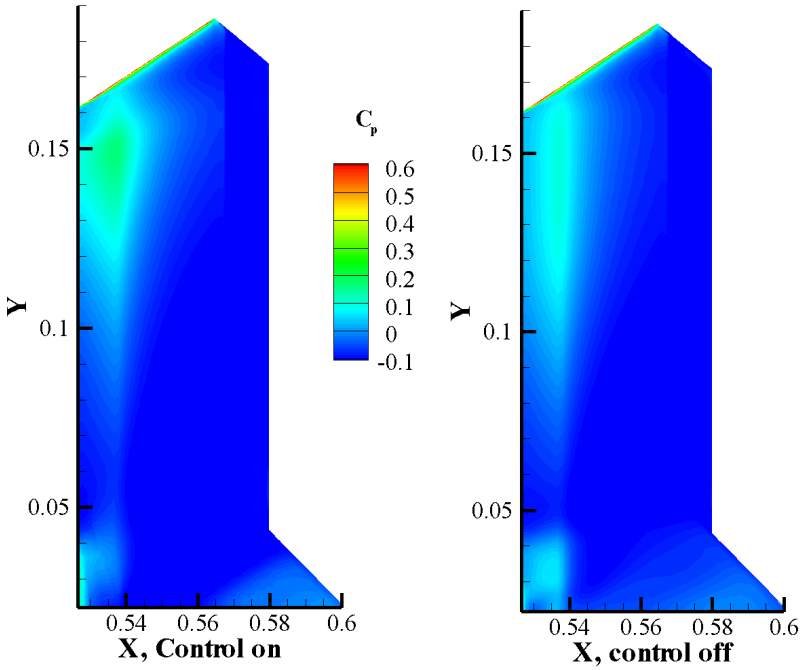

Figure 5-9: Contours of pressure coefficient on right side surface of fin 3 (see Figure 4.25).

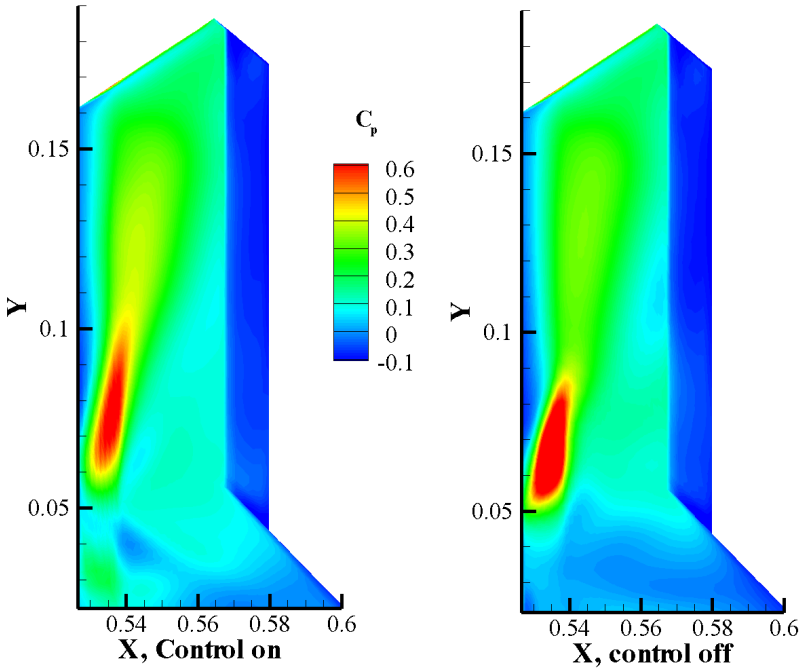

Figure 5-10: Contours of pressure coefficient on left side surface of fin 2 (see Figure 4.25).

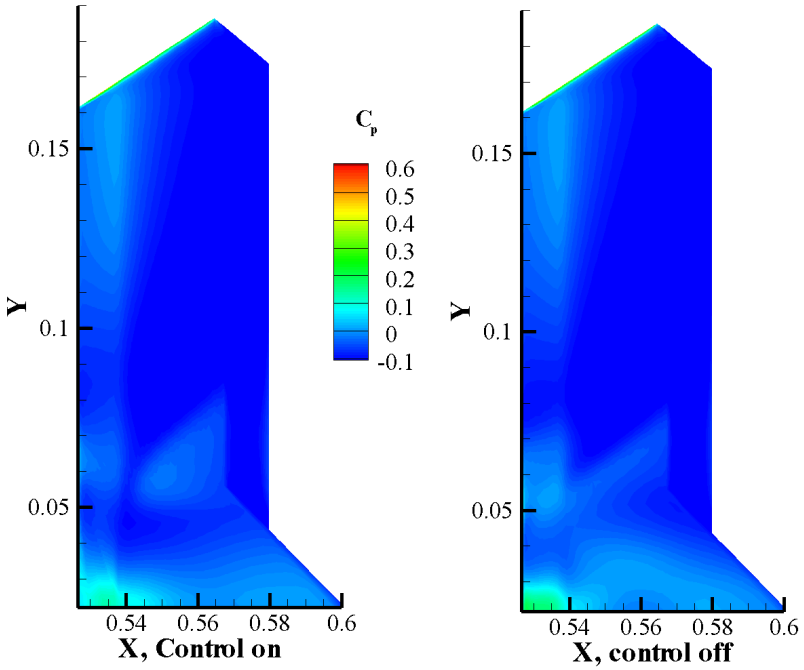

Figure 5-11: Contours of pressure coefficient on right side surface of fin 2 (see Figure 4.25).

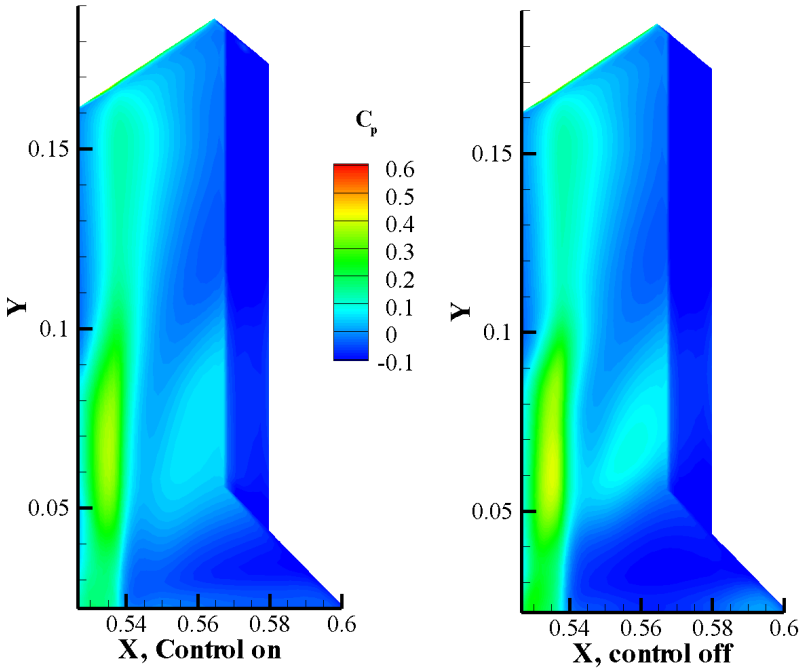

Figure 5-12: Contours of pressure coefficient on fin 1 (see Figure 4.25).

When the control is on, the supersonic flow past the spoiler is compressed and a spoiler-induced oblique shock, as designed, is produced just ahead of the spoiler and propagates to the downstream fins as shown in Figure 5-4. Additional results indicate the shock propagation direction is determined by the angle-of-attack and the height of the spoiler at a given free stream Mach number. Compared with the no-control case, the spoiler strengthens the downstream expansion fan moves the expansion fan forward. As a result, the spoiler generates an asymmetric wake that becomes the upstream flow for the fins. Generally, the asymmetrical flow includes the shock, low-speed region near the tail-piece, and high-speed region (expansion fan) between them. The pressure near the top of fins is influenced by the shock, while the pressure at the tail surface and the bottom of fins is affected by the wake of the boattail flow separation which is selectively enlarged by the usage of spoilers.

Additional simulations were conducted at angles of attack of -10° and 10°. The computed results of pitching moment and drag coefficient are presented in Figure 5-5. Once control is on, projectile drag is slightly increased at all tested angles of attack. The most effective control effect is obtained at -10°, with the pitching moment coefficient increases by about 11%. Cross-stream Mach number and static pressure contours of the region from the spoiler to the fins are presented in Figure 5-6 (a) and 5-6 (b) respectively for the angle-of-attack of -10°. The results indicate the asymmetric flow induced by the spoiler is transferred to the fins area and changes the surface pressure of the fins. With an arc shape, the spoiler-induced oblique shock spreads out and interacts with multi-fins and modifies the pressure on the fins. Moreover, the expansion fan strengthened by the spoiler at upside and affects the pressure on the fins in the same manner as the shock.

Comparisons of pressure coefficient distributions on the fins with control off and on are presented in Figures 5-7 to 5-12. Fin numbering is the same as presented in Figure 4-26. Because of symmetry, only the surface pressure distributions on one side are presented for fins 1 and 4. Additionally, results for fins 5 and 6 are similar to

fins 2 and fin 3 respectively due to symmetry. As shown in Figure 5.5, due to the impingement of the shock, a comparatively high pressure region (x = 0.54, y = 0.15) at the top of the fin 4 is produced when control is on. Furthermore, a high pressure region centered about around x = 0.53 and y = 0.025 near the root of the fin 4 is generated. This is caused by the modified subsonic wake of the boattail over the tail-piece. Similar pressure modifications are seen on fin 3. A high pressure region (centered around x = 0.54, y = 0.15) can be seen at the top of the fin 3. On the left (up) side of fin 3, the pressure coefficient increases from 0.4 to 0.6. On the right (down) side of fin 3, the pressure coefficient increases from 0.0 to 0.1. The locations of high pressure are almost identical for fins 3 and 4, which is due to the spoiler-induced shock propagating in the shape of an arc. In contrast to fins 3 and 4, no such modified pressure region can be seen on fins 1 and 2. This is because the shock only directly interacts with fins 3, 4 and 5 as shown in Figure 5-4 (x/L= 0.86).

Because of symmetry, there is no rolling moment generated in this control case. The analysis nevertheless suggests that roll control can be generated by interactions between asymmetric wake and fins since the controllable spoiler-induced shock can directly change the pressure on fin surfaces. The sizes and locations of the spoilers however will need to be very carefully arranged since the asymmetric wake can interact with both sides of the fin as well as multiple fins.

Additional to the asymmetrical wake affecting the pressure on the fins, but the flow-spoiler interaction modifies the local pressure on the projectile body. Figures 5-13 and 5-14 compare the pressure profiles on the axial cross lines for control-off (black lines) and control-on cases. In all cases, a near-constant pressure is observed on the main body. Additionally, sharp pressure drop occurs on the first stage of boattail due to flow separation. In general, the flow-spoiler interaction produces an oblique shock ahead of the spoiler leading to flow separation. Consequently, a significant high pressure rise is followed by a sharp drop at the back side of spoiler. Farther downstream from the spoiler, the pressure variation is fairly gradual. At 0° of angle

of attack, the upper surface pressure of the boattail is changed slightly when control is on. No obvious pressure change however occurs at lower surface.

Figures 5-13 and 5-14 show that the angle of attack has a great effect on the control performance. When the angle of attack is increased from zero, the windward boundary layer on the model becomes thinner. This thinner boundary layer and the clean impingement of the external flow bring higher windward side pressures and stronger flow-spoiler interactions. On the leeward side, the effect is opposite producing relatively lower leeward side pressure and weaker flow-spoiler interactions. In supersonic flow, it is not possible for a pressure disturbance to travel upstream if no solid bodies are presented. That is, the influence a perturbation is carried downstream. The same principle is applicable to the spoiler-induced wake. The turbulent wake will not affect forebody pressure, but it may change the pressure on the aftbody. The computational results show the influence depends on the cross-flow component in the induced wake. For example, large pressure modifications at the aft body are obtained at -10° of angle of attack due to the enlarged flow separation at the aft body.

Based on the air flow and pressure results, contributions to the control force come from three main sources. They are (1) direct fluid-spoiler interaction, (2) wake-fin interaction, and (3) the wake near the tail induced by the actuator. It was found that with the spoilers the boattail wake near the fins is enlarged and skewed, so the pressure on the tail and the roots of the fins are changed. Additionally, pressure loadings on the fins are modified by the oblique shock induced by the spoilers. The unbalanced pressure on the fins can be used to produce the desired control if the spoilers are strategically arranged.

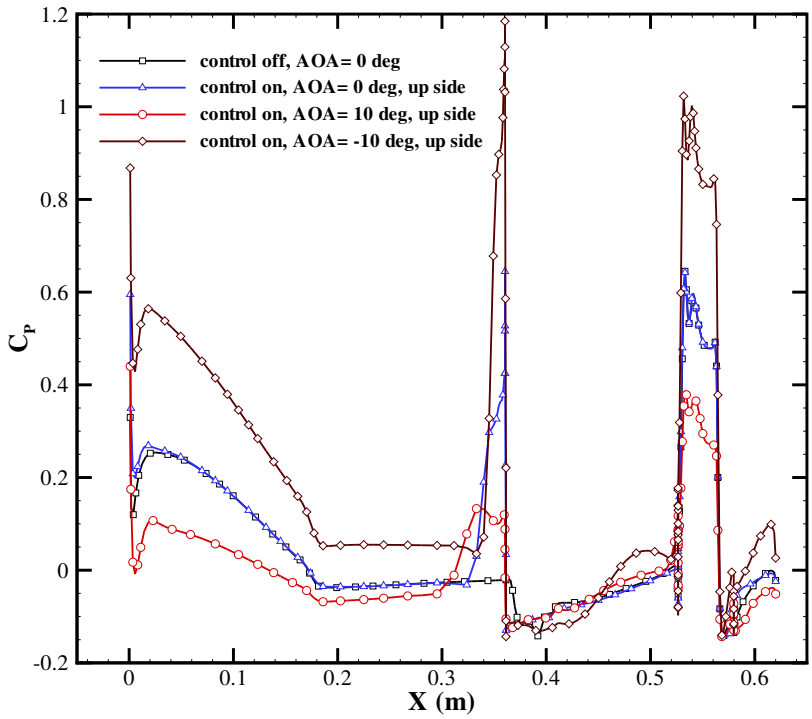

Figure 5-13: Effect of angle of attack on pressure coefficient on upside surface.

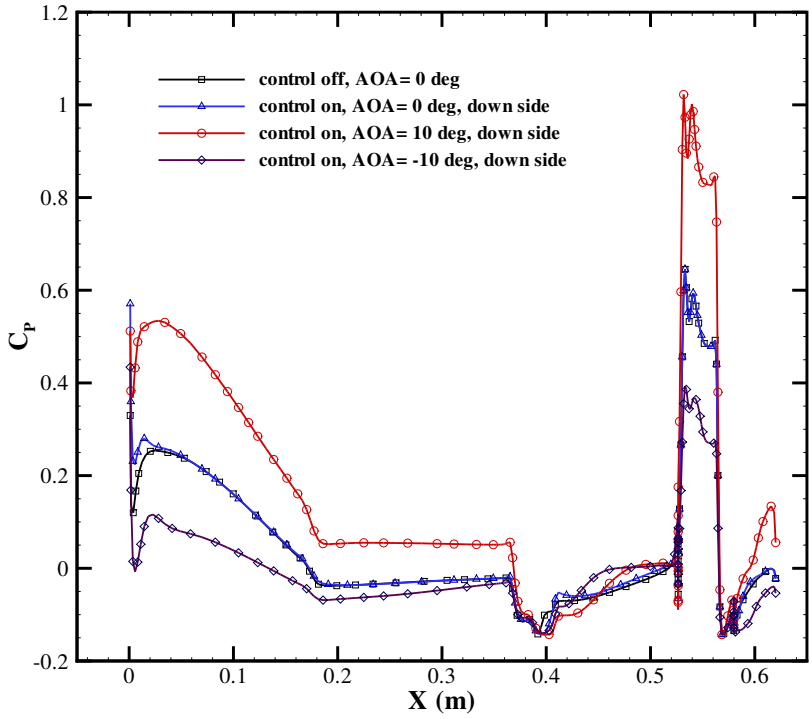

Figure 5-14: Effect of angle of attack on pressure coefficient on downside surface.

5.4 Configuration Study

To further investigate the effects of control on drag force, pitching moment, rolling moment and yawing moment, additional simulations at Mach 3 were conducted for the configurations illustrated in Figure 5-15. The results are summarized in Tables 5.1 and 5.2.

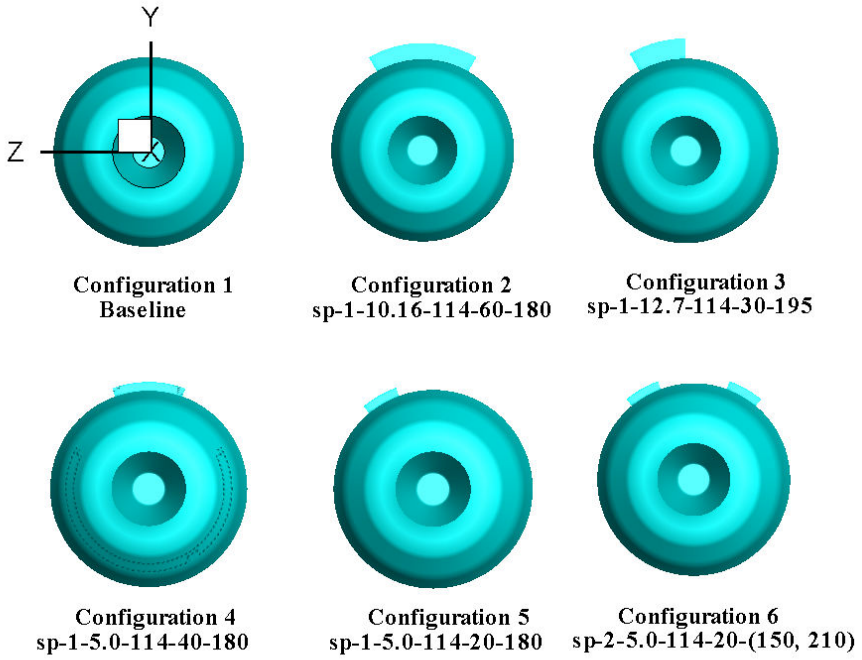

Figure 5-15: Illustrations of configurations studied at supersonic speed (back view).

The results in Table 5.1 show the drag force increases with the angle of attack and spoiler deployment. The maximum drag force occurs on configuration 2 at $-10°$ angle of attack. With the control, the drag is increased from the baseline value of about 0.54 to 0.61. Due to the compressibility effect at supersonic conditions, the control authority is not as significant as at subsonic speeds. At the same time, the penalty of drag increment is much reduced compared with the subsonic case.

Configurations 2 and 3 are both effective in generating pitching moments for control. The most significant control magnitude is achieved with configuration 2,

where a spoiler with a height of 10.16 mm and arc-length of 60° is deployed at the most effective position (180°) based on the subsonic wind tunnel study. In contrast to configuration 2, configuration 3 is not y-plane symmetric. The results indicate this asymmetric spoiler deployment can generate rolling moments at all angles of attack. For example, the rolling moment coefficient (Cl) on configuration 3 is raised from -0.0008 (should be zero in theory) with no control to -0.0026 with control at $-10°$ angle of attack.

Table 5.1: Computational results of configuration 1 to configuration 3.

		$-10°$	$0°$	$10°$
Config.1	Cd	5.37E-01	4.90E-01	5.37E-01
	CI	-8.14E-04	-3.78E-04	-8.14E-04
	Cn	2.79E-03	6.37E-03	-2.79E-03
	Cm	1.09E+00	-2.60E-03	-1.09E+00
Config.2	Cd	6.09E-01	5.28E-01	5.52E-01
	CI	1.92E-04	-1.25E-04	-3.41E-04
	Cn	4.01E-04	-7.18E-03	-5.56E-03
	Cm	1.21E+00	4.21E-02	-1.08E+00
Config.3	Cd	5.83E-01	5.15E-01	5.51E-01
	CI	-2.60E-03	-1.29E-04	-1.35E-03
	Cn	-8.98E-03	-8.36E-03	1.80E-02
	Cm	1.15E+00	2.12E-02	-1.09E+00

Results similar to Table 5.1 are observed in Table 5.2 where configuration 5 is asymmetric with respect to y-plane (y=0). Significant rolling moments are produced with the control. Table 5.2 shows results of control using small-size spoilers at relatively low angles of attack. As can be seen in Table 5.2, the drag still increases with the angle of attack and by the deployment of the spoiler. Additionally, nose-up pitching moments are produced at negative angles of attack on configurations 4 to 6. An interesting observation can be made on configuration 4 where the area of the spoiler

is larger than configuration 5 and the same as configuration 6 (see Figure 5-15).

Table 5.2: Computational results of configuration 4 to configuration 6.

		$-5°$	$-2.5°$	$0°$	$2.5°$	$5°$
Config.1	Cd	5.14E-01	5.01E-01	4.89E-01	5.01E-01	5.14E-01
	CI	5.00E-04	-9.25E-05	3.87E-06	-9.25E-05	5.00E-04
	Cn	9.24E-05	2.67E-03	1.78E-02	2.67E-03	9.24E-05
	Cm	5.13E-01	2.52E-01	7.75E-03	-2.52E-01	-5.13E-01
Config.4	Cd	5.30E-01	5.12E-01	5.03E-01	5.06E-01	5.11E-01
	CI	-3.23E-04	8.91E-04	2.10E-04	-1.31E-03	5.82E-04
	Cn	-6.27E-04	-7.48E-03	7.00E-03	-4.68E-03	1.23E-03
	Cm	5.18E-01	2.53E-01	-3.68E-03	-2.50E-01	-5.24E-01
Config.5	Cd	5.22E-01	5.06E-01	4.96E-01	5.03E-01	5.13E-01
	CI	-2.44E-03	-1.05E-03	-1.46E-05	7.04E-04	1.80E-03
	Cn	-4.29E-03	-2.27E-03	-9.46E-03	1.87E-02	1.47E-02
	Cm	5.35E-01	2.43E-01	1.13E-02	-2.41E-01	-5.31E-01
Config.6	Cd	5.55E-01	5.27E-01	5.03E-01	5.11E-01	5.17E-01
	CI	5.61E-04	2.04E-04	5.88E-04	3.17E-04	-2.84E-04
	Cn	-7.95E-03	-3.46E-03	1.40E-02	4.52E-04	-9.37E-04
	Cm	6.06E-01	2.85E-01	-6.78E-03	-2.38E-01	-5.20E-01

At $-5°$ angle of attack, the results show smaller spoiler-induced pitching moment on configuration 4 compared with configurations 5 and 6. This indicates the most effective azimuth location detected in subsonic study may be the same for supersonic speeds. As discussed in the previous section, besides the height and length of the spoiler, and the azimuth location directly affects shock generation and its propagation. As a result, the controlled-shock modifies the surface pressure on specific regions of the fins.This indicates the most effective azimuth location detected in subsonic study may be the different for supersonic speeds. As discussed in the previous section, besides the height and length of the spoiler, and the azimuth location directly affects shock generation and its propagation. As a result, the controlled-shock modifies the surface

pressure on specific local regions and regions of the fins. On configuration 6, the spoiler used on configuration 4 is split into two, which are putted at specific azimuth locations, shown in Figure 5-15. The shocks induced by these two spoilers interact with each other and directly modify the pressure on fin 3, 4 and 5, which is different with configuration 4. On configuration 4, one oblique shock is generated and the core of the shock only interacts with fin4 (see Figure 5-6). Compared with configuration 4, the pressure on fin 3 and fin 5 is more significantly altered on configuration 6. As shown in Figures 5-7 to 5-12, the pressure rising on these two fins determines the nose-up pitching moment generated at negative angles of attack. As such, a larger nose-up pitching moment is produced on configuration 6 at -10° angle of attack. This suggests additional efforts need to be conducted to strategically place and arrange the spoilers on the model.

Chapter 6

Dynamic Deployment of Spoilers

6.1 Methods of Study

The Wake-Fin Tailoring method is designed to have a fast control-response ratio. Due to limitations of the current experimental facility, it is difficult to experimentally investigate effects of the deployment process on the flowfield and associated pressure distribution. As such, a CFD study of the dynamic deployment of spoilers was conducted and the results are presented in this chapter.

Due to the motion of the spoiler, the shape of the computational domain is changing with time. The so-called dynamic mesh models need to be used to update the volume mesh in the deforming regions. The update of the volume mesh is handled automatically by the solver at each time step based on the new positions of the moving boundaries. To use the dynamic mesh model, a starting volume mesh and the description of the motion of the moving zones need to be provided. In the present study, a user-defined function (UDF) was employed to describe the motion of the spoiler. The UDF was defined using DEFINE-CG-MOTION, in which the center of gravity motion of the spoiler was specified to provide the solver with a linear velocity at each time step. The solver used this velocity to update the node position on the dynamic zone based on solid-body motion.

To re-mesh the deforming regions at every time step, a high-performance dynamic layering method was applied. This method only works with the structured mesh as was used in the present study. Using this method, the layers of cells adjacent to the moving spoiler will be added or removed based on the height of the layer adjacent to the moving surface. A sliding interface technique was also used to connect the moving zone with its adjacent regions.

Inherently, the deployment of spoilers is dynamic resulting in time-dependent flow computations. Therefore, 3D unsteady RANS simulations were conducted to simulate the whole deploying process. To obtain accurate flow predictions, the grid density and time step were determined by following the guidance provided by Cummings et al [78]. Some rules of thumb were employed to generate the grids, which included the first grid point away from the surface should be located at $y^+ \leq 1$ and a grid-stretching ratio of approximately 1.05 in a boundary layer. Based on the previous grid independence studies, a mesh with 3,896,272 cells was generated for present simulations.

Due to the limitation of the solver, dynamic mesh simulations currently work only with first-order time advancement, which introduces first-order truncation error. As is known, the overall time-discretization error is determined by the choice of temporal discretization and the manner in which the solutions are advanced to the next time step. In the present study, iterative time-advancement (ITA) scheme was used for time stepping. The ITA scheme is a direct extension of steady flow solution techniques to solve unsteady flow [79]. In this method, a steady flow solution technique is used interactively to obtain a converged solution for each time-level. The ITA scheme can account for the nonlinearity in each component of the momentum equation and the nonlinear coupling of three-dimensional velocity components through the interactive solution of the flow equations.

There is a general "rule of thumb" for the choice of time step: the time step should be determined by the temporal aspects of the flow feature(s) of interest in the computations [78 and 80]. Instead of using Strouhal number, Cummings et al [78]

suggested a non-dimensional time step of $\Delta t^* = 0.01$($\Delta t^* = \Delta t U/L$, where L is a characteristic length of the model) to be used as a starting point for the calculations. Following this guidance, a time step of $\Delta t = 0.0001s$ second was used in the present study. The height of the spoiler and the speed of deployment are 10.16 mm and 0.1 m/s respectively, yielding a deployment time of 0.1016s. As such, the time step in the deployment process is 1016. The total time step is fixed at 1500 in the current study.

For the unsteady simulation, the converged steady RANS solution was taken as the initial field. Then, unsteady RNAS simulation of finless baseline was carried out. After the unsteady simulation was converged to a period state, the UDF was applied and the spoiler started to deploy. As shown in Figure 6-1, the spoiler was deployed at 1.0383s with a constant speed of 0.1 m/s, and was stopped at 1.1399s.

6.2 Visualization of Vortices

It is widely agreed that vortices belong to the most important coherent features in a flow field. The concept of a vortex is common in fluid dynamics and has proven useful to describe and model the behavior of fluids, even through there is no formal and precise definition for a vortex. Robinson [81] proposed a most intuitive definition for a vortex: *A vortex exists when instantaneous streamlines mapped onto a plane normal to the vortex core exhibit a roughly circular or spiral pattern, when viewed from a reference frame moving with the center of the vortex core.*

Jiang et al [82, 83] reviewed several vortex detection algorithms and they categorized these methods into three groups. The first group of methods is based on isosurfaces of scalar field. The second one is based on the extraction of vortex core lines. The third group of methods is based on the geometric properties of streamlines. Among these groups, the first group of methods is widely-accepted. In the present study, helicity method together with Q-criterion method was used to detect

and visualize the vortex structure downstream of the spoiler.

Helicity density is defined as the scalar product of the local velocity and vorticity vectors. Since it indicates both the strength and sense of rotation of the vortices, helicity density has been found to be excellent means of visualizing the position and strength of the vortex pattern. The use of helicity density filters out the regions of low vorticity (far from the body), as well as regions of high vorticity, but low velocity particularly where the angle between the velocity and vorticity vectors is large (very close to the body in the boundary layer). High values of helicity density reflect high values of speed and vorticity when the relative angle between them is small. The sign of helicity density determined by the sign of the cosine of the angle between the velocity and vorcicity vectors. Thus, the sign of the helicity density indicates the direction of swirl of the vortex relative to the streamwise velocity component, which changes across every separation or attachment line. By marking positive and negative values of the helicity with different colors, it is easy to differentiate between the primary and second vortices [84, 85]. However, it was found by Moth [86] that the extracted core line might not always correspond to the actual vortex core line. Helicity method is a line-based method, which specifies criteria for locating vortex core lines [83]. This method is usually combined with other detectors to help to distinguish between connected regions of counter-rotating vortices.

Together with line-based helicity method, a region-based detector, Q-criterion, is used to identify contiguous grid cells that belong to either the vortex or its core [83]. Q-criterion was proposed by Hunt and others [87] in 1988, which is a kind of Galilean-invariant definitions of a vortex using invariants of the velocity gradient tensor. Vortex core is identified as a connected region where $Q > 0$ and the pressure is lower than the ambient value. Please see appendix A for detailed definition.

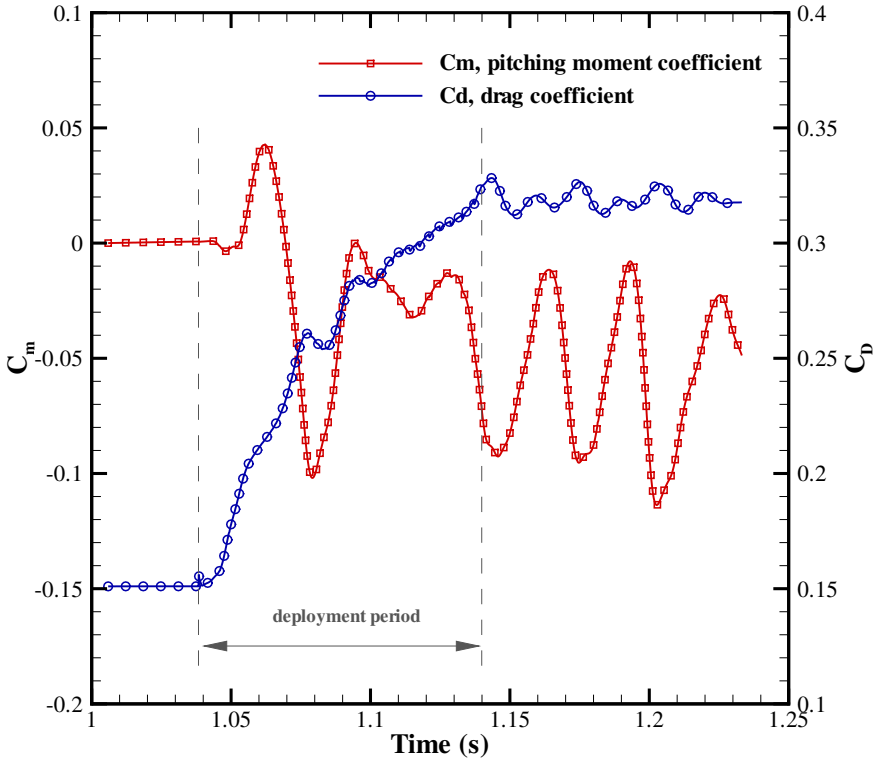

Figure 6-1: Effect of control on pitching moment and drag coefficient as a function of time.

6.3 Numerical Results

Before the results discussion, it is worth to notify that the center of gravity is centrally located at x/L=0.45 as shown in Figure 6-2. Figure 6-1 shows the time histories of drag coefficient and pitching moment coefficient. The drag was changed immediately upon the spoiler deployment, and kept rising during the entire deployment period. When the spoiler was fully deployed, the drag coefficient stopped increasing and then oscillated with a certain frequency. Detailed analysis was conducted to determine the drag increment contributions. It was found the main contribution to the total drag increment came from the pressure drag of the boattail. The boattail drag coefficient increased from 0.08 to 0.21 through the deployment process. Considerable contribution also came from the spoiler, producing an additional drag coefficient as high as 0.034. At the same time, it was observed that the nose drag and main body

drag were almost constant during the whole process.

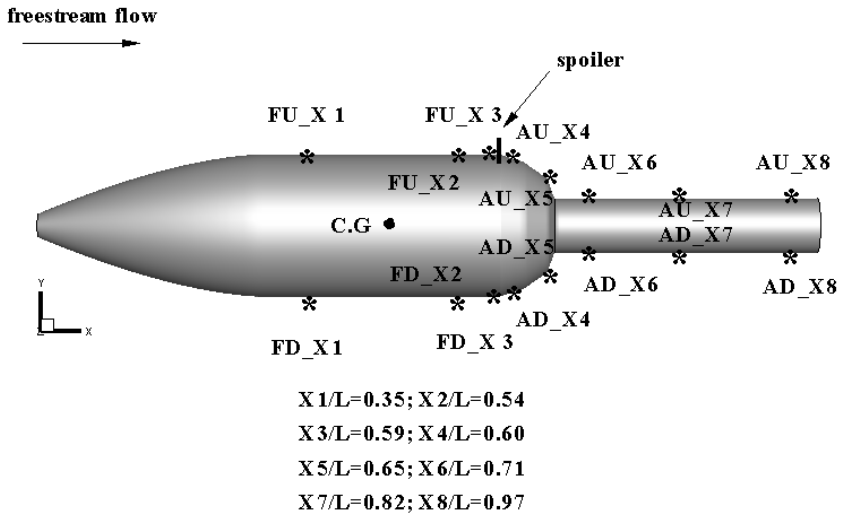

Figure 6-2: Illustration of the cross-stream sections.

In Figure 6-1, the time history of pitching moment coefficient shows strong unsteadiness. A sharp rise in the pitching moment was first observed and a positive coefficient peak of 0.5 was reached at about 1.0614s, corresponding with the spoiler at a position of 2.31 mm. A sharp drop to negative then occurred, with a valley of -0.1 was reached at 1.079s where the spoiler has increased to 4.07mm. Following this negative valley, the pitching moment coefficient increased again to a level near zero. After experiencing one more drop and rise cycle, the pitching moment became oscillatory but remained negative (nose-down) at all time during the oscillation.

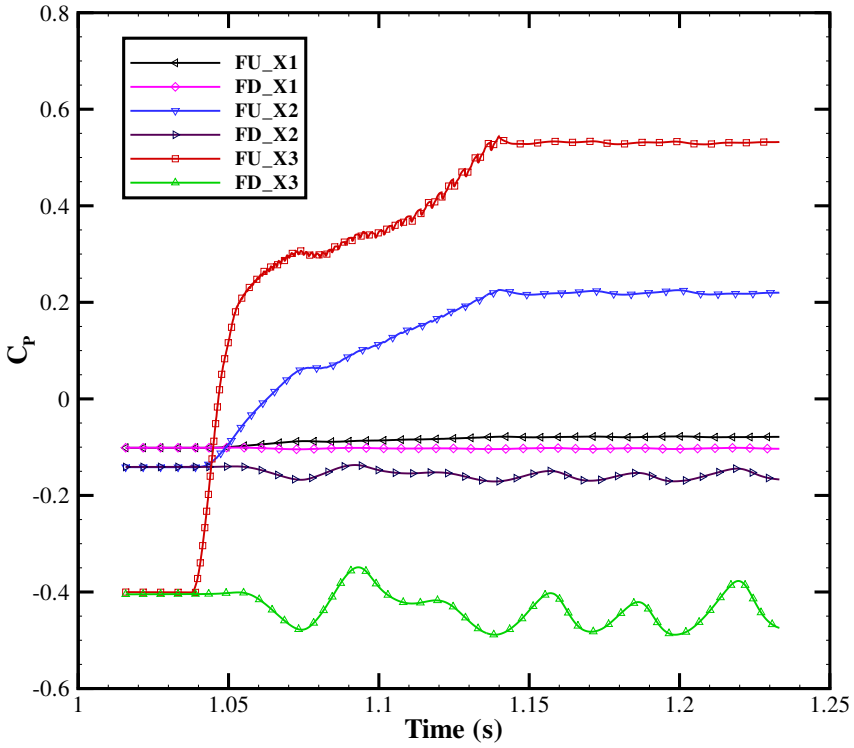

Figure 6-3: Time history profiles of pressure coefficient at points X1 to X3 located upstream of the spoiler.

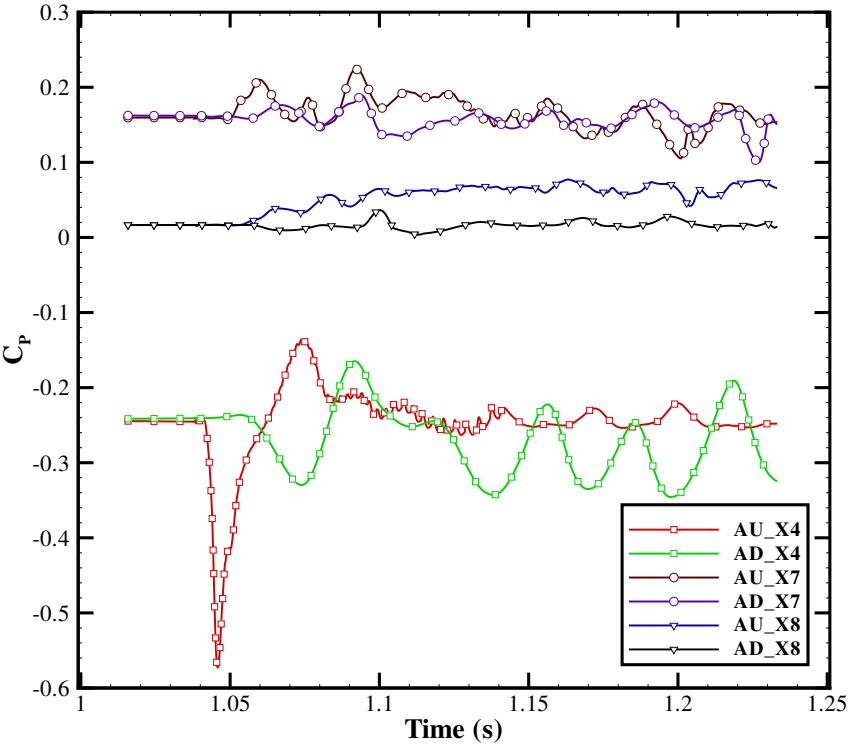

Figure 6-4: Time history profiles of pressure coefficient at points X4, X7 and X8 located downstream of the spoiler.

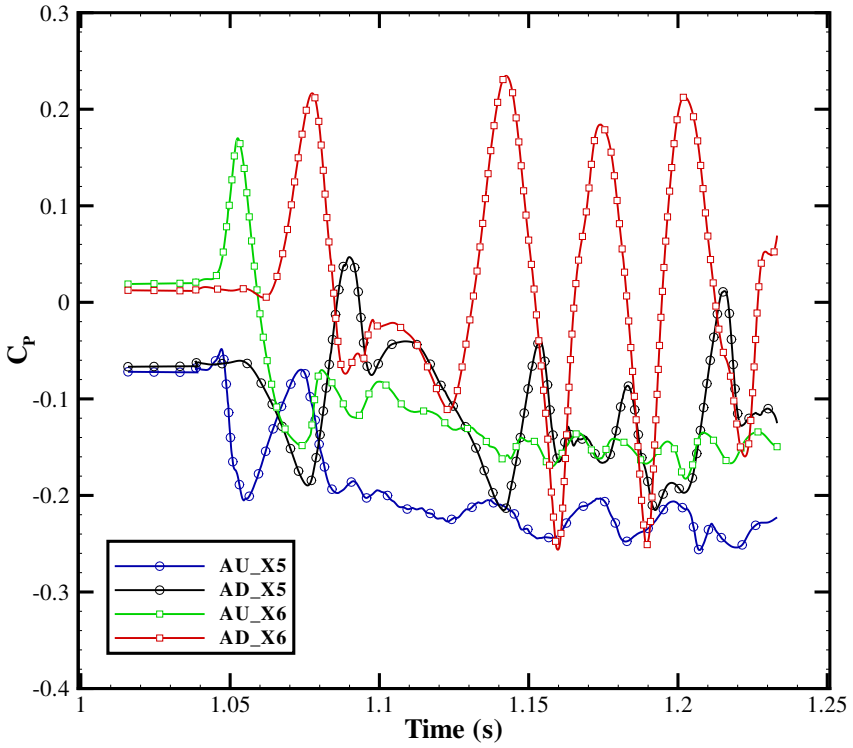

Figure 6-5: Time history profiles of pressure coefficient at points X5 and X6 located on tail-piece.

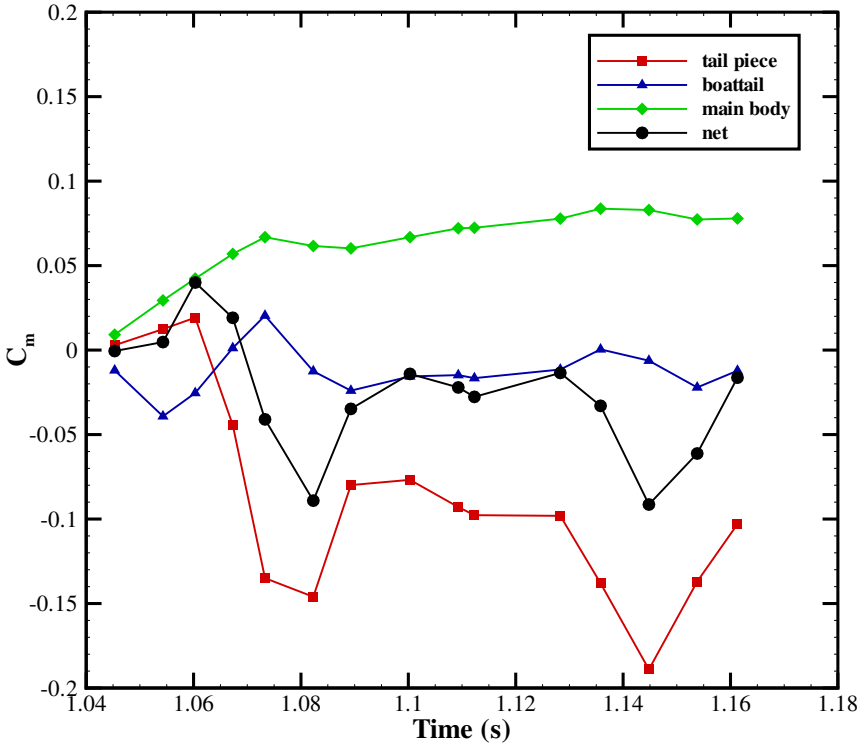

Figure 6-6: Time history profiles of net pitching moment and its components.

To help explain the unsteady behaviors of pitching moment coefficient, time histories of surface pressure distribution are presented in Figures 6-3, 6-4 and 6-5. The positions of monitored surface points are illustrated in Figure 6-2, in which the captive F and A mean forebody and aftbody respectively. In Figure 6-3, the time history of surface pressure upstream of the spoiler is presented. The results indicate the spoiler modifies the local and far upstream pressure loadings. The pressure difference between the upper and lower surfaces indicates a negative normal force should be produced. On the upper surface where the spoiler locates, the pressure is rising during the entire deploying process. After the deployment is completed, the upper surface pressure becomes constant. This indicates incoming flow interacts with the deployed spoiler in a relative steady manner. In comparison to the upper surface, the lower surface pressure is less modified by the spoiler but more unsteady. Even after the spoiler is fully deployed, the lower surface pressure remains oscillatory.

Surface pressure distributions downstream of the spoiler are presented in Figures 6-4 and 6-5, where the pressure coefficients are plotted as a function of time. Pressure fluctuations are observed at all the monitored points. Additionally, the fluctuations in pressure occur at both periodic and irregular manners during and after deployment. This indicates that the pressure fluctuations during and after deployment of the spoiler are produced by different unsteady behaviors of wake flow. Deployment of the spoiler is essentially an unsteady process, which determines the pressure fluctuations downstream of the spoiler during deployment. After deployment, the pressure fluctuations are produced by inherent instabilities of the asymmetric wake flow.

In contrast with upstream of spoiler where the pressure difference between upper and lower surfaces is almost linearly increasing as a function of the deployed height of the spoiler, the pressure difference downstream of the spoiler exhibits different degrees of oscillatory behaviors depending on the location. The phenomenon is particularly obvious at cross-stream sections at the front portion of the tail-piece such as X5 and X6 shown in Figure 6-5. As a result, the normal forces and corresponding pitching

moments generated on tail-piece can vary significantly with time. The results therefore indicate that the unsteady behavior of the pitching moment is caused by the surface pressure oscillations downstream of the spoiler where flow separation occurs and results in an unsteady vortex wake.

Pitching moment contribution analysis was conducted and the results are shown in Figure 6-6. It was found that the main contributions to the pitching moment came from main body, boattail and tail-piece. With the center of gravity located at (0.28, 0, 0), nose-up pitching moment is generated on main body. This pitching moment rises during the initial deployment of the spoiler, and reaches an almost constant level well before the deployment is completed. This constant level is a result of the balance between the nose-down and nose-up pitching moments produced upstream and downstream of the center of gravity respectively. As shown in Figure 6-3, a nose-down pitching moment is generated at front portion of the main body where the flow-spoiler interaction propagates upstream of the spoiler and alters the pressure. Figure 6-6 shows that considerable pitching moment is also produced on boattail. The time-varying moment is due to the pressure fluctuations at the boattail, as shown in Figure 6-4. For example, Figure 6-6 shows negative and positive peaks of pitching moment occur at 1.05 and 1.07 second respectively. At the same times, the pressure differences between upper surface (red line in Figure 6-4) and lower surface (green line in Figure 6-4) of the boattail are negative and positive respectively.

Figure 6-6 shows that the total pitching moment is mainly determined by the pitching moment produced on the tail-piece. The oscillation amplitude of tail-piece-generated pitching moment is much larger than that of main body and boattail. As such, the time-varying behaviors of the total pitching moment and tail-piece-generated pitching moment are strongly correlated. For example, negative perks of both pitching moments occur at about 1.085 and 1.142 seconds.

Further analysis was carried out to gain insights into the unsteady flow physics. Figure 6-7 displays the contours of y-velocity component in cross-stream sections of

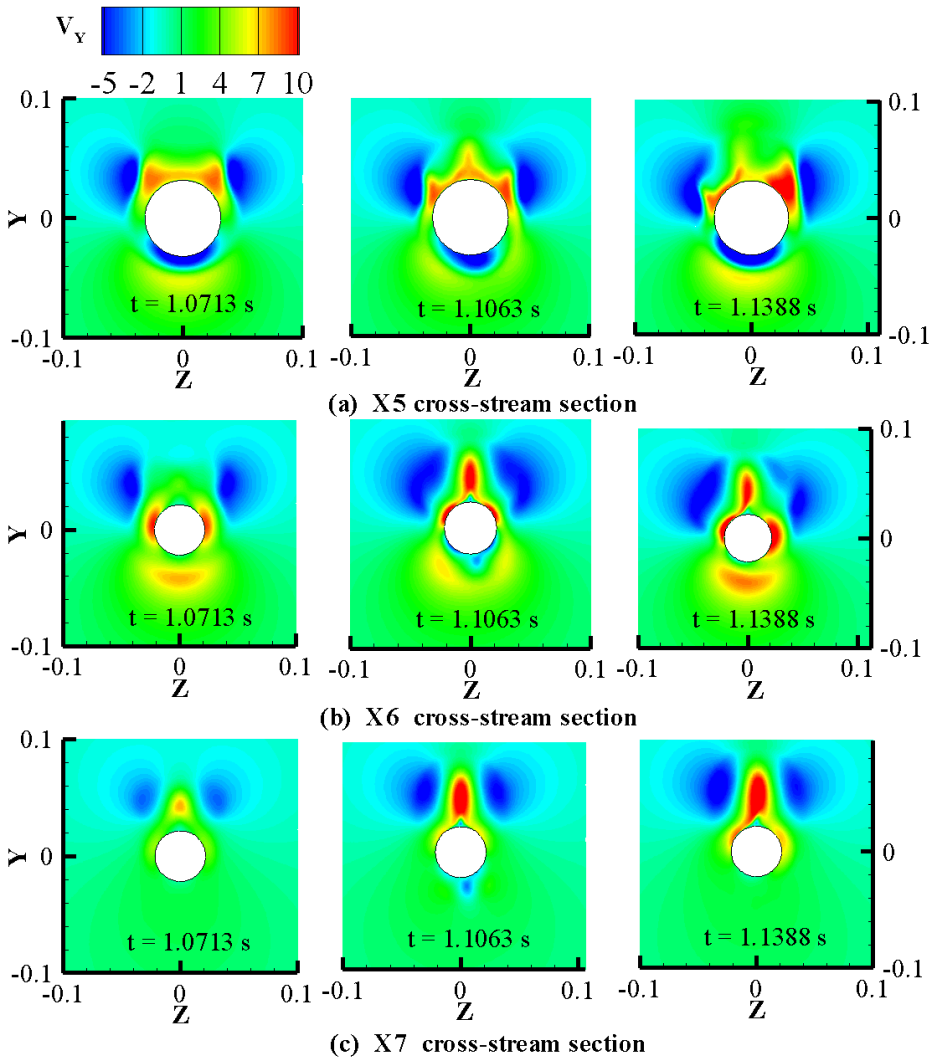

Figure 6-7: Y velocity contours in cross-stream sections of X5,X6 and X7.

X5, X6 and X7 (see Figure 6-2) at different deploying times. As can be seen in the figure, the velocity of asymmetric wake flow has a significant y-component in contrast to the flow upstream of spoiler where the x-axis flow dominates. As indicated by the red regions in the subfigures, close to the surface a significant y-component of velocity is generated, At 1.0713 second the near-surface flow and associated vortices are symmetrical about the z-axis. The flow becomes slightly asymmetric at 1.1063s and significantly asymmetric at 1.1388s especially at the section of X6. This is similar to the well-known vortex asymmetry phenomenon in flows over slender bodies.

At 1.1388 second, computational results show the values of side force and yawing moment, which mainly come from the tail-piece, to be 0.016 and -0.034 respectively.

Literature reviews and the above analysis suggest that downstream pressure fluctuation and associated pitching moment oscillation may be explained by the wake vortex structures. Herein, contour of helicity density and display of isosurface with specific positive Q value are used to visualize the vortex flow.

Figures 6-8 to 6-13 compare the helicity density contours in different cross-stream sections at 1.0233 second (control off) and 1.1066 second (control on). As shown in Figure 6-8, there is no helicity upstream of the boattail before the spoiler is deployed. After the spoiler is deployed at 1.1063s, however, its upstream influence is evident by the presence of the opposite-sense helicity. In the absence of a spoiler, the flow separates in an axial symmetric manner at the start of the boattail section. Farther downstream at x = 0.395, shown in Figure 6-9, natural flow instabilities cause the separated shear layer to break into four streamwise patterns. The presence of a spoiler breaks the initially axial symmetric separation. The growth of the streamwise instability is thus enhanced and results in the highly 3-dimensional helicity pattern shown in Figure 6.9. As can be seen in Figure 6-10, the patterns of instability growth for both control and un-control cases persist downstream. For control case, this flow phenomenon is also clearly shown in Figure 6-19. The helicity in Figure 6-13 shows that at x = 0.57 the controlled flow evolves into a pair of strong vortices near the tail-piece, which are wrapped by a pair of weaker vortices. The reversed colors (blue and red) of helicity density indicated the swirling directions of these two vortices are opposite. This suggests new kind of vortical flow near the tail-piece is formed after flow is reattached. The developing process is visualized and shown in Figure 6-19. Furthermore, the secondary vortexes will be induced if the near-wall vortical flow is sufficient strong.

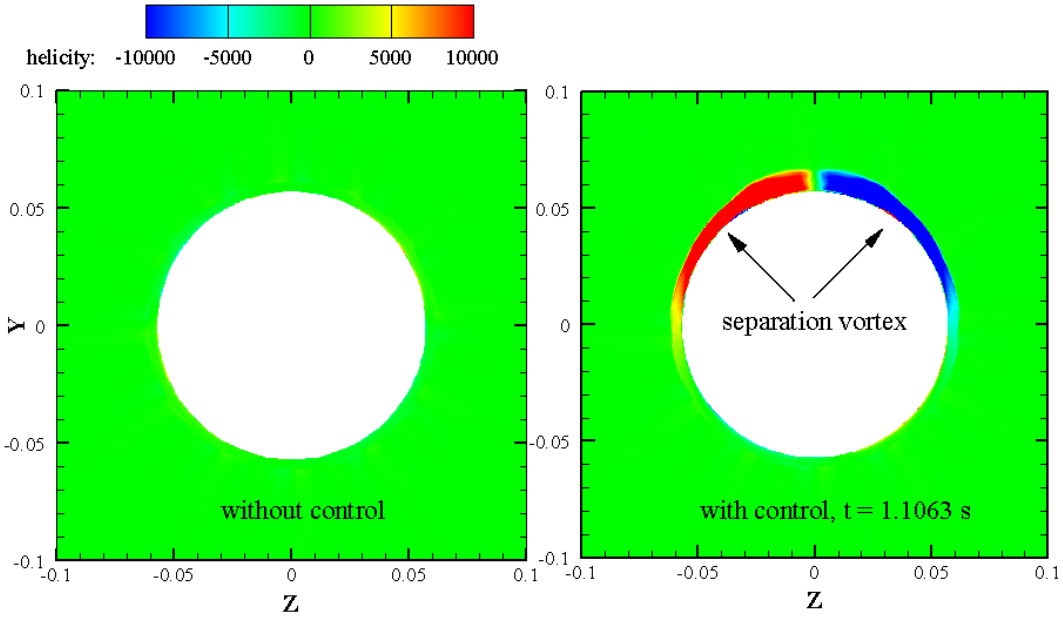

Figure 6-8: Helicity density contours in cross-stream section of x=0.364.

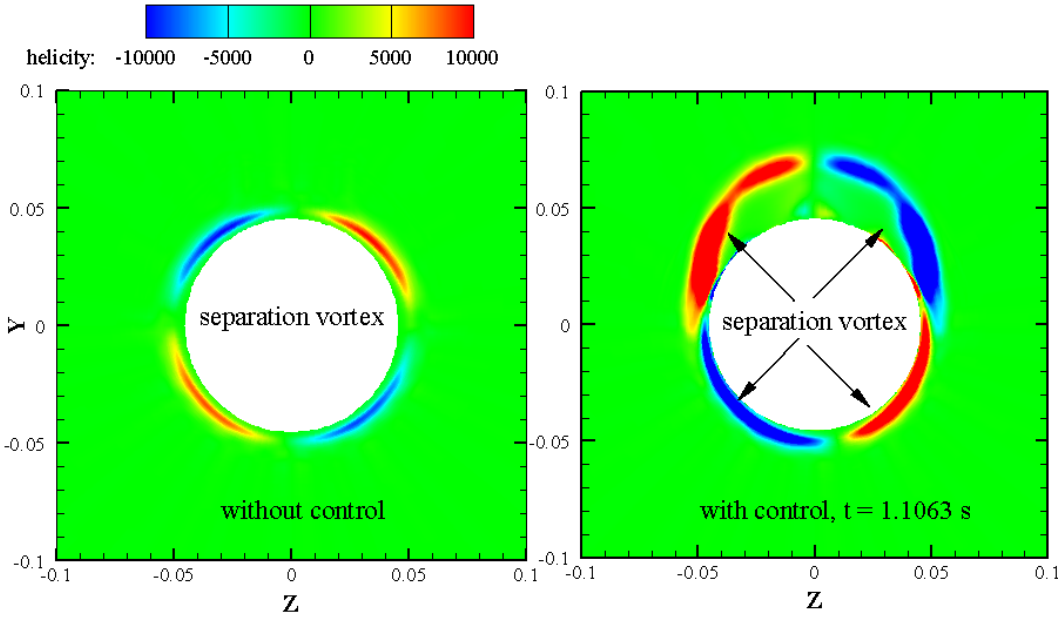

Figure 6-9: Helicity density contours in cross-stream section of x=0.395.

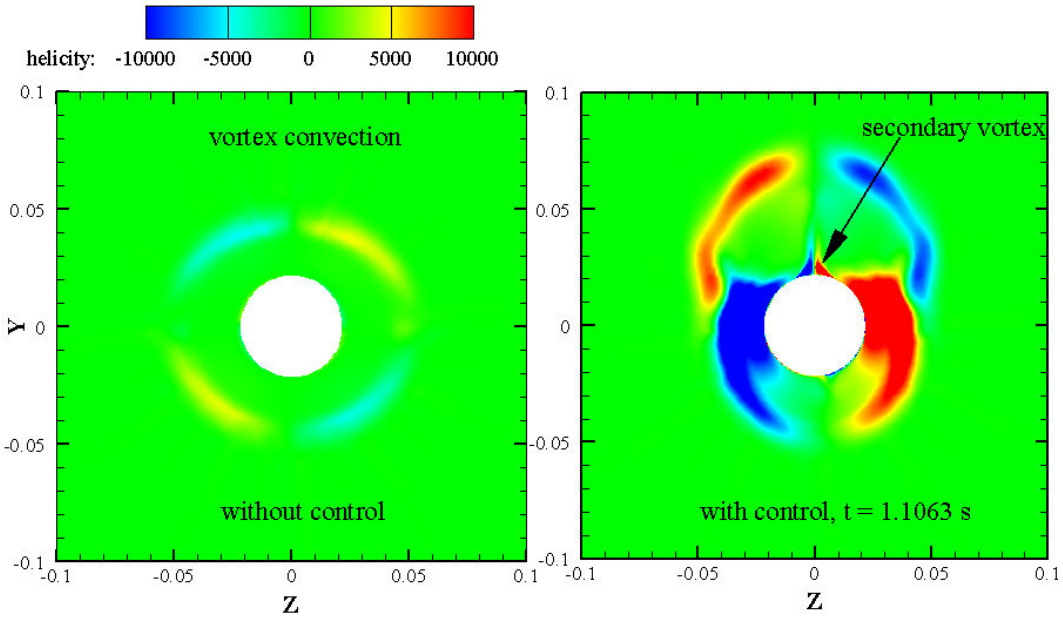

Figure 6-10: Helicity density contours in cross-stream section of x=0.42.

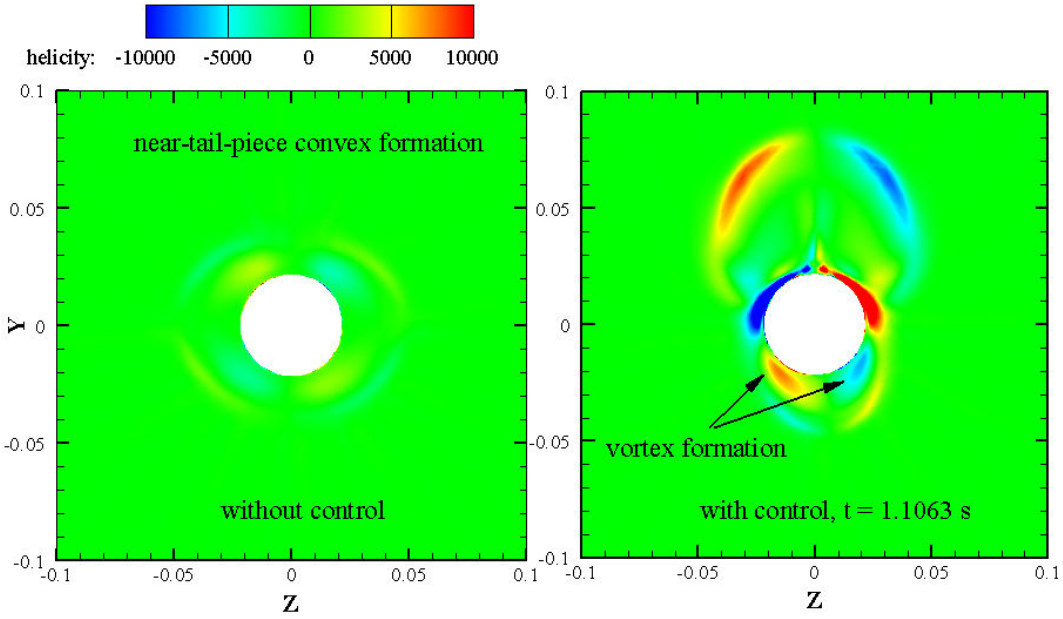

Figure 6-11: Helicity density contours in cross-stream section of x=0.47.

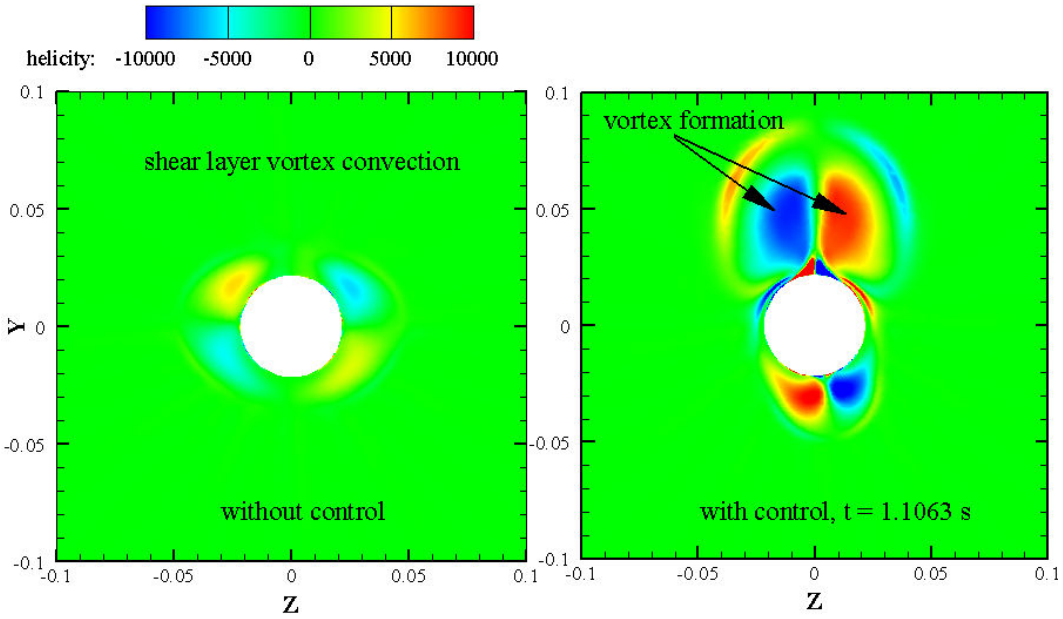

Figure 6-12: Helicity density contours in cross-stream section of x=0.52.

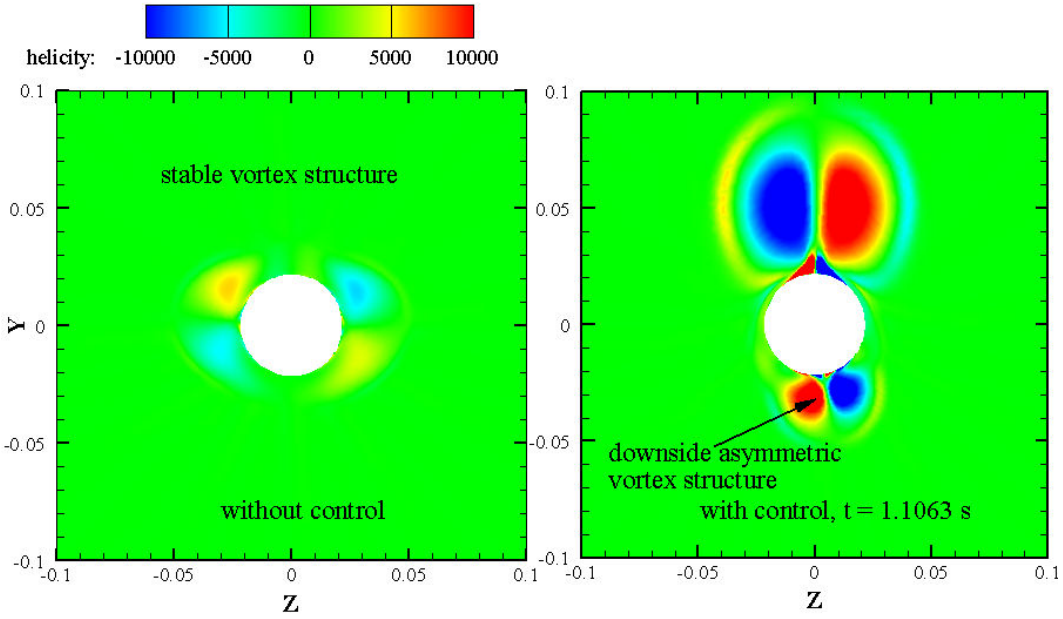

Figure 6-13: Helicity density contours in cross-stream section of x=0.57.

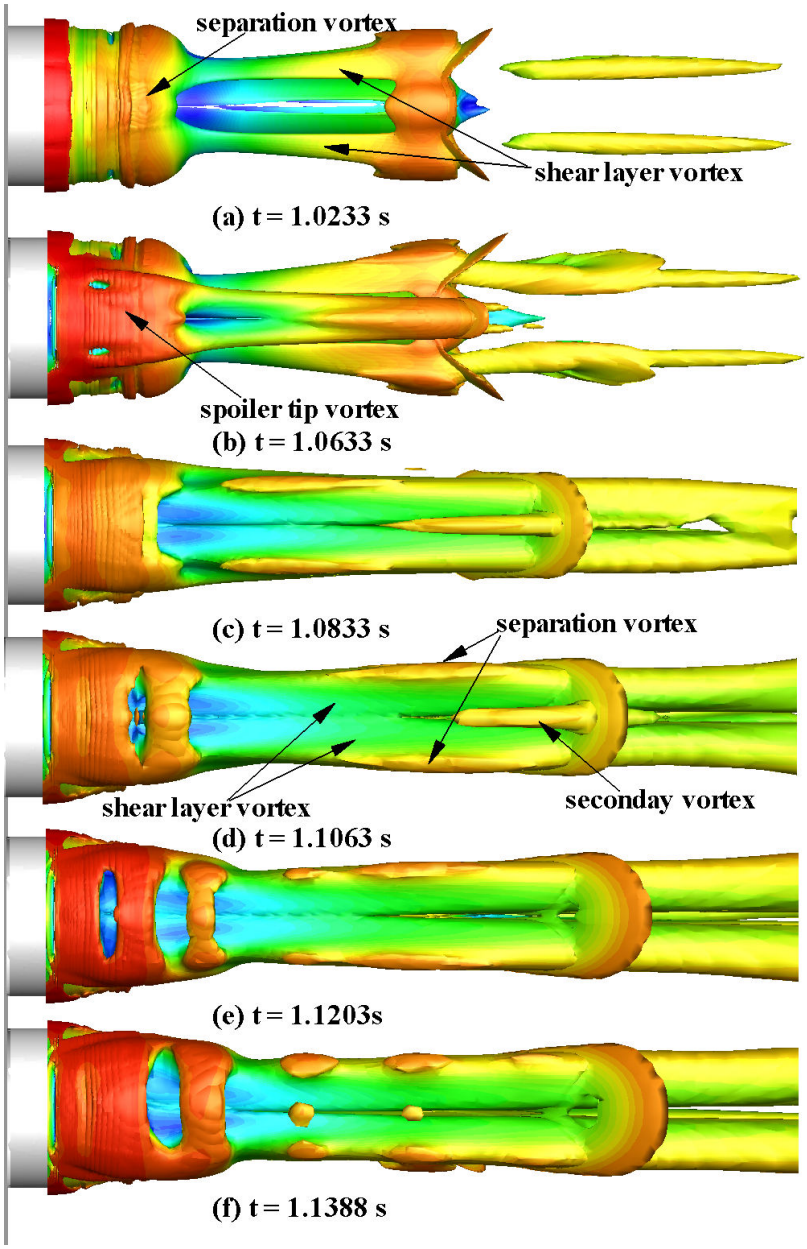

Figure 6-14: Instantaneous isosurfaces of Q-criterion (Q=1000) during deployment colored by velocity magnitude (top view).

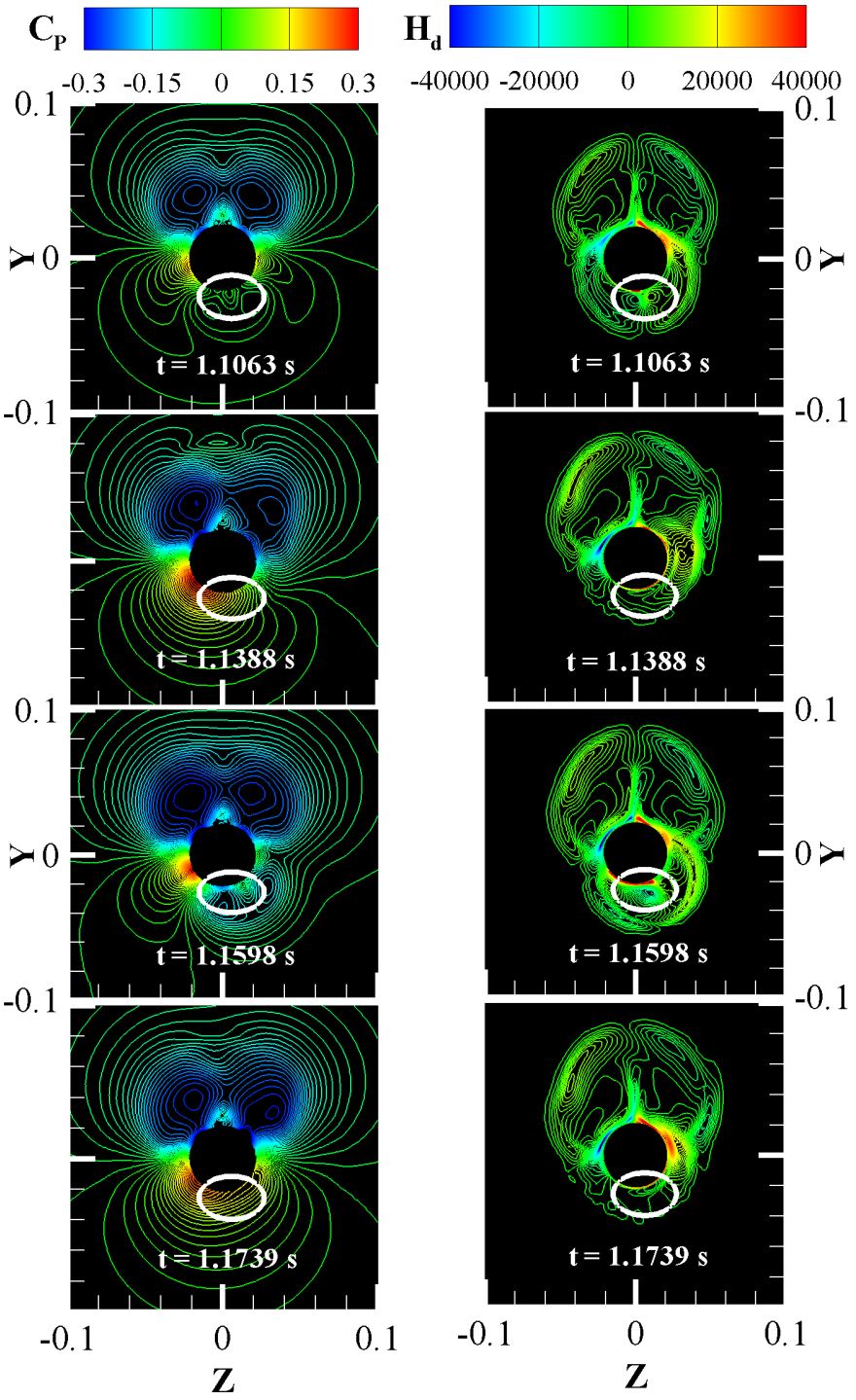

Figure 6-15: Pressure coefficient and Helicity density contours in cross-stream section of x6 at different times.

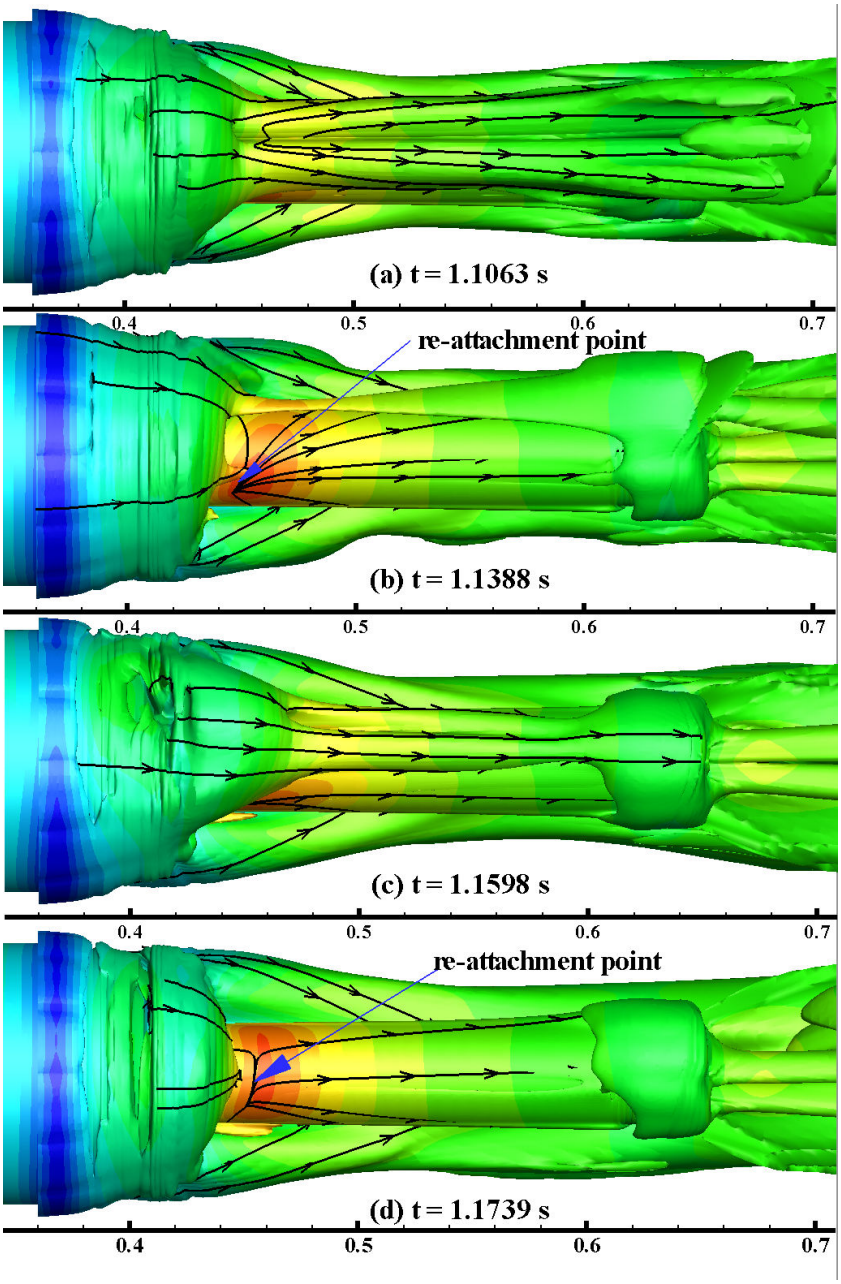

Figure 6-16: Instantaneous isosurfaces of Q-criterion (Q=1000) during deployment colored by pressure coefficient (down view), combining with stream traces.

The vortex structure along the tail-piece detected above was also revealed by using Q-criterion method. In Figure 6-14, isosurfaces (colored by velocity magnitude) of Q = 1000 at varying times during deployment are presented to visualize the vortex structure downstream of the spoiler. Comparing Figure 6-8 to 6-13 with subfigure (a) and (d) in Figure 6-14, the vortex structure revealed using these two methods is identical. Q-criterion method provides connected vortex information, and the sign of helicity method helps to identify different kinds of vortex.

Figure 6-15 shows the pressure coefficient and helicity density contours in the cross-stream section of X6 at different times. X6 is where the largest amplitude of pressure fluctuation is detected. The results show that the upper surface pressure is relatively stable after the deployment is completed (1.1388 second), but the lower surface pressure varies significantly with time. There is a high pressure region (red color) at lower left side, which may have been induced by the asymmetrical vortices (see Figure 6-9). As shown in Figure 6-5, the pressure at the lower surface (AD_X6) is negative at 1.1063 and 1.1598 seconds and positive at 1.1388 and 1.1739 seconds. As shown in Figure 6-15, significant helicity density and secondary vortices can be detected at 1.1063 and 1.1598 seconds.

The vortex structures in Figure 6-15 are also revealed in Figure 6-16 using the Q-criterion method. The shear layer vortices are observed at 1.1063 and 1.1598 seconds, shown in subfigures (a) and (c) in Figure 6-16. A reattachment point is identified in Figure 6-16, corresponding to a relative high pressure (red) area. This high pressure region can be also detected in Figure 6-15.

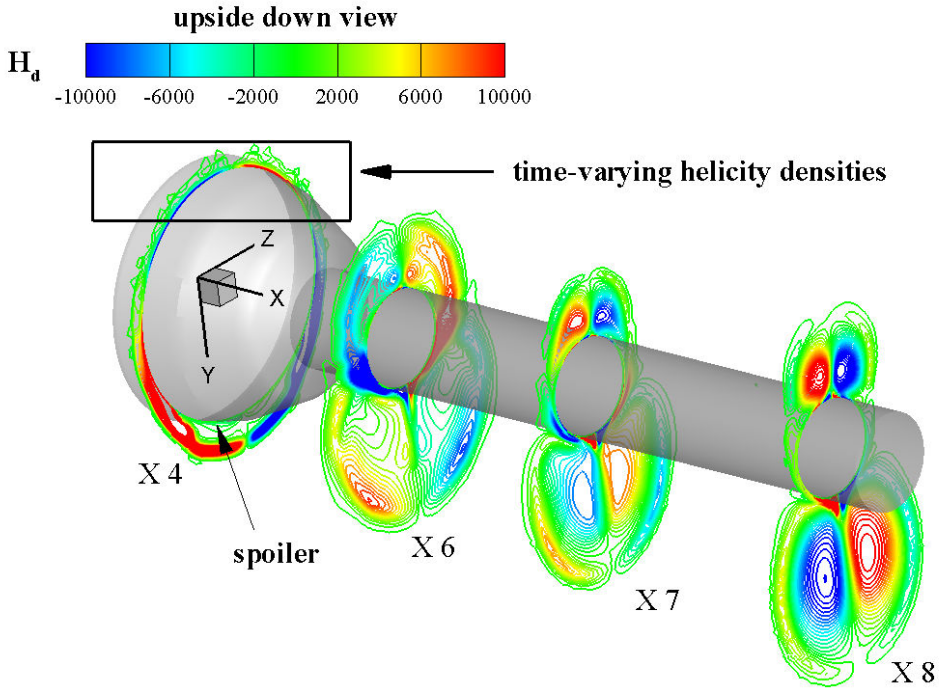

Figure 6-17: Helicity density contours in cross-stream section at 1.1063 second.

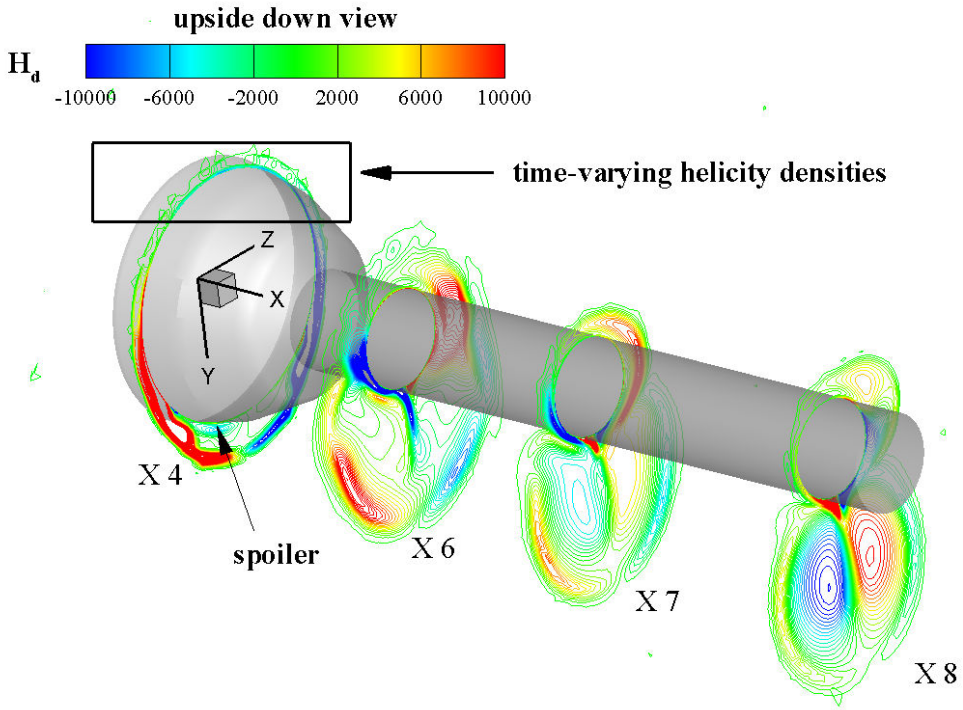

Figure 6-18: Helicity density contours in cross-stream section at 1.1388 second.

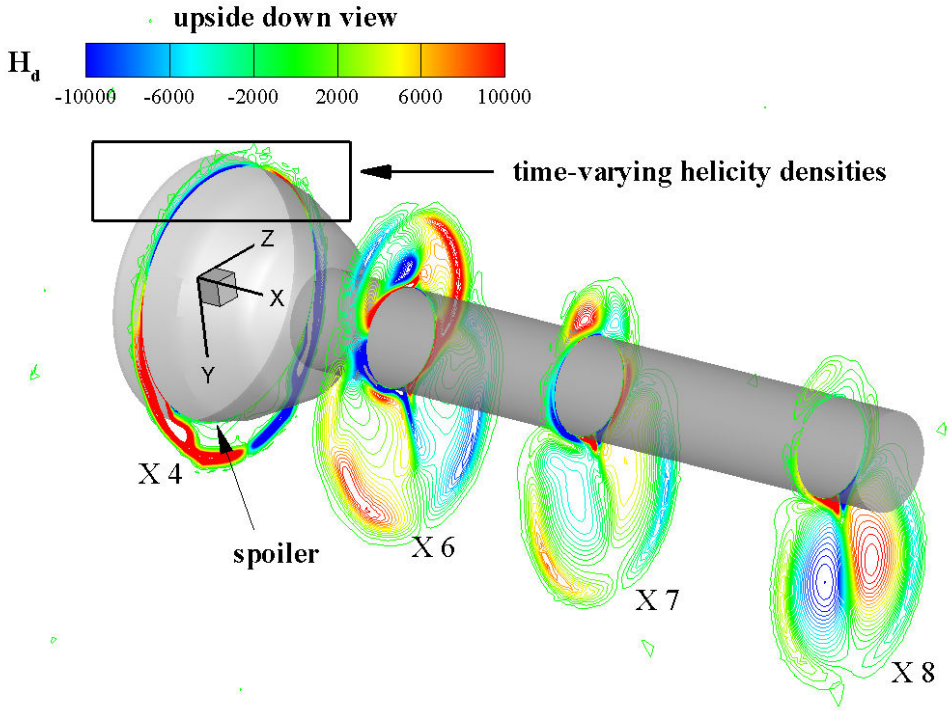

Figure 6-19: Helicity density contours in cross-stream section at 1.1598 second.

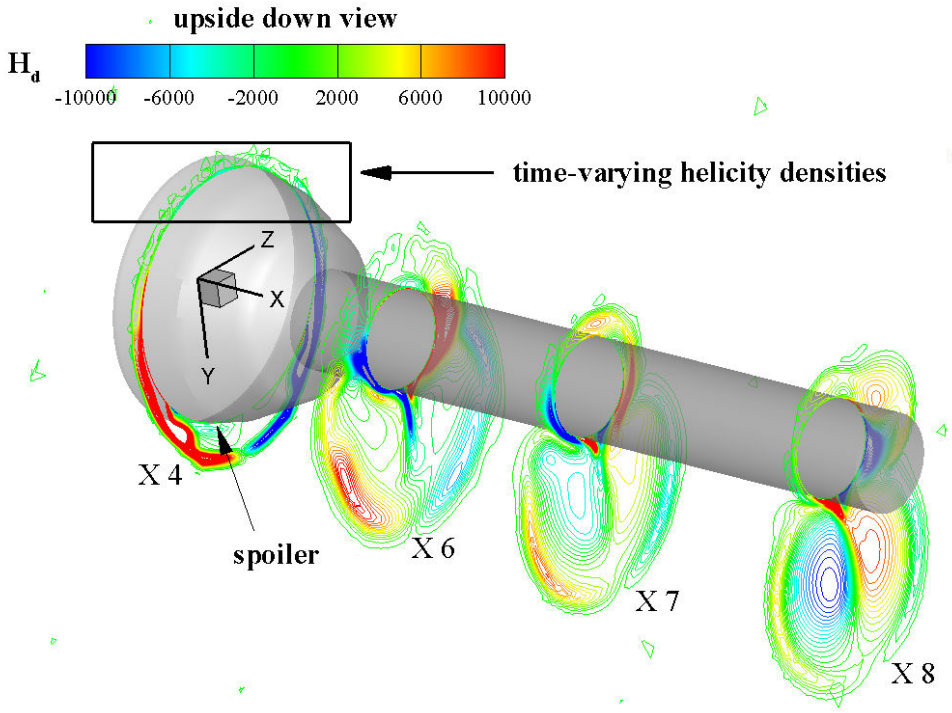

Figure 6-20: Helicity density contours in cross-stream section at 1.1739 second.

Figures 6-17 to 6-20 show the helicity density contours in different cross-stream sections (as in Figure 6-2) at the same times as in Figure 6-15. Note that the coordinates are upside down in these figures. The figures identify the vortex resources for in the flow over the tail-piece. They further confirm the behaviors of the flow are as discussed previously. The lower surface helicity density (circled region) varies significantly with time. As can be seen in Figure 6-17, the roughly symmetrical helicity density distribution in X4 section produces symmetrical flow behavior downstream of boattail. If the distribution is made asymmetrical, for instance by the spoiler, the downstream flow will be asymmetrical as shown in Figure 6-18. If the vortices are sufficiently strong, as in Figures 6-17 and 6-19, the vortices will induce secondary vortices in section X6.

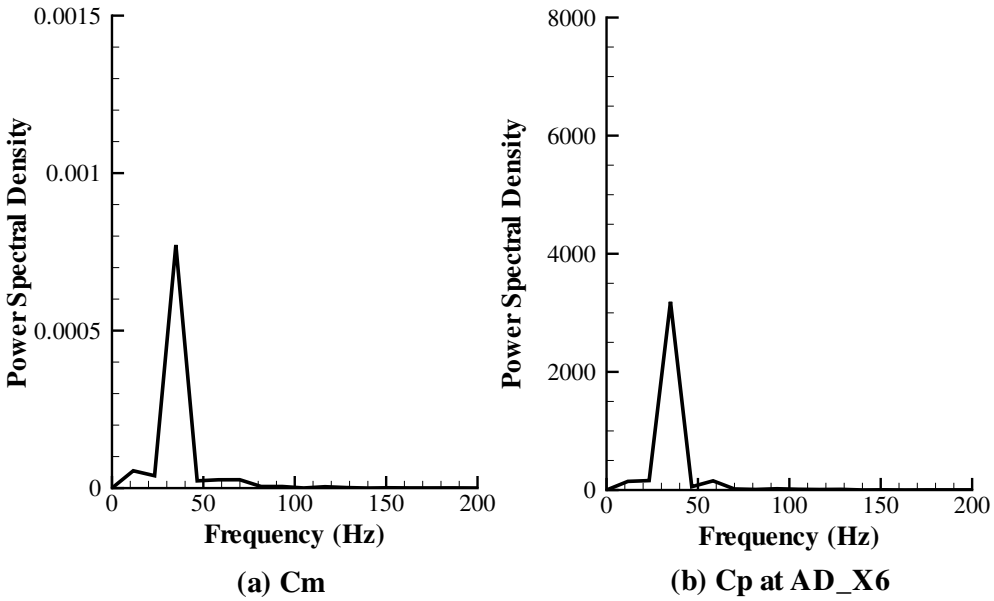

Figure 6-21: Power spectrum of pitching moment and pressure coefficient at AD_X6 obtained using URANS.

Both the helicity contours and isosurface of Q indicate the variation of pressure in time is related to the turbulent structures associated with the flow separation occurred just downstream of the spoiler. As discussed, the pitching moment is mainly determined by the force on the tail-piece. The largest amplitude of pressure fluctuation on

tail-piece occurs at the front portion such as near X6. The periodicities of separation are associated with eddy shedding, wake flapping, variation in reattachment position, time between reversals within separation zone and upstream structures. Figure 6-21 shows the spectral power densities of the pitching moment and pressure coefficient at AD_X6. The results show that the peak frequencies of pressure and pitching moment variation are identically at 35 Hz.

Based on the maximum diameter of the body, the St calculated using the peak frequency from Figure 6-21 is about 0.16, which is within the range for vortex (eddy) shedding. Based on the various results presented, the frequency of pitching moment variation is determined by the vortex shedding occurred downstream of the spoiler.

Chapter 7

Summary and Future Work

A novel active flow control method, named Wake-Fin Tailoring method, was evaluated for improving the steering performance and attitude control of a projectile at low angles of attack. Proof-of-concept experiments were conducted in subsonic wind tunnel to access the feasibility of the control concept and optimize the control performance. CFD simulations at supersonic flow regimes were carried out to quantify the effect of compressibility on the actuator's effectiveness. Additionally, unsteady CFD modelings of spinning model and dynamic deployment of actuators were performed to study dynamic behaviors of the control.

The proposed control method is aimed for applying to Army's next-generation LOS-MP munitions. The fin-stabilized LOS-MP projectile features a reduced-diameter tail-piece with six tail fins. Geometric constraints prevent the incorporation of a flow control system at aft body section which is typically the most effective location for control deployment. As such, the Wake-Fin Tailoring method is developed to make use of flow control actuators mounted at the middle-section boattail. The Wake-Fin Tailoring method not only rely on modifying the local pressure loading to fulfill the control objective, but also takes advantage of interactions between the main body wake and tail-fins to change the pressure and thus force distributions on the tail-fins. As a result, larger control authority and wider control bandwidth are expected to be

generated with smaller penalty of drag increment compared with other active flow control methods proposed and studied recently.

The experimental and numerical results can be summarized as follow.

1. Results from experimental investigations on the use of deployable miniature spoilers show significant aerodynamic forces can be generated and effectively used to steer and maneuver projectiles.

2. Experimental parametric and configuration studies reveal that the most effective configuration for pitch control is with the spoiler on the top or bottom of the boattail. As expected, the control force scaled with the size of the spoiler. The results further indicate that the most effective control performance is generated at negative angles of attack, especially from -10° to -2° where the spoiler is at the windward side.

3. The effect of Mach number on control effectiveness was qualified. The magnitudes of pitching moments of cases with and without control are both reduced at supersonic regimes. Significant control effect was however still observed.

4. Both experimental and numerical flow visualizations show flow separation just downstream of the nose tip and downstream of main body due to the blunt nose and reduced-diameter boattail. When control is on, the boattail flow separation zone is enlarged and the pressure on tail-piece is significantly modified.

5. Computational results reveal a pair of counter-rotating vortices being produced by flow-actuator interaction. The vortices impinge on the tail fins to modify the pressure on the fins. As a result, a control moment is generated additional to the one on the main body.

6. When the projectile is spinning, the spoiler-induced vortices become asymmetric. Additionally, trajectories of the vortices shift in the circumferential direction. As a result, the pressures on different fins are changed compared with

the stationary case. The influence is dependent on the spinning speeds. The nature unsteadiness of asymmetric vortices causes considerable oscillations of the pitching moment generated.

7. The supersonic study shows that an oblique shock can be induced by the spoiler. The strength and transfer direction of the shock is determined by the free-stream flow and spoiler size. The study shows that the shock significantly modifies the pressure on certain areas of the fins depending on the angle of the shock. Furthermore, the aft body wake near the boattail and tail-piece is altered, which affects pressures on the tail-piece and root surface of fins.

8. Simulation results of the dynamic deployment of a spoiler indicate considerably unsteady behavior is produced due to motion of the spoiler. At angle of attack of 0°, the oscillation of pitching moment is mainly due to the flow over the tail-piece The frequency of oscillation appears to be determined by the vortex shedding downstream of the spoiler.

To further develop the use of deployable miniature spoilers for aerodynamic control, it is recommended that the following future works be conducted to fully access the effectiveness of the control and gain additional insights on the flow physics.

1. Wind tunnel experiments of a spinning model with dynamic deployment of spoilers can be carried out to evaluate the dynamic performance of the control. Currently, a model is completed and the LabView control VI is developed. A small step motor with high torque is however required to overcome rolling resistance.

2. Wind tunnel experiments at supersonic flow regimes are recommended to experimentally verify the effect of compressibility on the spoiler's effectiveness and validate the computational methodologies.

3. It was observed in the present study, the numerical results are likely sensitive

to the free-stream turbulence level. As such, the effect of turbulence level needs to be determined for the unsteady simulations.

4. High-resolution CFD methods can be used to verify the steady and unsteady RANS models used in the present study. Based on requirements for computer resource and time, hybrid LES/RANS modeling, such as Detached Eddy Simulation (DES), is recommended.

5. Analytical and modeling studies can be conducted using Missile Datcom and 6-DOF flight simulations to predict and optimize the endgame performance of the control spoilers.

References

[1] **Sdf Collis, S.S, Joslin, R.D, Serifert, A, Theofilis, V.**, "Issues in Active Flow Control: Theory, Control, Simulation, and Experiment," *Progress in Aerospace Science*, Vol.40, pp. 237-289, 2004.

[2] **Lopera J.**, "Aerodynamic Control of Slender Bodies from Low to High Angles of Attack through Flow Manipulation," *PhD Dissertation, the University of Toledo*, 2007.

[3] **Patel, Mehul P., Lopera, Javier, Ng, Terry. T.**, "Active Boattailing and Aerodynamic Control Fins for Maneuvering Weapons," *AIAA 2004-2696*, Jun, 2004.

[4] **Lopera, Javier, Ng, Terry. T., Patel, Mehul. P.**, "Experimental Investigations of Reconfigurable Porosity for Aerodynamic Control," *AIAA 2004-2695*, Jun, 2004.

[5] **Lopera, Javier, Ng, Terry. T.**, "Coning Motion Control of a Blunt-Nose Projectile Using Small Deployable Strakes," *AIAA 2007-3812*, Jun, 2007.

[6] **Lopera, Javier, Ng, Terry. T.**, "Yaw Control of a Blunt-Nose Projectile at High Angles of Attack Using Strakes," *AIAA 2007-0671*, Jun, 2007.

[7] **Patil, S.K.R, Ng, T. T, Patel, M. P.**, "Trajectory Control of a Small Caliber Projectile Using Active Transpiration," *AIAA 2007-3811*, Jun, 2007.

[8] **Gad-el-Hak, M.**, "Flow Control: Passive, Active, and Reactive Flow Management," *Cambridge University Press*, Cambridge, United Kingdom, 2000.

[9] **Gad-el-Hak, M., Pollard, A., Bonnet, J.P.**, "Flow Control: Fundamentals and Practices," *Springer Verlag Telos*, Springer-Verlag Berlin Heidelberg 1998.

[10] **Courty, Jean-Claude**, "Industrial Constraints and Requirements for Aeronautical Flow Control Application," Flow Control: Fundamental, Advances and Application, Lecture Series 2009-02, *Von Karman Institute for Fluid Dynamics*, 2009.

[11] **Cattafesta, L.N., Sheplak, M.**, "Actuators for Active Flow Control," *Annual Review of Fluid Mechanics*, Vol.43, pp.247-272, 2010.

[12] **Farnsworth, J. A., Vaccaro, J.C., Amitay, M.**, "Active Flow Control at Low Angles of Attack," *AIAA Journal*, Vol.46, No.10, 2008.

[13] **Sahu, J.**, "Time-Accurate Computations of Free-Flight Aerodynamics of a Spinning Projectile with and without Flow Control," *AIAA 2006-6006*, Aug, 2006.

[14] **Moreau, E., Benard, N.**, "Plasmas for Flow Control," Flow Control: Fundamental, Advances and Application, Lecture Series 2009-02, *Von Karman Institute for Fluid Dynamics*, 2009.

[15] **Gnemmi, P., Rey, C.**, "Plasma Actuation for the Control of a Supersonic Projectile," *Journal of Spacecraft and Rockets*, Vol.46 No.5, pp.989-998, 2009.

[16] **Gnemmi, P., Charon, Duperoux, J-P, and George, A.**, "Feasibility Study for Steering a Supersonic Projectile by a Plasma Actuator," *AIAA Journal*, Vol.46, No.6, pp.1308-1317, 2008.

[17] **Corke, T. C., Tillotson, D., Patel, M.P.**, "Radius Flow Vectoring for Projectile Drag and Steering Control Using Plassma Actuators," *AIAA 2008-3769*, Jun, 2008.

[18] **Ericsson, L.E., Reding,L.P.**, "Asymmetric Flow Separation and Vortex Shedding," Tactical Missile Aerodynamic : General Topics, *in Progress in Astronautics and Aeronautics*, Vol.141,pp.291-452,1991.

[19] **Pick,G.S.**, "Investigation of Side Forces on Ogive-Cylinder Bodies at High Angles of Attack in the M=0.5 to 1.1 Range," *AIAA 1971-570*, Jun, 1971.

[20] **Allen, H. J., Perkins, E. W.**, "Characteristic of Flow Over Inclined Bodies of Revolution," *NACA RM A50L07*, 1951.

[21] **Allen, H. J., Perkins, E. W.**, "A Study of Viscosity on Flow Over Slender Inclined Bodies of Revolution," *NACA TN1048*, 1953.

[22] **Rao,D.M.**, "Side Force Alleviation on Slender, Pointed Forebodies at High Angles of Attack," *Journal of Aircraft*, Vol.16,pp.763-768, 1979.

[23] **Degani, D., Schiff,L.B.**, "Numerical Simulation of the Effect of Spatial Disturbances on Vortex Asymmetry," *AIAA Journal*, Vol.29,No.3, PP.344-352,1991.

[24] **Degani, D.**, "Effect of Geometrical Disturbance on Vortex Asymmetry," *AIAA Journal*, Vol.29, No.4, PP.560-566, 1991.

[25] **Ng,T.T.**, "Effect of a Single Strake on the Forebody Vortex Asymmetry," *Journal of Aircraft*, Vol.27, No.9,pp.844-846,1990.

[26] **Stahl, W.**, "Suppression of Vortex Asymmetry behind Circular Cones," *AIAA Journal*, Vol.28, No.6, pp.1138-1140, 1990.

[27] **Ng, T.T., Malcom, G. N.**, "Aerodynamic Control Using Forebody Strakes," *AIAA 1991-0618*, Jan, 1991.

[28] **Modi, V.J., Cheng, C.W., Mark, A., Yokomizo, T.**, "Reduction of the Side Force on Pointed Forebodies Through Add-on Tip Devices," *AIAA Jouranl*, Vol.30, No.10, pp.2462-2468, 1992.

[29] **Chen, L., Ng, T. T., Smith, B.**, "Forebody Vortex Control Using Nose-Boom Starkes," *Journal of Aircraft*, Vol.32, No.4, pp.896-898, 1995.

[30] **Peake, D.J., Rainbird, W.J., Atraghji, E. G.**, "Three Dimensional Flow Separation on Aircraft and Missiles," *AIAA Journal*, Vol.10, No. 5, pp.567-580, 1972.

[31] **Massey, K.C, McMichael, J, Warnock, T, and Hay, F.**, "Mechanical Actuators for Guidance of a Supersonic Projectile," *Journal of Spacecraft and Rockets*, Vol.45, No.4 pp.802-812, 2008.

[32] **Silition, S. I., and Massey, K. C.**, "Investigate of Actuator Performance for Guiding Supersonic Projectiles," *Journal of Spacecraft and Rockets*, Vol.45, No.3, pp.504-510, 2008.

[33] **Apostolovski, G., and Andreopoulos, Y.**, "Microactuators for Projectile Flight Control Systems: a Feasibility Study," *Journal of Spacecraft and Rockets*, Vol.41, No.6, pp.1336-1346, 2004.

[34] **Liang, S-M, and Fu, J-K**, "Drag Reduction for Turbulent Flow over a Projectile: Part ii," *Journal of Spacecraft and Rockets*, Vol.31, No.1 pp.93-98, 1994.

[35] **Patel, M.P, DiCocco, J.M, Prince, T.S, and Ng,T.T.**, "Afterbody Flow Control for Low Alpha Missile Maneuvering," *AIAA 2003-3673*, Jun, 2003.

[36] **Patel, M.P, Carver, R, Lisy, F.J, Prince, T.S, and Ng,T.T.**, "Detection and Control of Flow Separation Using Pressure Sensors and Micro-Vortex Generators," *AIAA 2002-0268*, Jan, 2002.

[37] **Patel.M.P, Sowle,Z.H, Stucke, R, and Ng,T.T.**, "Aerodynamic Control of a Small Projectile," *AIAA 2006-667*, Jan, 2006.

[38] **Patel,M.P, Sowle, Z.H, and Ng.T.T.**, "Range and Endgame Performance Assessment of a Smart Projectile Using Hingeless Flight Control," *AIAA 2006-671*, Jan, 2006.

[39] **Simpson, R. L.**, "Aspects of turbulent boundary layer separation," *Progress in Aerospace Science*, Vol.32, pp. 457-521, 1996.

[40] **Sears, W.r.**, "The Boundary Layer of Yawed Cylinder," *Journal of The Aeronautical Sciences*, Vol.15, No.1, pp.49-52, 1948.

[41] **Tobak, M., Peake, D.J.**, "Topology of Two-Dimensional and Three-Dimensional Separated Flow," *AIAA 1979-1480*, 1979.

[42] **Maskell, E.C.**, "Flow Separation in Three-Dimensions," RAE Report Aero.2565, Royal Aircraft Establishment, Farnborough, Great Britain, Nov, 1955.

[43] **Lighthill, M.J.**, "Attachment and Separation in Three-Dimensional Flow," *in Laminar Boundary Layer*, ed.L. Rosenhead, Oxford University Press, 1963, pp.72-82.

[44] **Lighthill, M.J.**, "Introduction, Boundary-Layer Theory," *in Laminar Boundary Layer*, ed.L. Rosenhead, Oxford University Press, 1963, pp.46-109.

[45] **Zeiger, M.D., Telionis, D.P., Vlachos, P.P.**, "Unsteady Separation Flows over Three-Dimensional Slender Bodies," *Progress in Aerospace Sciences*, Vol.40, pp.291-320, 2004.

[46] **Joslin,R.D., Thomas,R.H., Choudhari,M.M.**, "Synergism of flow and noise control technologies," *Progress in Aerospace Science*, Vol.41, pp.363-417, 2005.

[47] **Keener E.R., and Chapman G.T.**, "similarity in vortex asymmetries over slender bodies and wings," *AIAA Journal*, Vol.15, pp.1370-1372, Sept.1977.

[48] **Hal, I.M., Rogers, E.W., Davies, B.M.**, "Experiments with Inclined Blunt-Nosed Bodies at M=2.45," *Aeronautical Research Council*, London, R&M 3128, Aug, 1957.

[49] **Ericsson, L. E.**, "Unsteady flow," *Tactical Missile Aerodynamics: General Topics, in Progress in Astronautics and Aeronautics*, Vol.141, pp.453-502, 1991.

[50] **Hemsch, M. J., Nielsen, J.N.**, "Tactical Missile Aerodynamic: General Topic," Vol.141 *Progress in Astronautics and Aeronautics*, AIAA, New York, 1992.

[51] **Hsia, H.T.-S.**, "Equivalence of Secondary Injection to A Blunt Body in Supersonic Flow," *AIAA Journal*, Vol.4, No.10, pp.1832-1834, 1966.

[52] **Spaid, F.W., Cassel,L.A.**, "Aerodynamic Interface Induced by Reaction Control," *AGARD*, ad-755-209, Dec,1973.

[53] **Ferri, A.**, "Experimental Results with Airfoils Tested in the High-Speed Tunnel at Guidonia," *NACA TM 946*, 1940(translation).

[54] **Settles, G.S, and Dolling D.S.**, "Swept Shock-wave/Boundary-layer Interactions," Tactical Missile Aerodynamics: General Topics,*in Progress in Astronautics and Aeronautics*, Vol.141, pp.507-509, 1991.

[55] **Knight, D., Yan, H., Panaras, G,A., and Zheltovodov, A.**, "Advances in CFD Prediction of Shock Wave Turbulent Boundary Layer Interactions," *Progress in Aerospace Sciences*, Vol.39, pp.121-184, 2003.

[56] **Fujii, K.**, "Progress and Future Prospects of CFD in Aerospace- Wind Tunnel and beyond," *Progress in Aerospace Science*, Vol.41, pp. 455-470, 2005.

[**57**] **Shang, J.S.**, "Three Decades of Accomplishments in Computational Fluid Dynamics," *Progress in Aerospace Science*, Vol.40, pp. 173-197, 2004.

[**58**] **Piomelli, U.**, "Large-eddy Simulation: Achievement and Challenges," *Progress in Aerospace Science*, Vol.35, pp. 335-362, 1999.

[**59**] **Rumsey, C.L., Swanson, R.C.**, "Modeling and Simulation," Fundamentals and Applications of Modern Flow Control, *in Progress in Astronautics and Aeronautics*, Vol.231, pp.177-229, 2005.

[**60**] **Corson, D., Jaiman, R., Shakib, F.**, "Industrial Application of RANS Modeling: Capabilities and Needs," *International Journal of Computational Fluid Dynamics*, Vol.23, No. 4, pp. 337-347, 2009.

[**61**] **Georgiadis, N., Rizzetta, D., Fureby, C.**, "Large-Eddy Simulation: Current Capabilities, Recommended Practices, and Future Research," *AIAA 2009-948*, Jan 2009.

[**62**] **Baker, T.J.**, "Mesh Generation: Art or Science," *Progress in Aerospace Science*, Vol.41, pp. 29-63, 2005.

[**63**] **Dvaid, W.R., MackMynowski, D.G.**, "Brief History of Flow Control," Fundamentals and Applications of Modern Flow Control,*in Progress in Astronautics and Aeronautics*, Vol.231, pp.1-20, 2005.

[**64**] **Gross, A, AND Fasel, H. F.**, "CFD for Investigating Active Flow Control (Invited)," *AIAA 2008-4310*, Jun 2008.

[**65**] **Cummings, R.M., Forsythe, J.R., Morton, S.A., Squires, K. D.**, "Computational Challenges in High Angles of Attack Flow Prediction," *Progress in Aerospace Science*, Vol.39, pp. 369-384, 2003.

[66] **umsey, C.L., Swanson, R.C.**, "Turbulence Modelling for Active Flow Control Applications," *International Journal of Computational Fluid Dynamics*, Vol.23, No. 4, pp. 317-326, 2009.

[67] **Battern, P., Goldberg, U., Peroomian, O., Chakravarthy, S.**, "Recommendations and Best Practice for The Current State of The Art in Turbulence Modelling," *International Journal of Computational Fluid Dynamics*, Vol.23, No. 4, pp. 363-374, 2009.

[68] **Spalart,R,P.**, "Strategies for Turbulence Modeling and Simulations," *International Journal of Heat and Fluid*, Vol.21, pp.252-263, 2000.

[69] **Weinacht,P, Sturek, W. B.**, "Computation of the Roll Characteristics of a Finned Projectile," *Journal of Spacecraft and Rockets*, Vol.33 No.6,pp.769-775 , 1996.

[70] **Doraiswamy, S, and Candler, G.V.**, "Detached Eddy Simulations and Reynolds-Averaged-Navier-Stokes," *Journal of Spacecraft and Rockets*, Vol.45 No.5, pp.935-945, 2008.

[71] **Weinacht, P.**, "Projectile Performance, Stability, and Free-Fright Motion Prediction Using Computational Fluid Dynamics," *Journal of Spacecraft and Rockets*, Vol.41 No.2, pp.257-263, 2004.

[72] **Oberkampf, W.L, and Trucano, T. G.**, "Verification and Validation in Computational Fluid Dynamics," *Progress in Aerospace Science*, Vol.38, pp.209-272, 2002.

[73] **Vadillo, J., Agarwal, R. K.**, "Numerical Study of Transonic Drag Reduction for Flow Past Airfoils Using Active Flow Control," *AIAA 2007-0712*, Jan,2007.

[74] **Rehnam, A., Kontis, K.**, "Synthetic Jet Control Effectiveness on Stationary and Ptiching Airfoils," *Journal of Aircraft*, Vol.43, No.6, pp1782-1798, 2006.

[**75**] **Menter, F.R.**, "Two-Equation Eddy-Viscosity Turbulence Models for Engineering Applications," *AIAA Journal*, Vol.32, No.8, pp.1598-1605, 1994.

[**76**] **Menter, F.R.**, "Ten Years of Industrial Experience with The SST Turbulence Model," *Turbulence, Heat and Mass Transfer 4*, ed: K.Hanjalic, Y.Nagano, M. Tummers, Begell House, Inc., pp.625-632, 2003.

[**77**] **Menter, F.R.**, "Zonal Two Equation K-omega Turbulence Models for Aerodynamic Flow," *AIAA Paper 1993-2906*, July 1993.

[**78**] **Cummings,R.M., Morton, S.A., McDaniel, D.V.**, "Experience in Accurately Predicting Time-Dependent Flows," *Progress in Aerospace Sciences*, Vol.44, pp.241-257, 2008.

[**79**] **Kim, S. W., Benson, T.J.**, "Comparison of the SMAC, PISO and Iterative Time-Advancing Schemes for Unsteady Flow," *Computers & Fluids*, Vol.21, No.3, pp. 435-454, 1992.

[**80**] **Strelets,M.**, "Detached Eddy Simulation of Massively Separated Flow," *AIAA 2001-0879*, Jan 2001.

[**81**] **Robinson, S.K.**, "Coherent Motions in the Turbulent Boundary Layer," *Annual Review of Fluid Mechanics*, Vol.23, pp.601-639, 1991.

[**82**] **Jiang, M., Machiraju, R., Thompson, D. S.**, "A Novel Approach to Vortex Core Region Detection," *In Joint Eurographics -IEEE TCVG Symposium on Visualization*, pp.217-225, May 2002.

[**83**] **Jiang, M., Machiraju, R., Thompson, D. S.**, "Detection and Visualization of Vortices," *Visualization Handbook*, pp. 295-309, C. Johnson and C. Hansen, eds, Academic Press, Jan 2005.

[**84**] **Levy, Y., Seginer, A., Degani, D.**, "Graphical Visualization of Vortical Flow by Means of Helicity," *AIAA Journal*, Vol.28, No.8, pp.1347-1352, 1990.

[**85**] **Degani, D., Levy, Y.**, "Asymmetric Turbulent Vortical Flows over Slender Bodies," *AIAA Journal*, Vol.30, No.9, pp.2267-2273, 1992.

[**86**] **Roth, M.**, "Automatic Extraction of Vortex Core Lines and Other Line-Type Features for Scientific Visualization," *PhD thesis*, Swiss Federal Institute of Technology Zurich, 2000.

[**87**] **Hunt J.C.R., Wray A.A., Moin, P.**, "Eddies, Stream, and Convergence Zones in Turbulent Flows," *Center for Turbulent Research Report CTR-S88*, pp. 193-208, 1988.

Appendix A

Q-criterion

Q-criterion is used to identify and visualize the vortex structure. This method, proposed by Hunt et al [87] in 1988, is a kind of Galilean-invariant definitions of a vortex using invariants of the velocity gradient tensor. Vortex core is identified as a connected region where $Q > 0$ and the pressure is lower than the ambient value. The eigenvalues, σ of ∇u satisfy the characteristic equation

$$\sigma^3 - P\sigma^2 + Q\sigma - R = 0 \tag{A.1}$$

Where P, Q and R are the three invariants, which are defined as

$$\begin{aligned} P &= tr(\nabla u) \\ Q &= \tfrac{1}{2}\left[(tr(\nabla u))^2 - tr((\nabla u)^2)\right] \\ R &= Det(\nabla u) \end{aligned} \tag{A.2}$$

The velocity gradient tensor ∇u can be separated into its symmetric and anti-symmetric parts.

$$\nabla u = S + \Omega = \frac{1}{2}(\nabla u + (\nabla u)^T) + \frac{1}{2}(\nabla u - (\nabla u)^T) \tag{A.3}$$

$$S_{ij} = \frac{1}{2}(\frac{\partial u_i}{\partial x_j} + \frac{\partial u_j}{\partial x_i}) \tag{A.4}$$

$$\Omega_{ij} = \frac{1}{2}(\frac{\partial u_i}{\partial x_j} - \frac{\partial u_j}{\partial x_i}) \tag{A.5}$$

Where S and Ω are called rate-of-strain tensor and rotation rate tensor respectively. For an incomporessible flow ($P = tr(\nabla u) = 0$), the second invariant,Q of ∇u is simplified to

$$Q = \frac{1}{2}(\|\Omega\|^2 - \|S\|^2) \tag{A.6}$$

$$\|\Omega\| = \left[tr(\Omega\Omega^T)\right]^{1/2} \tag{A.7}$$

$$\|Q\| = \left[tr(SS^T)\right]^{1/2} \tag{A.8}$$

Thus, Q represent the local balance between shear strain rate and vorticity magnitude.